Doctorate Dissertation

博士論文

# Study of the Time Differential Muon Spin Resonance Method for Muonium Hyperfine Splitting Measurement with a High-Rate Capable Detector

(ミューオニウム超微細構造測定のための耐高計数率検出器による
時間微分ミューオンスピン共鳴法の研究)

A Dissertation Submitted for Degree of Doctor of Philosophy
June 2018

平成 30 年 6 月博士（理学）申請

Department of Physics, Graduate School of Science,
The University of Tokyo

東京大学大学院理学系研究科物理学専攻

Shoichiro Nishimura

西村　昇一郎

# Study of the Time Differential Muon Spin Resonance Method for Muonium Hyperfine Splitting Measurement with a High-Rate Capable Detector

Shoichiro Nishimura

June 1, 2018

## Abstract

The muonium (Mu) ground state hyperfine structure (HFS) interval, $\nu_{\mathrm{Mu\ HFS}}$, in a zero magnetic field was measured at the Japan Proton Accelerator Research Complex (J-PARC), Materials and Life Science Experimental Facility (MLF), Muon Science Facility (MUSE), where a high intensity pulsed muon beam is provided. Mu HFS is strongly related to the muon anomalous magnetic moment $g-2$, which was reported of having a discrepancy of about $3\sigma$ between theoretical value and experimental value. To improve the precision of the $g-2$ measurement, it is important to measure Mu HFS precisely.

In the previous measurement at the Clinton P. Anderson Meson Physics Facility (LAMPF), it was reported that the time differential method can extract more information than the time integral method. However, it was rather limited due to low statistics. Therefore, we developed the time differential method by using high-intensity beam at J-PARC.

It is required for a decay positron detector to measure the time and the number of positrons correctly. Therefore, a silicon strip detector, which has a high rate capability and a good time resolution, was developed. By using this silicon strip detector, the time differential muon spin flip resonance method was developed.

For the development of the time differential method, a simulation study was performed. We reveal that the time differential method can determine the muonium HFS with only one frequency data, and by taking advantage of this property, it is possible to improve the statistical uncertainty 3.2 times compared to the conventional analysis method, which is also called the time integral method. The systematic uncertainty due to the microwave power drift is also improved with the time differential method.

The time differential method was applied to the experimental data taken in June 2017, and the obtained result was

$$\nu_{\mathrm{Mu\ HFS}} = 4\ 463\ 302.2\ (3.1)\ (0.2)\ \ \mathrm{kHz},$$

where the first error is the statistical uncertainty and the second one is systematic. The total uncertainty was 690 ppb. This value corresponds to an improvement by a factor of seven over the previous measurement at J-PARC, and is consistent with the previous best measurement at LAMPF. The precision in this experiment would be improved twice compared to the previous experiment at zero field if the measurement would run for the same period of time, and by using the time differential method. The measurement value of the Mu HFS frequency in a zero magnetic field at J-PARC MLF MUSE is expected to be more precise than that in a high magnetic field at LAMPF by the upgrade of experimental apparatuses in the future.

# Contents

# Chapter 1

# Introduction

Muonium (Mu) is the bound state of a positive muon and an electron, and one of hydrogen-like atoms. In the standard model (SM), a positive muon and an electron are point-like lepton particles so that the contribution of the strong interaction is relatively small and well understood.

The muon-to-electron mass ratio is extracted from the muonium hyperfine structure (HFS). The electron mass was determined quite precisely, so we can determine the muon mass precisely. In fact, the extraction from the muonium HFS is the most precise determination of the muon mass. The point is that the muon mass can not be predicted by the SM, but is an input parameter for the SM calculation of the Fermi coupling constant, the muon anomalous magnetic moment ($a_\mu = \frac{g_\mu - 2}{2}$), and so on. Actually, a more precise mass measurement can make theoretical prediction of the muonium HFS more accurate.

The precision measurement of $g-2$ is important because there is a discrepancy of 3.5 standard deviations between the SM prediction and the experimental value. This discrepancy suggests that there is a new physics beyond the SM, and a more precise measurement is desired. However, the experimental value of $g-2$ was extracted by using the muon-to-proton magnetic moment ratio obtained from the muonium HFS measurement, and it is necessary to measure the muonium HFS more precisely to improve the experimental value of $g-2$. Therefore, it is important to measure the muonium HFS precisely.

The idea to improve the precision of the muonium HFS is to use a new analysis method with high-intensity pulsed muon beam. In the previous experiments, the

muonium HFS was obtained by the time integrated signal data. The important point is that the time differential method can extract the information lost during the integration process from its signal shape, and both the statistical uncertainty and the systematic uncertainty can be improved.

This chapter describes the physics motivation of the muonium HFS measurement, the theoretical expression of the muonium HFS, and the introduction of the time differential method.

## 1.1 Hyperfine Structure of Hydrogen-like atom

Muonium is more suitable for the validation of the bound state quantum electrodynamics (QED) than other hydrogen-like atoms, such as hydrogen and positronium (Ps). For hydrogen, theoretical calculation is limited by the knowledge about the proton internal structure. Theoretical analysis for positronium is complicated and difficult due to annihilation and recoil effect. For muonium, which is free from these effects, it is possible to calculate more precisely than other hydrogen-like atoms. In addition, the experimental value can be as precise as the theoretical calculation. Therefore, the muonium HFS is one of the best probe to verify the bound state QED.

The latest measured value of hydrogen HFS is [1, 2, 3]

$$\Delta\nu_{\mathrm{H(exp)}} = 1\ 420.405\ 751\ 766\ 2(3)\ \mathrm{MHz} \tag{1.1}$$

and the theoretical value is [4]

$$\Delta\nu_{\mathrm{H(theory)}} = 1\ 420.405\ 11(79)(57)(140)\mathrm{MHz}, \tag{1.2}$$

where the first error comes from the finite size effect of the proton, the second error is the contribution of the proton polarizability, and the third error represents all remaining theoretical uncertainties. The comparison between the experimental value and the theoretical value is

$$\frac{\Delta\nu_{\mathrm{H(theory)}} - \Delta\nu_{\mathrm{H(exp)}}}{\Delta\nu_{\mathrm{H(exp)}}} = (-0.45 \pm 1.2)\ \mathrm{ppm}. \tag{1.3}$$

The combined value of the three most precise measurements of positronium HFS is [5, 6, 7]

$$\Delta\nu_{\mathrm{Ps(exp)}} = 203\,388.65(67)\ \mathrm{MHz}, \tag{1.4}$$

while the theoretical value is [8]

$$\Delta\nu_{\mathrm{Ps(theory)}} = 203\,391.69(41)\ \mathrm{MHz}, \tag{1.5}$$

where the uncertainty comes from unknown non-logarithmic higher-order terms and was estimated by using an analogous coefficient as in the case of the muonium HFS. The comparison between experimental and theoretical values is

$$\frac{\Delta\nu_{\mathrm{Ps(theory)}} - \Delta\nu_{\mathrm{Ps(exp)}}}{\Delta\nu_{\mathrm{Ps(exp)}}} = (1.5 \pm 0.4)\ \mathrm{ppm}. \tag{1.6}$$

There is a discrepancy of about three standard deviations between experiment and theory.

The muonium HFS was measured by two different methods. One is a measurement at a very-weak magnetic field, so called "zero" field, and the most precise measurement value is [9]

$$\Delta\nu_{\mathrm{Mu(ZF)}} = 4\,463.\,302\,2(14)\ \mathrm{MHz}. \tag{1.7}$$

The other one is a measurement at a high magnetic field, and the most recent measurement result is [10]

$$\Delta\nu_{\mathrm{Mu(HF)}} = 4\,463.\,302\,765(51)(17)\ \mathrm{MHz}, \tag{1.8}$$

in which the first error is the statistical uncertainty and the second one is systematic.

The current theoretical value is [11]

$$\Delta\nu_{\mathrm{Mu(theory)}} = 4\,463.302\,868(271)\ \mathrm{MHz}. \tag{1.9}$$

The comparisons between results of the zero field (ZF) measurement and the high field (HF) measurement at the Clinton P. Anderson Meson Physics Facility (LAMPF),

and the theoretical value are

$$\frac{\Delta\nu_{\mathrm{Mu(theory)}} - \Delta\nu_{\mathrm{Mu(ZF)}}}{\Delta\nu_{\mathrm{Mu(ZF)}}} = (150 \pm 320)\ \mathrm{ppb}, \tag{1.10}$$

and

$$\frac{\Delta\nu_{\mathrm{Mu(theory)}} - \Delta\nu_{\mathrm{Mu(HF)}}}{\Delta\nu_{\mathrm{Mu(HF)}}} = (23 \pm 61)\ \mathrm{ppb}, \tag{1.11}$$

respectively.

Table 1.1 summarizes the precision of the experiment, theory, and a comparison of hydrogen-like atom HFS. The muonium HFS provides the most precise comparison between experiment and theory. Thus, muonium HFS measurement is important to search for new physics beyond the SM.

Table 1.1: Summary table of precision of the hyperfine structure. Calculation of the comparison is mentioned above.

| Hydrogen-like atom | Experimental Precision | Theoretical Precision | Comparison |
|---|---|---|---|
| Hydrogen | 0.2 ppt | 1.2 ppm | $(-0.45 \pm 1.2)$ ppm |
| Positronium | 3.1 ppm | 1.1 ppm | $(0.15 \pm 0.32)$ ppm |
| Muonium (ZF) | 310 ppb | 61 ppb | $(150 \pm 320)$ ppb |
| Muonium (HF) | 12 ppb | 61 ppb | $(23 \pm 62)$ ppb |

## 1.2 Muon-Electron Mass Ratio and Muon-Proton Magnetic Moment Ratio

Hyperfine transition measurement can be used to extract fundamental constants: the muon-electron mass ratio, $m_\mu/m_e$, and muon-proton magnetic moment ratio, $\mu_\mu/\mu_p$.

### 1.2.1 Determination of the Magnetic Moment Ratio $\mu_\mu/\mu_p$

In a static magnetic field the Hamiltonian of muonium is described as

$$\mathcal{H} = h\Delta\nu \boldsymbol{I}\cdot\boldsymbol{J} + \mu_B^e g_J \boldsymbol{J}\cdot\boldsymbol{B} - \mu_B^\mu g'_\mu \boldsymbol{I}\cdot\boldsymbol{B}, \tag{1.12}$$

where $\boldsymbol{I}$ is the muon spin operator, $\boldsymbol{J}$ is the total angular momentum operator of the electron, $\boldsymbol{B}$ is the external static magnetic field, and $h$ is the Plank constant. $\mu_B^e = e\hbar/2m_e$ and $\mu_B^\mu = e\hbar/2m_\mu$ are the electron Bohr magneton and the muon Bohr magneton, respectively, where $m_e$ is the electron mass, $m_\mu$ is the muon mass, and $\hbar = h/2\pi$. $g'_\mu$ and $g_J$ are the g-factor ratios of muon and electron in muonium, respectively. They are different from the free value, $g_e$ and $g_\mu$, due to binding corrections in muonium, and are described as [12]

$$g'_\mu = g_\mu\left(1 - \frac{\alpha^2}{3}\left(1 - \frac{3}{2}\frac{m_e}{m_\mu}\right) - \left(\alpha^2\left(\frac{m_e}{m_\mu}\right)^2 - \frac{\alpha^3}{12\pi}\frac{m_e}{m_\mu} + \frac{97}{108}\alpha^4\right)\right), \tag{1.13}$$

$$g_J = g_e\left(1 - \frac{\alpha^2}{3}\left(1 - \frac{3}{2}\frac{m_e}{m_\mu}\right) + \frac{\alpha^3}{4\pi} - \left(\alpha^2\left(\frac{m_e}{m_\mu}\right)^2 + \frac{5\alpha^3}{12\pi}\frac{m_e}{m_\mu} + \alpha^4\left(\frac{1}{12} + \frac{0.289...}{\pi^2}\right)\right)\right), \tag{1.14}$$

in which $\alpha$ is the fine structure constant [11],

$$\alpha^{-1} = 137.035\ 999\ 135(31). \tag{1.15}$$

In a static magnetic field, the ground state splits into four substates as shown in Fig. 1.1. The substates are defined by the quantum numbers of the muon and electron spins, $\left(M_e,\ M_\mu\right)$. The transitions for $(1/2,\ 1/2) \leftrightarrow (1/2,\ -1/2)$, $\nu_{12}$, and $(-1/2,\ -1/2) \leftrightarrow (-1/2,\ 1/2)$, $\nu_{34}$, are observed by a microwave resonance technique. The transition frequencies are described by the Breit-Rabi formula [13]

$$\nu_{12} = -\frac{\mu_B^\mu g'_\mu B}{h} + \frac{\Delta\nu}{2}\left((1+x) - \sqrt{1+x^2}\right), \tag{1.16}$$

$$\nu_{34} = \frac{\mu_B^\mu g'_\mu B}{h} + \frac{\Delta\nu}{2}\left((1-x) + \sqrt{1+x^2}\right), \tag{1.17}$$

where

$$x = \left(g_J\mu_B^e - g'_\mu\mu_B^\mu\right)\frac{B}{h\Delta\nu}, \tag{1.18}$$

and $B$ is the intensity of the external static magnetic field. The Larmor relation, $2\mu_p B = h\nu_p$, and nuclear magnetic resonance (NMR) are used to determine $B$ in

terms of the precession frequency of the free proton, $\nu_p$, and the proton magnetic moment, $\mu_p$. The muonium HFS is obtained from the summation of the transition frequencies,

$$\nu_{12} + \nu_{34} = \Delta\nu. \tag{1.19}$$

The muon-to-proton magnetic moment ratio can be extracted from the difference between the transition frequencies,

$$\delta \equiv \nu_{34} - \nu_{12} = \frac{\mu_B^\mu g'_\mu \nu_p}{\mu_p} + \Delta\nu\left(\sqrt{1+x^2} - x\right). \tag{1.20}$$

By using the notation

$$r'_e = \frac{g_J \mu_B^e}{\mu_p}, \tag{1.21}$$

$$r'_\mu = \frac{g'_\mu \mu_B^\mu}{\mu_p}, \tag{1.22}$$

$x$ is rewritten as

$$x = \left(r'_e + r'_\mu\right)\frac{\nu_p}{2\Delta\nu}. \tag{1.23}$$

From Eqs. 1.20, 1.21, 1.22, and 1.23, $r'_\mu$ is described as

$$r'_\mu = \frac{1}{2}\frac{-(\Delta\nu)^2 + \nu_p r'_e \delta + \delta^2}{\nu_p\left(\nu_p r'_e + \delta\right)}. \tag{1.24}$$

The muon-to-proton magnetic moment ratio is expressed as

$$\begin{aligned}\frac{\mu_\mu}{\mu_p} &= \frac{r'_\mu}{2}\frac{g_\mu}{g'_\mu} \\ &= \frac{1}{4}\frac{-(\Delta\nu)^2 + \nu_p r'_e \delta + \delta^2}{\nu_p\left(\nu_p r'_e + \delta\right)}\left(1 - \frac{\alpha^2}{3}\left(1 - \frac{3}{2}\frac{m_e}{m_\mu}\right) - \left(\alpha^2\left(\frac{m_e}{m_\mu}\right)^2 - \frac{\alpha^3}{12\pi}\frac{m_e}{m_\mu} + \frac{97}{108}\alpha^4\right)\right)^{-1},\end{aligned} \tag{1.25}$$

in which 1.13 is used.

Therefore, we extract the hyperfine structure interval of the ground state $\Delta\nu$

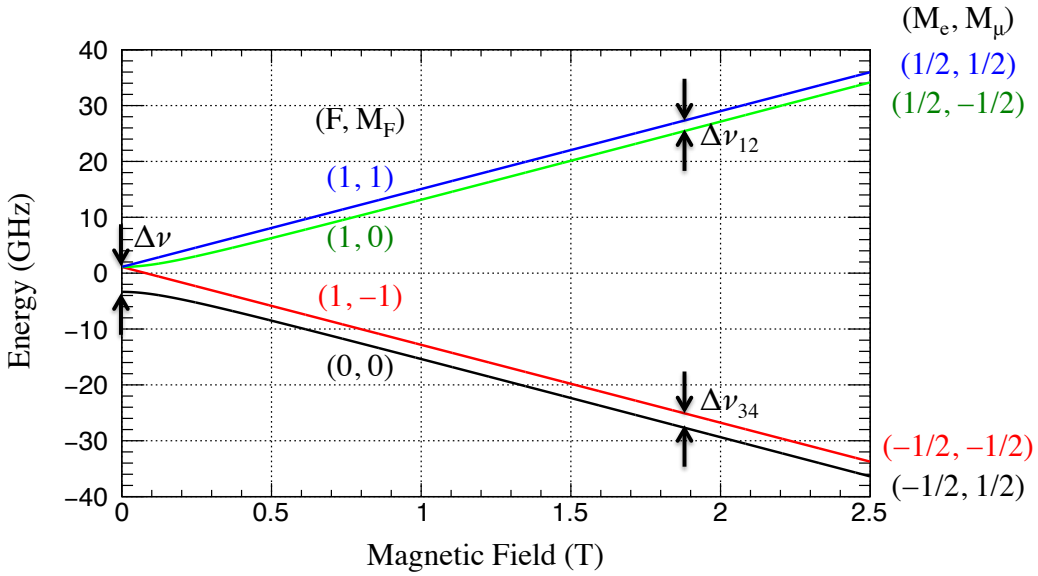


Figure 1.1: Energy levels diagram for muonium in the ground state as a function of the intensity of the static magnetic field. $M_\mu$ and $M_e$ are the quantum number of the muon and electron spins, respectively. $F$ is the quantum number of the total angular momentum and $M_F$ is the quantum number of the $z$ component of the total angular momentum.

and the muon-to-proton magnetic moment ratio $\mu_\mu/\mu_p$ by the measurements of the transition frequencies $\nu_{12}$ and $\nu_{34}$. The most precise experimented values are [10]

$$\nu_{12}(\text{exp}) = 1\,897\,539.800(35)\ \text{kHz} \quad (18\ \text{ppb}) \tag{1.26}$$

$$\nu_{34}(\text{exp}) = 2\,565\,762.965(43)\ \text{kHz} \quad (17\ \text{ppb}) \tag{1.27}$$

$$\Delta\nu(\text{exp}) = 4\,463\,302.765(53)\ \text{kHz} \quad (12\ \text{ppb}) \tag{1.28}$$

$$\frac{\mu_\mu}{\mu_p} = 3.183\,345\,13(39) \quad (120\ \text{ppb}) \tag{1.29}$$

### 1.2.2 Determination of the Mass Ratio $m_\mu/m_e$ from the Magnetic Moment Ratio

The muon-to-electron mass ratio $m_\mu/m_e$ is described as

$$\frac{m_\mu}{m_e} = \left(\frac{g_\mu}{g_e}\right)\left(\frac{\mu_p}{\mu_\mu}\right)\left(\frac{\mu_e}{\mu_p}\right). \tag{1.30}$$

Because $g_\mu$, $g_e$ and $\mu_e/\mu_p$ are known more precisely than $\mu_p/\mu_\mu$, $m_\mu/m_e$ can be obtained as precisely as $\mu_p/\mu_\mu$ by using Eq. 1.30 with $\mu_p/\mu_\mu$ from Eq. 1.25. The current value is [11]

$$\frac{m_\mu}{m_e} = 206.768\,276\,(24)\,, \tag{1.31}$$

by using Eq. 1.29 and the following physical constants,

$$a_\mu = \frac{g_\mu - 2}{2} = 0.001\,165\,920\,89\,(63)\,, \tag{1.32}$$

$$\frac{\mu_e}{\mu_p} = -658.210\,686\,6\,(20)\,. \tag{1.33}$$

### 1.2.3 Theoretical Expression of $\Delta\nu$

The theoretical expression for the transition frequency of the hyperfine splitting is described as the following equation [14],

$$\Delta\nu_{\mathrm{Mu(theory)}} = \Delta\nu_{\mathrm{F}}\,(1 + \mathrm{corrections})\,, \tag{1.34}$$

$$\Delta\nu_{\mathrm{F}} = \frac{16}{3} Z^3 \alpha^2 R_\infty c \frac{m_e}{m_\mu} \left(\frac{m_\mu}{m_e + m_\mu}\right)^3, \tag{1.35}$$

where $R_\infty$ is Rydberg constant [11],

$$R_\infty c = 3.289\,841\,960\,355(19) \times 10^{15}\ \mathrm{Hz}, \tag{1.36}$$

and $\Delta\nu_{\mathrm{F}}$ is the Fermi formula. $Z$ is the atomic number with $Z = 1$ for muonium.

The general expression for the transition frequency of the hyperfine splitting is [11]

$$\Delta\nu_{\mathrm{Mu(theory)}} = \Delta\nu_{\mathrm{rad}} + \Delta\nu_{\mathrm{rec}} + \Delta\nu_{\mathrm{r-r}} + \Delta\nu_{\mathrm{weak}} + \Delta\nu_{\mathrm{had}}, \tag{1.37}$$

where the terms labeled rad, rec, r-r, weak, and had stand for the radiative, recoil, radiative-recoil, electroweak, and hadronic contributions to the hyperfine splitting, respectively. Representative Feynman diagrams for these correction are presented in Fig. 1.2.

The radiative corrections come from emissions and reabsorptions of virtual

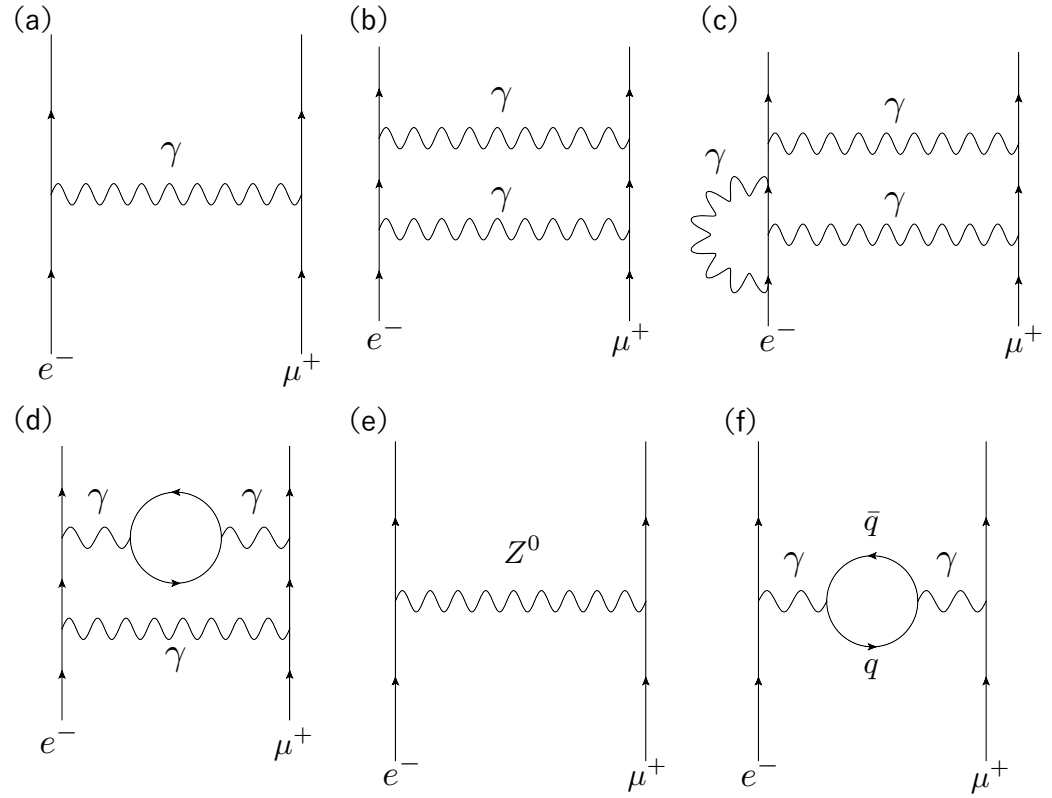


Figure 1.2: Representative Feynman diagrams for some contributions to the muonium hyperfine splitting. (a) is the leading radiative correction. (b) is the leading recoil correction. (c) and similar diagrams are the leading radiative-recoil correction from the electron line. (d) and similar diagrams are the leading radiative-recoil correction from vacuum polarization. (e) is the weak interaction contribution. (d) is the hadronic contribution.

photons by the muon and the electron. Purely radiative terms of orders $\alpha\,(Z\alpha)$ and $\alpha\,(Z\alpha)^2$ are known as [15]

$$\begin{aligned}\Delta\nu_{\rm rad} &= \Delta\nu_{\rm F}\left(1+a_\mu\right)\left(1+\frac{3}{2}\,(Z\alpha)^2+a_e+\alpha\,(Z\alpha)\left(\ln 2-\frac{5}{2}\right)\right.\\ &\left.-\frac{8}{3\pi}\alpha\,(Z\alpha)^2\ln\,(Z\alpha)\left[\ln\,(Z\alpha)-\ln 4+\frac{281}{480}\right]+\frac{14.88\pm 0.29}{\pi}\alpha\,(Z\alpha)^2\right),\end{aligned} \tag{1.38}$$

where $a_e$ and $a_\mu$ are the anomalous magnetic moments of the electron and muon, respectively. The different radiative contributions are summarized in Table 1.2.

Table 1.2: Contributions from the radiative corrections

| Term | Contribution (kHz) | Reference |
|---|---|---|
| $(Z\alpha)^2$ | 356.174 | [15] |
| $\alpha\,(Z\alpha)$ | −428.611(1) | [16] |
| $\alpha^2\,(Z\alpha)$ | 0.4256(2) | [15] |
| $\alpha\,(Z\alpha)^2$ | −32.115(3) | [17] |
| $\alpha\,(Z\alpha)^3$ | −0.542(8) | [18] |
| $\alpha^2\,(Z\alpha)^2$ | 0.193(24) | [19] |
| Total | −104.901(39) | |

The recoil contribution is given by

$$\Delta\nu_{\rm rec}=\Delta\nu_{\rm F}\left(-\frac{3Z\alpha}{\pi}\frac{m_\mu m_e}{m_\mu^2-m_e^2}\ln\frac{m_\mu}{m_e}+\frac{\gamma^2}{m_\mu m_e}\left[2\ln\frac{m_r}{2\gamma}-6\ln 2+\frac{65}{18}\right]\right), \tag{1.39}$$

where $\gamma\equiv Z\alpha m_r$ and $m_r=m_\mu m_e/\left(m_\mu+m_e\right)$.

The radiative-recoil contributions arising from both electron and muon lines and from vacuum polarizations are given by

$$\begin{aligned}\Delta\nu_{\rm r-r} &= \Delta\nu_{\rm F}\frac{\alpha\,(Z\alpha)}{\pi^2}\frac{m_e}{m_\mu}\left(-2\ln^2\frac{m_\mu}{m_e}+\frac{13}{12}\ln\frac{m_\mu}{m_e}+6\zeta\,(3)+\zeta\,(2)-\frac{71}{72}+3\pi^2\ln 2\right.\\ &\left.+Z^2\left[\frac{9}{2}\zeta\,(3)+\frac{39}{8}-3\pi^2\ln 2\right]+\frac{\alpha}{\pi}\left[-\frac{4}{3}\ln^3\frac{m_\mu}{m_e}+\frac{4}{3}\ln^2\frac{m_\mu}{m_e}+O\left(\ln\frac{m_\mu}{m_e}\right)\right]\right),\end{aligned} \tag{1.40}$$

where $\zeta$ is the Riemann zeta function.

The electroweak contribution due to the $Z^0$ exchange is

$$\begin{aligned} \Delta\nu_{\rm weak} &= -\Delta\nu_{\rm F} G_{\rm F} \frac{3\sqrt{2} m_\mu m_e}{8\alpha\pi} \\ &\simeq -0.065 \text{ kHz}, \end{aligned} \tag{1.41}$$

where $G_F$ is the Fermi coupling constant. The contribution from higher order terms is negligibly small.

The correction of the hadronic vacuum polarization is [20, 21]

$$\begin{aligned} \Delta\nu_{\rm had,\ LO} &= \frac{\alpha\,(Z\alpha)}{\pi^2} \Delta\nu \frac{m_e m_\mu}{m_\pi^2}\,(3.75 \pm 0.24) + \cdots \\ &= 0.2327(14) \text{ kHz}, \end{aligned} \tag{1.42}$$

where $m_\pi$ is the charged pion mass. Other contributions are from hadronic higher-order corrections and the hadronic light-by-light correction [21, 22, 23, 24]

$$\Delta\nu_{\rm had,\ HO} = 0.005(2) \text{ kHz}, \tag{1.43}$$

and

$$\Delta\nu_{\rm had,\ LbL} = 0.000\,0065(10) \text{ kHz}, \tag{1.44}$$

respectively.

The above theory yields

$$\Delta\nu_{\rm Mu}\,(\text{theory}) = 4\,463\,302.868(271) \text{ kHz}, \tag{1.45}$$

using values of the physical constants in CODATA-2014. The numerical values of the terms given in Eqs. 1.38-1.45 are summarized in Table 1.3. The dominant uncertainty of the theoretical calculation is the muon-electron mass ratio $m_\mu/m_e$. Therefore, a more precise measurement of the muon-electron mass ratio as noted in the previous section would make the uncertainty of the theoretical value smaller.

Table 1.3: Theoretical prediction of muonium HFS.

| Term | Contribution (kHz) | Reference |
|---|---|---|
| Fermi energy and $a_\mu$ | 4 459 031.819(253) | [11, 15] |
| $a_e$ | 5 170.926 | [25] |
| Radiative correction of $\alpha^n$ $(Z\alpha^m)$ | −104.901(39) | [15, 25] |
| Recoil | −791.714(80) | [25] |
| Radiative-recoil | −3.427(70) | [25] |
| Electroweak | −0.065 | [26] |
| Hadronic vacuum polarization | 0.232 7(14) | [20, 21] |
| Hadronic higher order | 0.005(2) | [22, 23] |
| Hadronic light by light | −0.000 0065(10) | [24] |
| Total | 4 463 302.868(271) | [11] |

### 1.2.4 Alternative Determination of the Mass Ratio $m_\mu/m_e$ from the Mu HFS

The mass ratio $m_\mu/m_e$ is regarded as a parameter in $\Delta\nu$, which could also be determined by the experimental result $\Delta\nu(\mathrm{exp})$. By using Eq. 1.28 as the experimental value, we obtain CODATA recommended values,

$$\frac{m_\mu}{m_e} = 206.768\ 282\ 6(46) \qquad (22\ \mathrm{ppb}), \tag{1.46}$$

and

$$\frac{\mu_\mu}{\mu_p} = 3.183345142(71) \qquad (22\ \mathrm{ppb}), \tag{1.47}$$

where we have used $R_\infty$ and $\alpha$ as in Eq. 1.36 and Eq. 1.15, respectively. This method can determine the values of $m_\mu/m_e$ and $\mu_\mu/\mu_p$ more precisely than the determination of $\mu_\mu/\mu_p$ from the difference between transition frequencies as discussed in Section 1.2.

## 1.3 Implementation of the Muon $g-2$ Measurements

The muon anomalous magnetic moment ($a_\mu = \frac{g_\mu - 2}{2}$) was measured in the E821 experiment at the Brookhaven National Laboratory (BNL). The current experimental

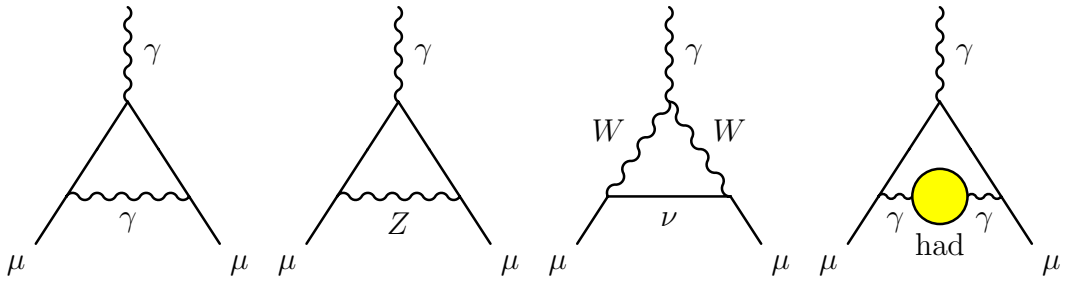


Figure 1.3: Feynman diagram for the muon $g-2$ corrections [29]. From left to right, the first order QED contribution (Schwinger term), the lowest-order weak contribution, and the lowest order hadronic contribution.

value is [27]

$$a_\mu\,(\mathrm{exp}) = 0.001\,165\,920\,91(54)(33) \qquad (0.54\ \mathrm{ppm})\,, \tag{1.48}$$

$$\tag{1.49}$$

where the first error is statistical and the second one is systematic.

Theoretical calculation also predicted the value of $g-2$ as precisely as the experimental value. The SM prediction value $a_\mu(\mathrm{SM})$ is [28]

$$\begin{aligned} a_\mu\,(\mathrm{SM}) &= a_\mu^{\mathrm{QED}} + a_\mu^{\mathrm{EW}} + a_\mu^{\mathrm{Had}} && (1.50)\\ &= 0.001\,165\,918\,23(1)(34)(26), && (1.51) \end{aligned}$$

where the errors are due to the electroweak, lowest-order hadronic, and higher-order hadronic corrections, respectively. Representative Feynman diagrams for these contributions are shown in Fig. 1.3.

The difference between the experimental value and the SM prediction is

$$\Delta a_\mu = a_\mu\,(\mathrm{exp}) - a_\mu\,(\mathrm{SM}) = 268(63)(43)\times 10^{-11}, \tag{1.52}$$

where the errors are from the experiment and SM prediction, respectively. Comparison of the measured value and the theoretical expectation is shown in Fig. 1.4. There is an interesting but not conclusive discrepancy of 3.5 standard deviations. This discrepancy may imply the existence of new physics beyond the SM. For example, supersymmetric (SUSY) models predict the following additional

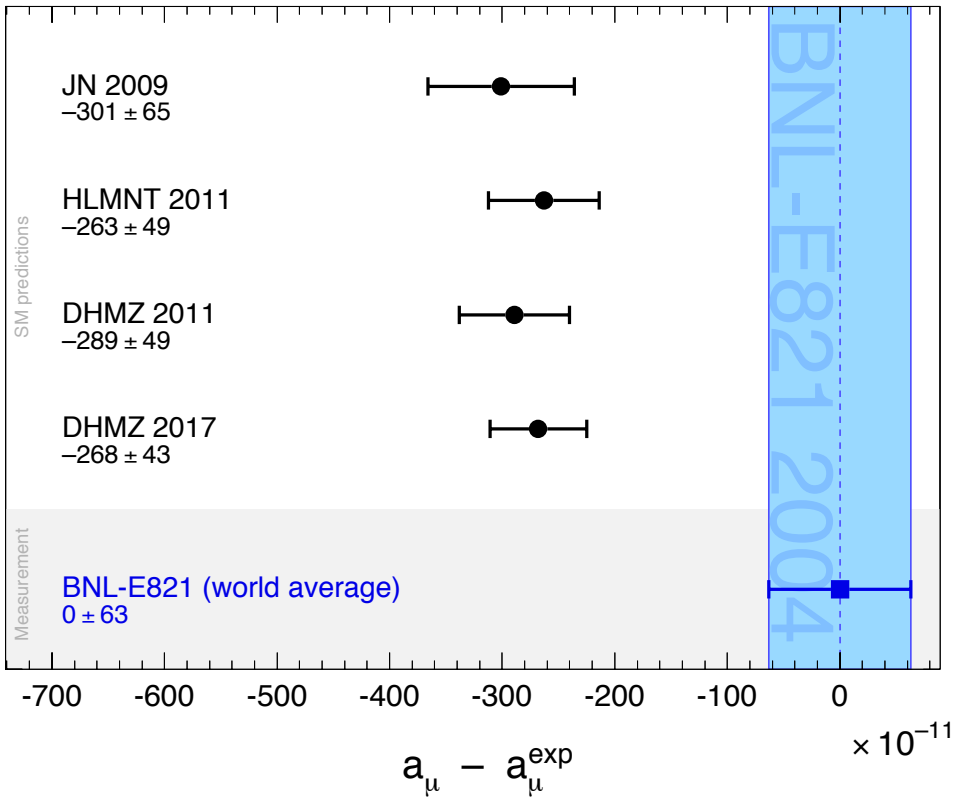


Figure 1.4: Comparison of experimental and theoretical values for $a_\mu$[29].

contribution [30],

$$a_\mu^{\mathrm{SUSY}} \simeq \pm 130 \times 10^{-11} \cdot \left(\frac{100\ \mathrm{GeV}}{m_{\mathrm{SUSY}}}\right) \tan\beta, \tag{1.53}$$

where $m_{\mathrm{SUSY}}$ is a representative supersymmetric mass scale, $\tan\beta \simeq$ 3-40 a potential enhancement factor, and $\pm 1$ corresponds to the sign of the $\mu$ term in the supersymmetric Lagrangian. Supersymmetric particles in the mass range 100-500 GeV could be the source of the deviation $\Delta a_\mu$.

Two experiments aim to improve the precision of the $g-2$ measurement value. One is the E989 experiment at the Fermi National Accelerator Laboratory (FNAL) [31]. The other is the E34 experiment at the Japan Proton Accelerator Research Complex (J-PARC) [32]. Table 1.4 compares the BNL experiment, its continuation at the Fermilab, and the J-PARC experiment.

In the $g-2$ experiments, the angular frequency of the spin precession of muon,

Table 1.4: Comparison of BNL-E821, FNAL-E989, and J-PARC-E34 [32].

| | BNL-E821 | FNAL-E989 | J-PARC-E34 |
|---|---|---|---|
| Muon momentum | 3.09 GeV/$c$ | | 0.3 GeV/$c$ |
| $\gamma$ | 29.3 | | 3.1 |
| Polarization | 100% | | 100% |
| Storage field | $B = 1.45$ T | | $B = 3.0$ T |
| Focusing field | Electric Quad. | | very-weak magnetic |
| Cyclotron period | 149 ns | | 7.4 ns |
| Spin precession period | 4.37 $\mu$s | | 2.11 $\mu$s |
| # of detected $e^+$ | $5.0\times10^9$ | $1.8\times10^{11}$ | $1.5\times10^{12}$ |
| # of detected $e^-$ | $3.6\times10^9$ | – | – |
| Statistical precision ($a_\mu$) | 0.46 ppm | 0.14 ppm | 0.14 ppm |

$\omega_a$, is measured in a ring. In a static magnetic field, $\omega_a$ is expressed as

$$\overrightarrow{\omega_a} = -\frac{e}{m_\mu}\left(a_\mu \overrightarrow{B} - \left(a_\mu - \frac{1}{\gamma^2-1}\right)\frac{\overrightarrow{\beta}\times\overrightarrow{E}}{c}\right), \tag{1.54}$$

where $B$ is the magnetic field intensity, while the term due to the muon electric dipole moment (EDM) is neglected because its contribution is very small. Eq. 1.54 can be simplify by using the magic momentum, $a_\mu - \frac{1}{\gamma^2-1} = 0$, or eliminating the electric field as

$$\overrightarrow{\omega_a} = -\frac{e}{m_\mu} a_\mu \overrightarrow{B}. \tag{1.55}$$

$B$ is determined by using the Larmor relation and nuclear magnetic resonance (NMR), which is the same method as in the muonium HFS measurement. $\omega_a$ is obtained by the oscillation of the time histogram of the decay positron as shown in Fig. 1.5.

## 1.4 Relations between $g-2$, Mu HFS, and $\mu_\mu/\mu_p$

The experimental value of $a_\mu$ is determined from the relation [27],

$$a_\mu = \frac{R}{\lambda - R},\ R = \frac{\omega_a}{\omega_p},\ \lambda = \frac{\mu_\mu}{\mu_p}, \tag{1.56}$$

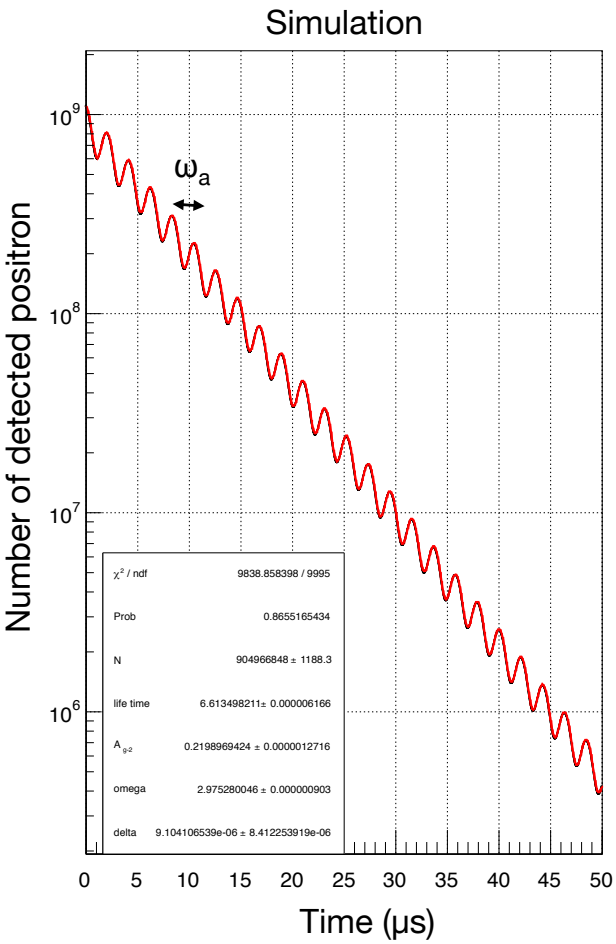


Figure 1.5: Distribution of decay positron counts versus time obtained by a simulation.

where $\omega_p = 2\pi\nu_p$. In the BNL experiment, they used the following numbers as inputs,

$$R(\mathrm{BNL}) = 0.003\,707\,206\,4(20), \qquad (540\ \mathrm{ppb}) \tag{1.57}$$

$$\lambda(\mathrm{LAMPF}) = 3.183\,345\,39(10). \qquad (31\ \mathrm{ppb}) \tag{1.58}$$

In Eq. 1.56, $a_\mu$ can be expanded in a series of $R/\lambda \simeq 10^{-3}$ terms,

$$a_\mu = \frac{R/\lambda}{1 - R/\lambda} = \frac{R}{\lambda}\left(1 + \frac{R}{\lambda} + \left(\frac{R}{\lambda}\right)^2 + \cdots\right), \tag{1.59}$$

and the uncertainty $\delta a_\mu$ is described as

$$\begin{aligned} \delta a_\mu &= \delta\left(\frac{R}{\lambda}\right)\left(1 + O\left(\frac{R}{\lambda}\right)\right) \\ &= \delta\left(\frac{R}{\lambda}\right). \end{aligned} \tag{1.60}$$

It is straightforward to calculate the relative uncertainty $\delta a_\mu/a_\mu$ as

$$\begin{aligned} \frac{\delta a_\mu}{a_\mu} &= \frac{1}{a_\mu}\sqrt{\left(\delta R \frac{\partial}{\partial R}\frac{R}{\lambda}\right)^2 + \left(\delta\lambda\frac{\partial}{\partial\lambda}\frac{R}{\lambda}\right)^2} \\ &= \sqrt{\left(\frac{\delta R}{R}\right)^2 + \left(\frac{\delta\lambda}{\lambda}\right)^2} \end{aligned} \tag{1.61}$$

In the J-PARC/Fermilab $g-2$ experiments, we aim at $\delta R/R = 140$ ppb and then $\delta a_\mu/a_\mu = 140$ ppb. To achieve this, we need

$$\frac{\delta\lambda}{\lambda} \ll 140\ \mathrm{ppb}. \tag{1.62}$$

Indeed, if $\left(\frac{\delta R}{R}, \frac{\delta\lambda}{\lambda}\right) = (140\ \mathrm{ppb},\ 120\ \mathrm{ppb})$, then $\delta a_\mu/a_\mu = 184$ ppb, while if $\left(\frac{\delta R}{R}, \frac{\delta\lambda}{\lambda}\right) = (140\ \mathrm{ppb},\ 30\ \mathrm{ppb})$, then $\delta a_\mu/a_\mu = 143$ ppb. These numbers clearly indicate that it is necessary to improve the value of $\lambda$, which is determined from the difference between transition frequencies $\delta$ in Eq. 1.20. Furthermore, the experimental value of $\lambda$, which was obtained from the muonium HFS was determined only in a high-field experiment. For an independent verification, a precise muonium

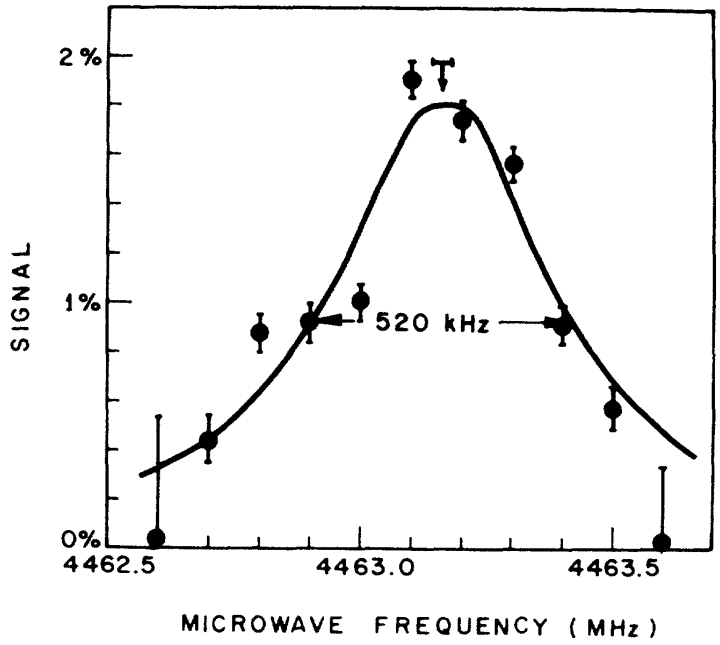


Figure 1.6: Time integral signal obtained by the previous zero-field experiment [33]. The error bars are due to statistical uncertainties. The solid line shows a least-squares fit by a Lorentzian with the center value at $4463.159 \pm 0.016$ MHz.

HFS measurement in a zero magnetic field is desired.

## 1.5 Mu HFS Measurement by the Time Integral Method

In the experiment, the muonium HFS was obtained from the relation between the microwave frequency and number of detected positrons. There are two kinds of analysis methods: the time integral method and the time differential method.

Figure 1.6 represents the time integral analysis obtained by the previous zero-field experiment. The signal of the time integral data is the integral of the number of detected positrons over the whole measurement time. The signal shape, plotted with the microwave frequency as the horizontal axis and the signal as the vertical axis, obeys a Lorentzian function, and the HFS frequency is obtained from the central value of the Lorentzian.

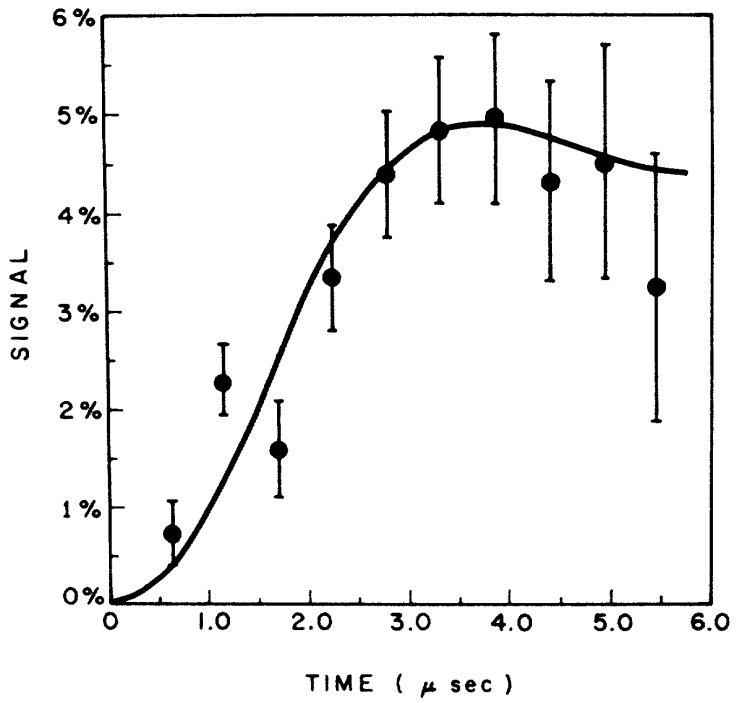


Figure 1.7: Time differential signal observed by the previous experiment [33]. The injected microwave frequency $\nu_0$ of this data is $\nu_0 = 4463.200$ MHz and the microwave power $P$ is 1.00 W. The solid curve is a fitting result to the time differential signal with a central frequency $\Delta\nu = 4463.161 \pm 0.011$ MHz.

## 1.6 Time Differential Method

Figure 1.7 shows the time differential data, which is equivalent to one of the data point of the time integral analysis in Fig. 1.6. In this analysis, the HFS frequency is derived from the time dependence of the signal. The time differential signal contains more information than the time integral signal and may eliminate the systematic uncertainty due to the power fluctuation with frequency. Therefore, it is expected that a detailed and precise measurement is possible by using the time differential method.

However, the previous time differential analysis was fairly limited because of low statistics. Also in the previous measurement, a DC muon beam was used. We can improve the statistical uncertainty by using the high-intensity pulsed muon beam at J-PARC. Thus, J-PARC high-intensity beam makes it possible to use the time differential method for the first time. On the other hand, the high-intensity beam

may distort the time differential signal due to pile-up. Therefore, it is necessary to develop a high-rate capable detector.

In general, a silicon strip detector is highly segmented and has a good time resolution, so it is well suited to the time differential analysis with a pulsed muon beam.

This paper presents the development of a silicon strip detector, the development of the time differential analysis and the experimental results obtained by the time differential analysis.

## 1.7 Organization of the Thesis

In the above, the physics motivation to measure muonium HFS and the advantage of the time differential method were discussed.

An important point to emphasize in this dissertation is the fact that the time differential method can improve statistical and systematic uncertainties compared to the time integral method, and it is actualized for the first time by using the high-intensity pulsed muon beam at J-PARC and a silicon strip detector with high-rate capability.

This dissertation describes the development of the silicon strip detector and the development of the time differential method. The second chapter presents the theoretical expression of the signal forms. It is important for the fitting to understand how the microwave power and its frequency affect the signal shapes.

The microwave system, the gas control system, and magnetic shields are important to reduce systematic uncertainty due to variation of the microwave power, gas density shift, and static magnetic field, respectively. The third chapter describes the experimental apparatus and also presents the development and construction of the silicon strip detector.

To substantiate the time differential method, a simulation study was developed. The advantage of the time differential method was also evaluated by the simulation. The detail of the simulation is described in the forth chapter.

The muonium HFS measurement at J-PARC was conducted in June 2017. The performance check of the silicon detector in the measurement and data analysis with

the time differential method are presented in the fifth chapter.

In the sixth chapter, we will discuss the experimental results and the estimation of the systematic uncertainty by a Monte-Carlo (MC) simulation at this time. Then, the perspectives of the muonium HFS measurement at J-PARC is described.

# Chapter 2

# Theoretical Discussion for the Muonium Hyperfine Structure Measurement

In the experiment, the muon spin flip induced by a microwave magnetic field is measured via the number of decay positrons. The theoretical expression of the signals is described in this chapter.

## 2.1 Muonium Decay

The dominant mode of the muonium decay is due to the decay of the free positive muon due to the weak interaction

$$\mu^+ \rightarrow e^+ + \nu_e + \bar{\nu}_\mu. \tag{2.1}$$

The measured mean lifetime $\tau_\mu$ or the muon decay rate $\gamma$ is [34]

$$\tau_\mu \equiv \frac{1}{\gamma} = 2.196\,981\,1(22)\ \mu\text{s}. \tag{2.2}$$

The momentum and angular spectrum of decay positrons from positive muons with degree of polarization $P$ is given by the following equation,

$$N\left(y,\ \theta\right) = \frac{\gamma}{2\pi} y^2 \left((3-2y) + (2y-1)\, P_z \cos\theta\right), \tag{2.3}$$

where $\theta$ is the angle between the muon spin direction and the positron momentum, and $y$ is the positron momentum $y = p/p_{\max}$, with $p_{\max}$ being the maximum momentum of the decay positron and given by

$$p_{\max} = \frac{m_\mu^2 - m_e^2}{2m_\mu} c \simeq 52.8\ \mathrm{MeV}/c. \tag{2.4}$$

## 2.2 Energy Levels of Muonium Ground State

Here the Hamiltonian of the muonium is introduced again.

$$\mathcal{H} = h\Delta\nu \boldsymbol{I}\cdot\boldsymbol{J} + \mu_B^e g_J \boldsymbol{J}\cdot\boldsymbol{B} - \mu_B^\mu g_\mu' \boldsymbol{I}\cdot\boldsymbol{B}. \tag{2.5}$$

The first term is the magnetic interaction between the electron and the muon. The second term and the third term are the energy of the electron and the muon in the static magnetic field, respectively.

The four eigenstates of the muonium are expressed as

$$\psi = \phi(r)\,\chi_{F,\,M_F}(\boldsymbol{B}), \tag{2.6}$$

where $\phi(r)$ is the spatial part of the wave function, $\chi_{F,\,M_F}(\boldsymbol{B})$ is the spin eigenfunction, $F$ is the quantum number of the total angular momentum, and $M_F$ is the associated magnetic quantum number. The spin eigenfuctions are

$$\begin{aligned}
\chi_{1,\,1}(\boldsymbol{B}) &= |1\rangle = \alpha_e\alpha_\mu, \\
\chi_{1,\,0}(\boldsymbol{B}) &= |2\rangle = c\alpha_e\beta_\mu + s\beta_e\alpha_\mu, \\
\chi_{1,\,-1}(\boldsymbol{B}) &= |3\rangle = \beta_e\beta_\mu, \\
\chi_{0,\,0}(\boldsymbol{B}) &= |4\rangle = c\beta_e\alpha_\mu - s\alpha_e\beta_\mu,
\end{aligned} \tag{2.7}$$

in which $\alpha_\mu$ and $\beta_\mu$ are the normalized spin eigenfunctions of the muon corresponding to the spin orientation in the positive $z$ direction and the negative $z$ direction,

respectively. $\alpha_e$ and $\beta_e$ are that of the electron. The quantities $s$ and $c$ are

$$c = \frac{1}{\sqrt{2}}\sqrt{1+\frac{x}{\sqrt{1+x^2}}}, \tag{2.8}$$

$$s = \frac{1}{\sqrt{2}}\sqrt{1-\frac{x}{\sqrt{1+x^2}}}, \tag{2.9}$$

where $x$ is defined in Eq. 1.18. $s$ and $c$ satisfy the following equation,

$$s^2 + c^2 = 1. \tag{2.10}$$

The energy eigenvalues of the Hamiltonian for the ground state are expressed in the Breit-Rabi equation

$$W_{F=\frac{1}{2}\pm\frac{1}{2},\ M_F} = -\frac{1}{4}h\Delta\nu - g'_\mu\mu_B^\mu M_F B \pm \frac{1}{2}h\Delta\nu\sqrt{1+2M_F x+x^2}. \tag{2.11}$$

The energy levels of the muonium ground state are represented in Fig. 1.1. At a very weak field, the energy levels of the state $|i\rangle$, $W_i$, are described as

$$\begin{aligned} W_1 &= \frac{1}{4}h\Delta\nu + \frac{\left(g_J\mu_B^e + g'_\mu\mu_B^\mu\right)}{2}B, \\ W_2 &= \frac{1}{4}h\Delta\nu, \\ W_3 &= \frac{1}{4}h\Delta\nu - \frac{\left(g_J\mu_B^e + g'_\mu\mu_B^\mu\right)}{2}B, \\ W_4 &= -\frac{3}{4}h\Delta\nu. \end{aligned} \tag{2.12}$$

## 2.3 State Populations of Muonium

The time-dependent populations of the four states are expressed by the density operator

$$\rho(t) = |\phi(t)\rangle\langle\phi(t)|, \tag{2.13}$$

where $|\phi(t)\rangle$ is the wave function for the system at time $t$. The density operator can be described as a density matrix using the eigenfunctions of the system as bases. The

elements of the density matrix are

$$\rho_{mn}(t)\langle m|(t)|n\rangle = \langle m|\phi(t)\rangle\langle\phi(t)|n\rangle. \tag{2.14}$$

An arbitrary muonium wave function is described as

$$|\psi\rangle = \sum_{i=1}^{4} a_i(0)|i\rangle \mathrm{e}^{-iW_i t/\hbar}, \tag{2.15}$$

where the coefficient $a_i(0)$ are normalized as

$$\sum_{i=1}^{4} a_i(0)a_i^*(0) = 1. \tag{2.16}$$

The diagonal matrix elements $\rho_{mn}(0) = |a_m(0)|^2$ give the probabilities of formation of the states $|m\rangle$ at time $t = 0$.

The density matrix for the muon with a polarization $P$ is

$$\rho_\mu(0) = \frac{1}{2}\begin{pmatrix} 1+P & 0 \\ 0 & 1-P \end{pmatrix}. \tag{2.17}$$

The density matrix for the electron is

$$\rho_e(0) = \frac{1}{2}\begin{pmatrix} 1 & 0 \\ 0 & 1 \end{pmatrix}. \tag{2.18}$$

The elements of the density matrix for muonium at $t = 0$ are

$$\rho_{ik}(0) = \langle i|\rho_e(0)\rho_\mu(0)|k\rangle. \tag{2.19}$$

Therefore, the density matrix is

$$\rho(0) = \frac{1}{4}\begin{pmatrix} 1+P & 0 & 0 & 0 \\ 0 & 1+P\left(s^2-c^2\right) & 0 & 2csP \\ 0 & 0 & 1-P & 0 \\ 0 & 2csP & 0 & 1+P\left(c^2-s^2\right) \end{pmatrix}, \tag{2.20}$$

where the spin eigenfunctions of Eq. 2.7 are used as bases. The probabilities of formation of the states are

$$\begin{aligned} P_1 &= \frac{1}{4}(1+P), \\ P_2 &= \frac{1}{4}\left(1+P\left(s^2-c^2\right)\right), \\ P_3 &= \frac{1}{4}(1-P), \\ P_4 &= \frac{1}{4}\left(1-P\left(s^2-c^2\right)\right). \end{aligned} \tag{2.21}$$

For a highly polarized beam $P \approx -1$ and a zero field case, the relative populations of the states are

$$\begin{aligned} |a_1(0)|^2 &= 0, \\ |a_2(0)|^2 &= \frac{1}{4}, \\ |a_3(0)|^2 &= \frac{1}{2}, \\ |a_4(0)|^2 &= \frac{1}{4}. \end{aligned} \tag{2.22}$$

## 2.4 State Amplitudes of Muonium

Muonium formed in a gas target populates Zeeman states. Transitions between Zeeman states are induced by the external magnetic field of the microwave. The transition probability depends on the difference between the microwave frequency and the transition frequency. A time dependent term $H'$ is added to the Hamiltonian in Eq. 2.5 due to the applied magnetic field of the microwave and is described as

$$\begin{aligned} \mathcal{H}' &= \left(\mu_e g_J \boldsymbol{J} - \mu_\mu g_\mu \boldsymbol{I}\right) \cdot \boldsymbol{B}_1 \cos\omega_0 t \\ &\equiv \mathcal{H}'_0 \cos\omega_0 t \\ &= \frac{1}{2}\mathcal{H}'_0\left(\mathrm{e}^{-i\omega_0 t} + \mathrm{e}^{i\omega_0 t}\right), \end{aligned} \tag{2.23}$$

where $\boldsymbol{B}_1 = B_x\hat{x} + B_y\hat{y}$ is the vector amplitude of the microwave field and $\omega_0$ is the microwave angular frequency. In the experiment, the microwave magnetic field is perpendicular to the muon spin direction.

The muonium wave function $\psi\left(\boldsymbol{r},\ t\right)$ is describe as

$$\psi\left(\boldsymbol{r},\ t\right)=\phi\left(\boldsymbol{r}\right)\sum_{k=1}^{4}a_{k}\left(t\right)\left|k\right\rangle \mathrm{e}^{-iW_{k}t/\hbar}, \tag{2.24}$$

where $\phi\left(\boldsymbol{r}\right)$ is the spatial component of the wave function, $\left|k\right\rangle$ are spin wave functions defined in Eq. 2.7, and $W_k$ are energy eigenvalues.

Time dependent state amplitudes of muonium are decomposed into the muon decay component and the state transition component induced by the microwave field. The muon decay operator is treated phenomenologically by

$$\dot{a}_{k}\left(t\right)=-\frac{1}{2}\gamma a_{k}\left(t\right), \tag{2.25}$$

and the state transition is expressed as

$$i\hbar\frac{\partial\psi}{\partial t}=\left(\mathcal{H}+\mathcal{H}'\right)\psi\left(t\right). \tag{2.26}$$

By using Eqs 2.25 and 2.26, the time dependence of the state amplitude is given by

$$\dot{a}_{k}\left(t\right)=-\frac{1}{2}\gamma a_{k}\left(t\right)-i\sum_{i=1}^{4}a_{i}b_{ik}f_{ik}\left(t\right), \tag{2.27}$$

where

$$b_{ik} = \frac{1}{2\hbar}\left\langle i\right|\mathcal{H}_{0}'\left|k\right\rangle, \tag{2.28}$$

$$f_{ik}\left(t\right) = \mathrm{e}^{-i\left(\omega_{ik}-\omega_{0}\right)t}+\mathrm{e}^{-i\left(\omega_{ik}+\omega_{0}\right)t}, \tag{2.29}$$

$$\omega_{ik} = \frac{W_{i}-W_{k}}{\hbar}. \tag{2.30}$$

For a general microwave field $\boldsymbol{B}_1 = B_x\hat{x}+B_y\hat{y}+B_z\hat{z}$, the matrix elements $b_{ik}$ are shown in Table 2.1. In the table, the following definition is used,

$$B_{\pm} = B_{x}\pm iB_{y}. \tag{2.31}$$

The $z$ axis is chosen parallel to $\boldsymbol{B}$ and the microwave field $\boldsymbol{B}_1$ is assumed to be perpendicular to $\boldsymbol{B}$. All diagonal elements of $b$ as well as $b_{42}$ and $b_{24}$ are zero

because $B_z = 0$ in the experiment.

Table 2.1: Matrix elements $b_{ik}$.

| k\ i | 1 | 2 | 3 | 4 |
|---|---|---|---|---|
| 1 | $\frac{g_J\mu_B^e + g'_\mu\mu_B^\mu}{4\hbar}B_z$ | $\frac{sg_J\mu_B^e + cg'_\mu\mu_B^\mu}{4\hbar}B_-$ | $0$ | $\frac{cg_J\mu_B^e - sg'_\mu\mu_B^\mu}{4\hbar}B_-$ |
| 2 | $\frac{sg_J\mu_B^e + cg'_\mu\mu_B^\mu}{4\hbar}B_+$ | $\left(c^2 - s^2\right)\frac{g_J\mu_B^e - g'_\mu\mu_B^\mu}{4\hbar}B_z$ | $\frac{cg_J\mu_B^e + sg'_\mu\mu_B^\mu}{4\hbar}B_-$ | $-2sc\frac{g_J\mu_B^e - g'_\mu\mu_B^\mu}{4\hbar}B_z$ |
| 3 | $0$ | $\frac{cg_J\mu_B^e + sg'_\mu\mu_B^\mu}{4\hbar}B_+$ | $-\frac{g_J\mu_B^e + g'_\mu\mu_B^\mu}{4\hbar}B_z$ | $\frac{-sg_J\mu_B^e + cg'_\mu\mu_B^\mu}{4\hbar}B_+$ |
| 4 | $\frac{cg_J\mu_B^e - sg'_\mu\mu_B^\mu}{4\hbar}B_+$ | $-2sc\frac{g_J\mu_B^e - g'_\mu\mu_B^\mu}{4\hbar}B_z$ | $\frac{-sg_J\mu_B^e + cg'_\mu\mu_B^\mu}{4\hbar}B_-$ | $\left(s^2 - c^2\right)\frac{g_J\mu_B^e - g'_\mu\mu_B^\mu}{4\hbar}B_z$ |

The time dependent coupled equations for the state amplitudes is given by the matrix

$$\begin{pmatrix} \dot{a_1} \\ \dot{a_2} \\ \dot{a_3} \\ \dot{a_4} \end{pmatrix} = \begin{pmatrix} -\frac{\gamma}{2} & 0 & 0 & -ib_{14}e^{i(\omega_{14}-\omega_0)t} \\ 0 & -\frac{\gamma}{2} & 0 & 0 \\ 0 & 0 & -\frac{\gamma}{2} & -ib_{34}e^{i(\omega_{34}-\omega_0)t} \\ -ib_{14}^* e^{-i(\omega_{14}-\omega_0)t} & 0 & -ib_{34}^* e^{-i(\omega_{34}-\omega_0)t} & -\frac{\gamma}{2} \end{pmatrix} \begin{pmatrix} a_1 \\ a_2 \\ a_3 \\ a_4 \end{pmatrix}, \quad (2.32)$$

in which,

$$b_{14} = \frac{1}{4\hbar}\left(B_x - iB_y\right)\left(cg_J\mu_B^e - sg'_\mu\mu_B^\mu\right), \quad (2.33)$$

$$b_{34} = -\frac{1}{4\hbar}\left(B_x + iB_y\right)\left(cg_J\mu_B^e - sg'_\mu\mu_B^\mu\right). \quad (2.34)$$

$b_{14}^*$ and $b_{34}^*$ are the conjugates of $b_{14}$ and $b_{34}$, respectively. The microwave power is defined as

$$b_{14} = -b_{34}^* \equiv b. \quad (2.35)$$

Clearly the state $|2\rangle$ is decoupled from other states.

For the zero field case, $\boldsymbol{B} = 0$ and the following relations hold,

$$\omega_{14} = \omega_{34} = 2\pi\Delta\nu \equiv \omega. \quad (2.36)$$

The three coupled equations can be reduced to an equivalent two-level problem. The state amplitudes defined by the linear combinations

$$A_+ = \frac{1}{\sqrt{2}}\left(a_1 + a_3\right), \tag{2.37}$$

$$A_- = \frac{1}{\sqrt{2}}\left(a_1 - a_3\right), \tag{2.38}$$

satisfy the matrix equations

$$\begin{pmatrix} \dot{A}_+ \\ \dot{A}_- \\ \dot{a}_4 \end{pmatrix} = \begin{pmatrix} -\frac{\gamma}{2} & 0 & 0 \\ 0 & -\frac{\gamma}{2} & -i\sqrt{2}b\mathrm{e}^{i(\omega-\omega_0)t} \\ 0 & -i\sqrt{2}b\mathrm{e}^{-i(\omega-\omega_0)t} & -\frac{\gamma}{2} \end{pmatrix} \begin{pmatrix} A_+ \\ A_- \\ a_4 \end{pmatrix}. \tag{2.39}$$

Only the $A_-$ and $a_4$ are coupled. The solution for the state amplitudes is

$$A_+(t) = \left(\frac{a_1(0) + a_3(0)}{\sqrt{2}}\right)\mathrm{e}^{-\gamma t/2}, \tag{2.40}$$

$$A_-(t) = \left(\left(\frac{a_1(0) - a_3(0)}{\sqrt{2}}\right)\left(\cos\frac{\Gamma t}{2} - \frac{i\Delta\omega}{\Gamma}\sin\frac{\Gamma t}{2}\right) + a_4(0)\left(-\frac{i2\sqrt{2}b}{\Gamma}\sin\frac{\Gamma t}{2}\right)\right)\mathrm{e}^{-\gamma t/2 + i\Delta\omega t/2}, \tag{2.41}$$

$$a_4(t) = \left(\left(\frac{a_1(0) - a_3(0)}{\sqrt{2}}\right)\left(-\frac{i2\sqrt{2}b}{\Gamma}\sin\frac{\Gamma t}{2}\right) + a_4(0)\left(\cos\frac{\Gamma t}{2} + \frac{i\Delta\omega}{\Gamma}\sin\frac{\Gamma t}{2}\right)\right)\mathrm{e}^{-\gamma t/2 - i\Delta\omega t/2}, \tag{2.42}$$

where

$$\Delta\omega = \omega - \omega_0 \equiv 2\pi\Delta, \tag{2.43}$$

$$\Gamma = \sqrt{\Delta\omega^2 + 8\left|b\right|^2}. \tag{2.44}$$

The state amplitudes $a_1(t)$ and $a_3(t)$ are given by

$$a_1(t) = \frac{1}{\sqrt{2}}\left(A_+(t) + A_-(t)\right), \tag{2.45}$$

$$a_3(t) = \frac{1}{\sqrt{2}}\left(A_+(t) - A_-(t)\right). \tag{2.46}$$

## 2.5 Time Dependence of the Muon Polarization

The time dependence of the muonium state is described as

$$\phi(t) = a_1(t)\,|1\rangle\, e^{-iW_1 t/\hbar} + a_2(t)\,|2\rangle\, e^{-iW_2 t/\hbar}. \tag{2.47}$$

The number of muon polarized along the $z$ axis is

$$P_z(t) = |a_1|^2 - |a_3|^2 + a_2^* a_4 e^{i\omega_{24} t} + a_4^* a_2 e^{-i\omega_{24} t}. \tag{2.48}$$

The muon decay rate $\gamma$ is relatively small compared to the HFS frequency $\omega_{24}$. Therefore, the cross terms are negligible, and Eq. 2.48 becomes

$$\begin{aligned} P_z(t) &= |a_1|^2 - |a_3|^2 \\ &= 2\mathrm{Re}\left(a_+^*(t) a_-(t)\right) \\ &= \frac{1}{4}\left(\cos\frac{\Delta\omega t}{2}\cos\frac{\Gamma t}{2} + \frac{\Delta\omega}{\Gamma}\sin\frac{\Delta\omega t}{2}\sin\frac{\Gamma t}{2}\right) e^{-\gamma t}. \end{aligned} \tag{2.49}$$

Then, the ensemble average of the muon spin polarization is

$$\begin{aligned} \langle P_z(t)\rangle &= \frac{P}{2}\left(\frac{G_+}{\Gamma}\cos G_- t + \frac{G_-}{\Gamma}\cos G_+ t\right) e^{-\gamma t} \\ &= P_{z0}(t) e^{-\gamma t}, \end{aligned} \tag{2.50}$$

where $G_\pm = \dfrac{\Gamma \pm \Delta\omega}{2}$, respectively.

## 2.6 Muon Spin Relaxation

Muonium depolarizes due to collisions and chemical reactions. The gas impurity may increase the rate of the muon spin relaxation. One of the main source of high spin relaxation is the oxygen contamination in the gas target. Considering the spin relaxation rate $\lambda$, the time dependence of the muon spin polarization can be written

as

$$\begin{aligned} P'_{z0} &= P_{z0}\mathrm{e}^{-\lambda t} \\ &= \frac{P}{2}\left(\frac{G_+}{\Gamma}\cos G_- t + \frac{G_-}{\Gamma}\cos G_+ t\right)\mathrm{e}^{-\lambda t}. \end{aligned} \tag{2.51}$$

## 2.7 Resonance Signal

The counting rate of the number of detected positrons is described as,

$$\frac{dN\left(\nu,\ |b|,\ t\right)}{dt} = N_0\frac{\lambda}{2\pi}y^2\left(3-2y\right)\left(1+\frac{2y-1}{3-2y}P'_{z0}\left(t\right)\cos\theta\right)\mathrm{e}^{-\gamma t}dyd\Omega, \tag{2.52}$$

in which $d\Omega$ is the infinitesimal solid angle and $N_0$ is the number of muons stopped in the gas target. Integrating Eq. 2.52 over $y$ from the threshold energy $y_0$ to 1 gives the total number of detected positron as

$$N = \int\int N_0\frac{\lambda}{4\pi}A_0\left(1+aP'\left(t\right)\cos\theta\right)\mathrm{e}^{-\gamma t}dtd\Omega, \tag{2.53}$$

where

$$A_0 = 1-\left(2y_0^3-y_0^4\right), \tag{2.54}$$

$$a = \frac{1-\left(3y_0^4-2y_0^3\right)}{3A_0}. \tag{2.55}$$

The signal is expressed by the ratio of the number of detected positron with and without microwave. The time development of the signal is described by the microwave frequency $\nu$ and the intensity of the microwave magnetic field $|b|$ as

$$\begin{aligned} S_{\mathrm{diff}}\left(\nu,\ |b|,\ t\right) &= \frac{dN_{\mathrm{ON}}/dt - dN_{\mathrm{OFF}}/dt}{dN_{\mathrm{OFF}}/dt} \\ &= \frac{N_{0,\mathrm{ON}}\int\left(1+\frac{aP'}{2}C\left(\nu,\ |b|,\ t\right)\cos\theta\right)\mathrm{e}^{-\gamma t}d\Omega - N_{0,\mathrm{OFF}}\int\left(1+\frac{aP'}{2}\cos\theta\right)\mathrm{e}^{-\gamma t}d\Omega}{N_{0,\mathrm{OFF}}\int\left(1+\frac{aP'}{2}\cos\theta\right)\mathrm{e}^{-\gamma t}d\Omega} \\ &= \frac{C\left(\nu,\ |b|,\ t\right)-1}{\frac{2}{aP'}\frac{S_2}{S_1}+1}, \qquad (\text{if } N_{0,\mathrm{ON}} = N_{0,\mathrm{OFF}}), \end{aligned} \tag{2.56}$$

in which

$$C(\nu,\ |b|,\ t) = \frac{G_+}{\Gamma}\cos G_- t + \frac{G_-}{\Gamma}\cos G_+ t, \tag{2.57}$$

$$S_1 = \int \cos\theta d\Omega, \tag{2.58}$$

$$S_2 = \int d\Omega. \tag{2.59}$$

The shape of the time differential signal is described by the summation of cosine functions. Their frequency and height are related to the field intensity of the stored microwave and the difference between the microwave frequency and the muonium HFS frequency.

Calculation results of Eq. 2.56 for several microwave frequencies and microwave intensities are plotted in Fig. 2.1. This signal expression is called the time differential signal. This figure indicates the following fact. When the microwave frequency is detuned from the muonium HFS frequency, the frequency of the component $\frac{G_-}{\Gamma}\cos G_+ t$ becomes higher, and that of $\frac{G_+}{\Gamma}\cos G_- t$ becomes lower, while signal heights of both components become lower. On the other hand, when the microwave power is increased, both frequency components become higher frequency and their signal heights become higher. The response to the signal form is obviously different between the microwave frequency and the stored microwave power. Hence, the time differential signal can extract the muonium HFS and the stored microwave power from its shape at the same time.

The integral over time from $t = 0$ to $t = \infty$ is elementary. The integration result is

$$\begin{aligned} S_{\rm int} &= \frac{N_{\rm ON} - N_{\rm OFF}}{N_{\rm OFF}} \\ &= \frac{\frac{aP}{2}\cos\theta}{1 + \frac{\lambda}{\gamma} + \frac{aP}{2}\cos\theta} \frac{-2|b|^2\left(\gamma'^2 + 2|b|^2\right)}{\left(\gamma'^2 + 2|b|^2\right)^2 + \gamma'^2\Delta\omega^2} \\ &= \frac{\frac{aP}{2}\cos\theta}{1 + \frac{\lambda}{\gamma} + \frac{aP}{2}\cos\theta} L(\nu,\ |b|), \end{aligned} \tag{2.60}$$

where $\gamma' = \gamma + \lambda$. $L$ is the Lorentzian function. This expression is called the time

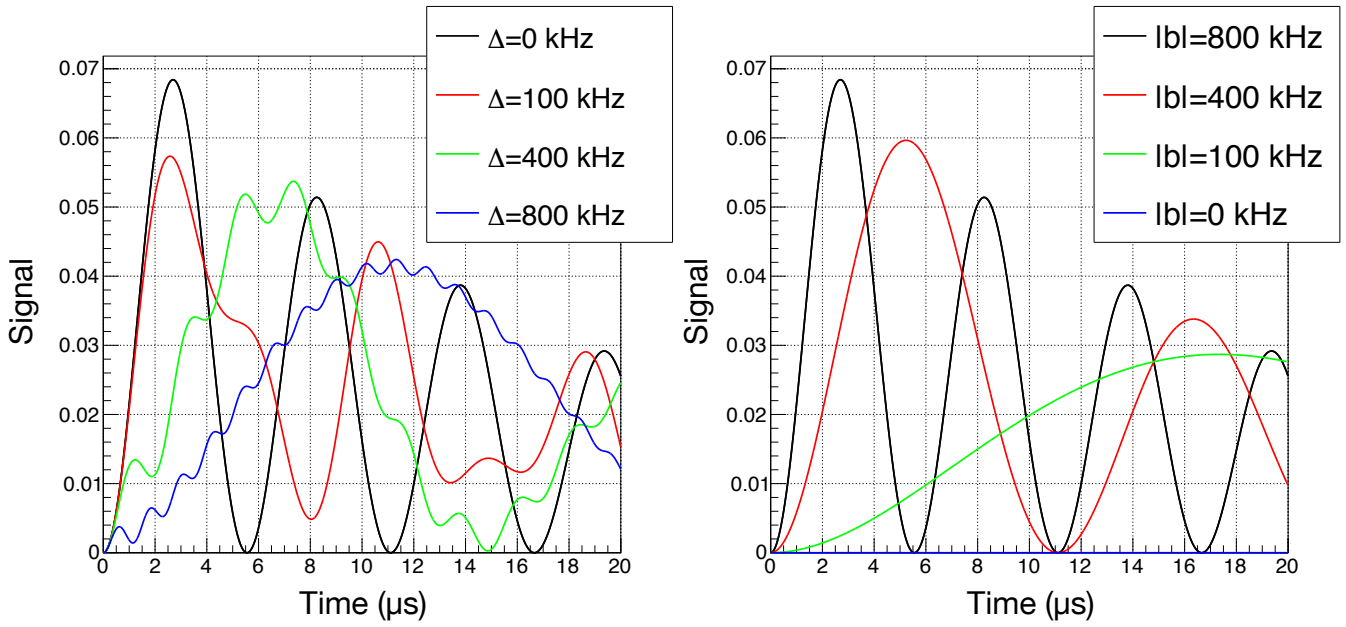


Figure 2.1: Time differential signals. The left side shows microwave frequency dependence of the time differential signal when the microwave power $|b|$ is 800 kHz. The detuning frequency from the muonium HFS is represented in respective colors. The right side represents microwave power dependence just on the resonance frequency. The stored microwave power is represented in respective colors.

integral signal. The signal shape described in Eq. 2.60 is plotted with the frequency difference between the microwave and the muonium HFS as the horizontal axis and the signal height as the vertical axis in Fig. 2.2. The time integral signal follows a Lorentzian function of which the center microwave frequency is equal to the muonium HFS frequency.

However the signals observed in the measurement are more complicated because the magnetic field intensity of the microwave varies with position. The integral of the time differential signal over the cavity is described as

$$\begin{aligned} S_{\mathrm{diff}}(\nu,\ t) &= \frac{\int\int \left(N_{0,\mathrm{ON}}(r,\theta,z)\left(1+\frac{aP'}{2}C(\nu,\ |b|,\ t)\cos\theta\right) - N_{0,\mathrm{OFF}}(r,\theta,z)\left(1+\frac{aP'}{2}\cos\theta\right)\right) d\Omega dV}{\int\int N_{0,\mathrm{OFF}}(r,\theta,z)\left(1+\frac{aP'}{2}\cos\theta\right) d\Omega dV} \\ &= \frac{\frac{aP'}{2}\int\int N_0(r,\theta,z)\left(C(\nu,\ |b|,\ t)-1\right)\cos\theta\ d\Omega dV}{\int\int N_0(r,\theta,z)\left(1+\frac{aP'}{2}\cos\theta\right) d\Omega dV}, \ (\text{if } N_{0,\mathrm{ON}} = N_{0,\mathrm{OFF}} = N_0), \end{aligned} \tag{2.61}$$

where $dV$ is the infinitesimal volume.

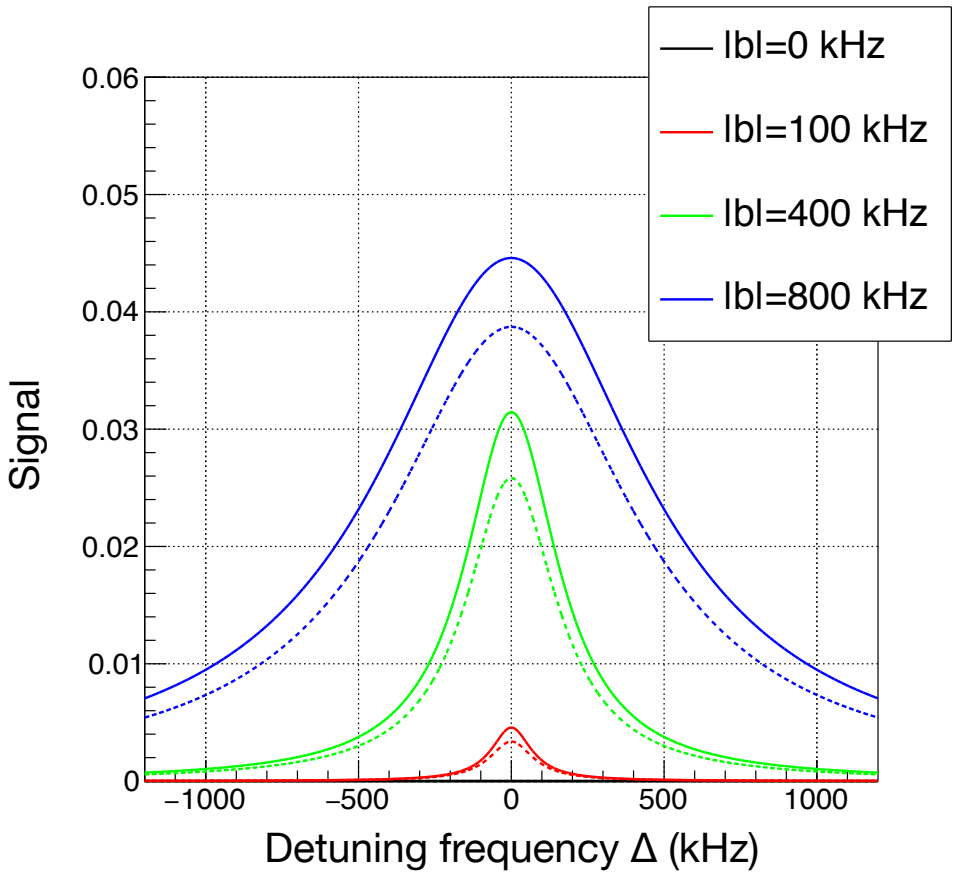


Figure 2.2: Time integral signals. Solid lines represent the Lorentzian signal without the spin relaxation. Broken lines show the signal considering a spin relaxation coefficient of 200 $\mu$s.

For the time integral method, the muonium HFS frequency is determined by a multitude of frequency data. Therefore, a microwave power variation with frequency due to the frequency characteristics of the microwave cavity may shift the center value of the Lorentzian function and results in one the source of systematic uncertainty.

On the contrary, the time differential method can determine the muonium HFS frequency from a single frequency data. In addition, the time differential signal can also extract the microwave power from the signal form at the same time. Thus, the time differential method can eliminate the systematic uncertainty due to fluctuation of the stored microwave power.

# Chapter 3

# Experimental Procedure and Apparatus

This chapter describes the experimental setup of the measurement of muonium HFS at J-PARC Materials and Life Science Experimental Facility (MLF) Muon Science Facility (MUSE). Figure 3.1 shows a schematic view of the zero field muonium HFS measurement. A polarized muon beam is injected in a Kr gas volume, and then muonium is formed in the cavity. The muon spin flip due to the microwave is measured by two types of detectors. Well suppressed very weak magnetic field was achieved by three layers of permalloy magnetic shield. A gas handling system controlled and monitored the Kr gas pressure.

## 3.1 Coordinate System

In the following discussion, the coordinate system is defined as shown in Fig. 3.1: the $z$-axis, the $y$-axis, and the $x$-axis are along the beam direction axis, the vertical axis, and the horizontal axis perpendicular to the $z$-axis and $y$-axis, respectively.

## 3.2 Muon Beam Line

Figure 3.2 shows the schematic view of the MLF muon beam line [35]. A proton beam injected into a graphite target produces surface muons with a momentum of typically 28.0 MeV/$c$, and then the D-Line transports the polarized surface muon beam to

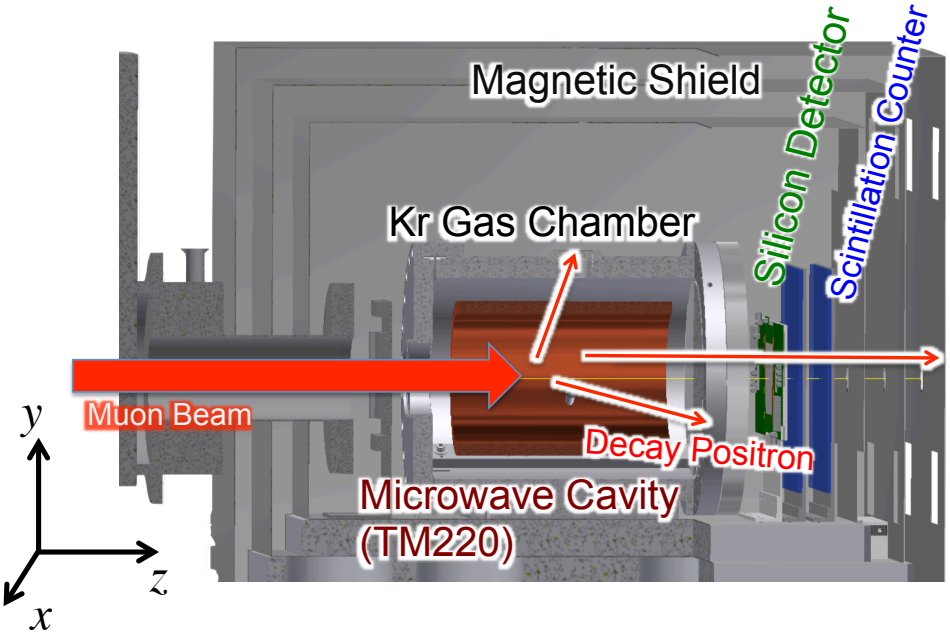


Figure 3.1: Schematic view of zero field experiment at J-PARC MLF MUSE. Muon beam is injected from the left side and stopped in Kr gas. The number of decay positron is counted by a silicon detector and two segmented scintillation counters.

the experimental area. The proton beam power was 150 kW in this experiment. The repetition rate of the beam was 25 Hz. The typical number of muons at the experimental area was $1.8 \times 10^5$ per pulse.

## 3.3 Magnetic Field Control System

For the zero field experiment, it is necessary to reduce the residual magnetic field in the cavity from the surroundings. The magnetic shields and a field measurement system are shown in Fig. 3.3. The magnetic shields consist of three layers of permalloy plates. The permeability of permalloy was estimated as 12000. A coaxial flux gate probe (MTI K. K. FM-3500) was used to measure the magnetic field. The resolution of the probe was about 0.5 nT. The result of the magnetic field measurement is shown in Fig. 3.4. A magnetic field of less than 350 nT was achieved, which is about 1000 times smaller than without the three layers of magnetic shield. The largest source of the magnetic field was from a thermocouple used to measure the temperature of the cavity. The time fluctuation of the magnetic field during muonium

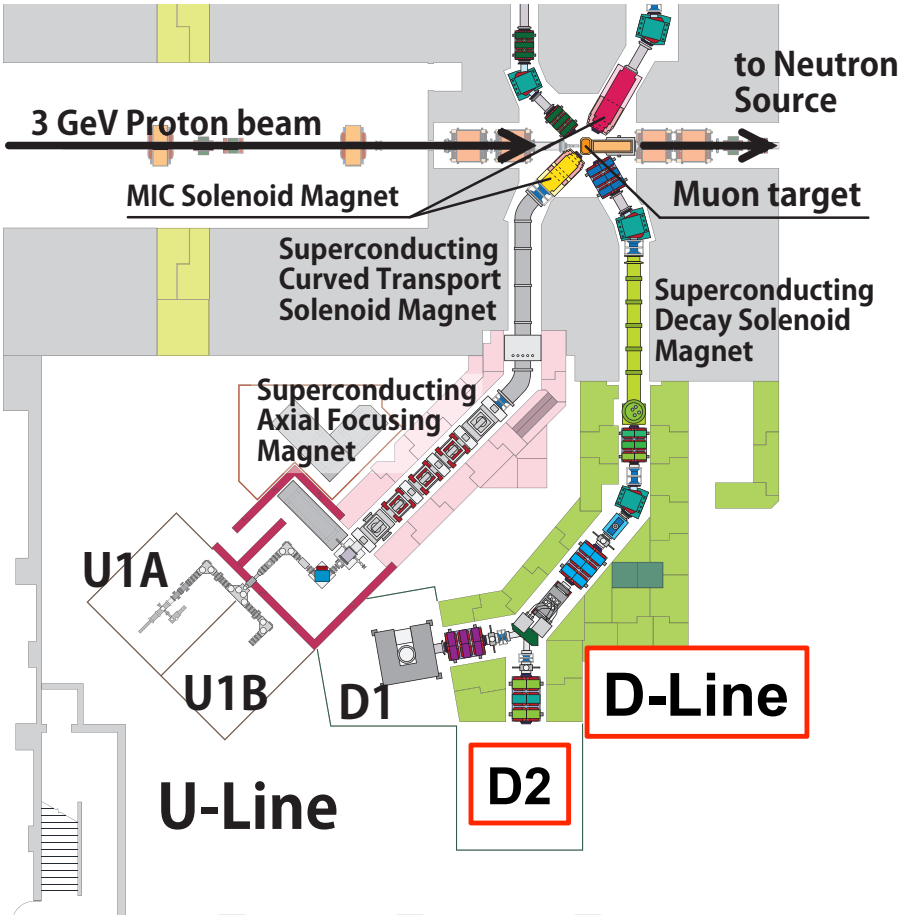


Figure 3.2: Schematic view of a part of the MLF experimental hall No.1 [35].

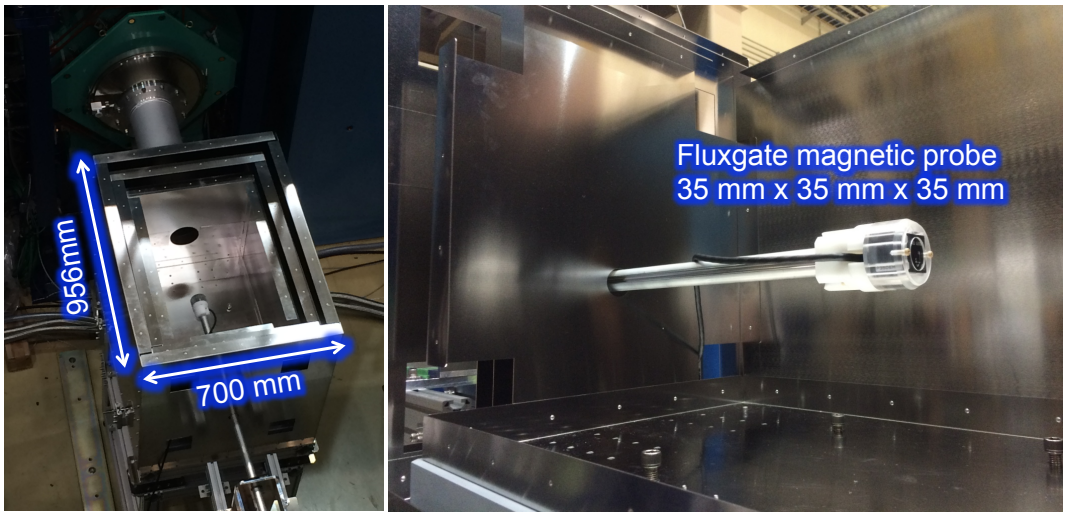


Figure 3.3: Three layers of magnetic shield and a field probe. The left picture shows a downward view of the magnetic shields, and the right the magnetic probe attached to the end of a moving pole.

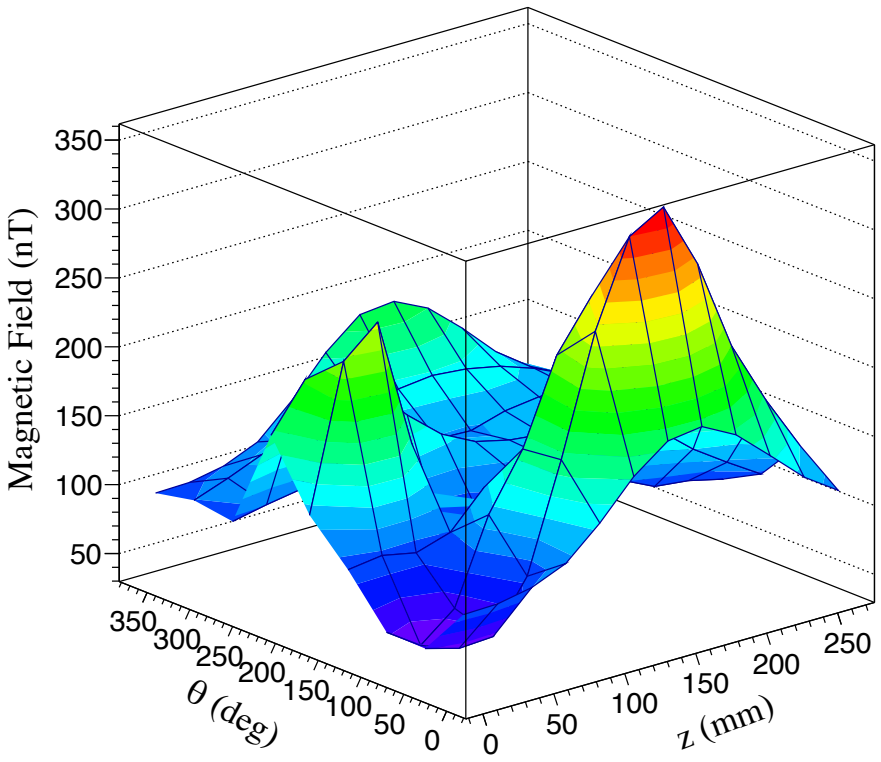


Figure 3.4: Result of the magnetic field measurement. The angle $\theta$ measures the rotation angle around the beam axis, and the probe was set at 41 mm from the center. The largest field source was from a thermocouple that was attached on the microwave cavity.

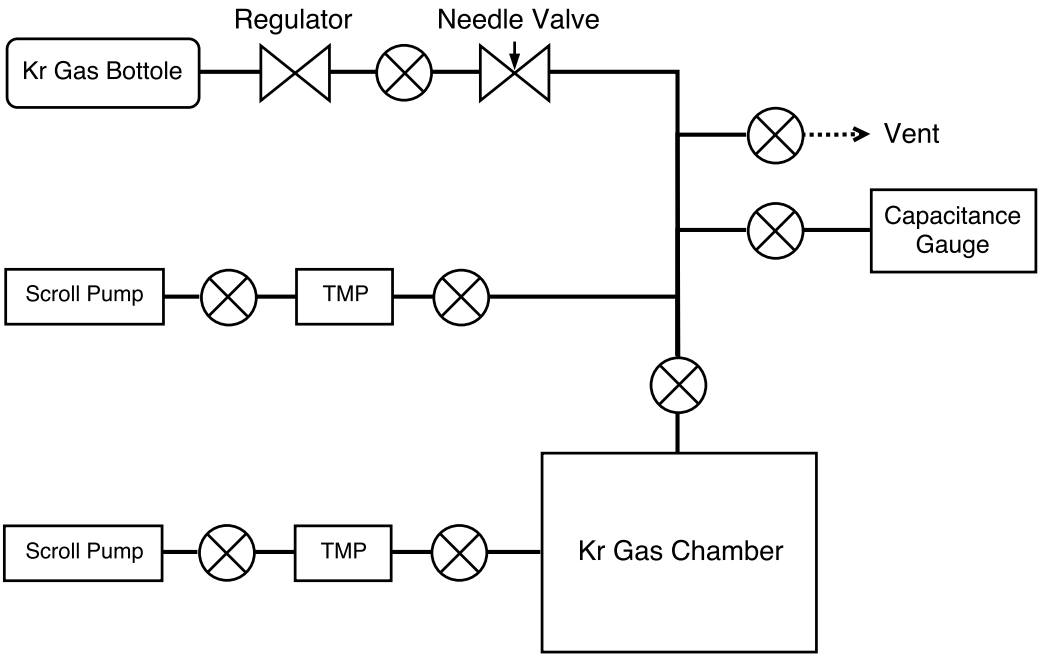


Figure 3.5: Block diagram of the gas control system. TMP stands for a turbo molecular pump. The gas pressure was monitored by a capacitance gauge.

HFS frequency measurements was monitored by the same probe. The measuring interval was 5 sec.

## 3.4 Gas Control System

The muonium HFS frequency is shifted in the Kr gas due to collisions. The collision rate depends on the Kr gas density, which can be calculated by knowing the gas pressure and temperature. Therefore, the muonium HFS frequency depends on the Kr gas pressure, and monitoring of the gas pressure is important to reduce systematic uncertainty due to gas density shift. Figure 3.5 shows the diagram of the gas control system. Scroll pumps and turbo molecular pumps were used to evacuate the gas chamber. The gas pressure was monitored by a capacitance gauge (ANELVA M-342DG) with a precision of 0.2% at 300 K. Figures 3.6 and 3.7 show pictures of the Kr gas chamber and the gas control panel. On the upstream side, a 100-$\mu$m thick aluminum foil separates the Kr gas volume from the outside. On the opposite side, there was a 55-mm thick flange, which also works as an absorber to

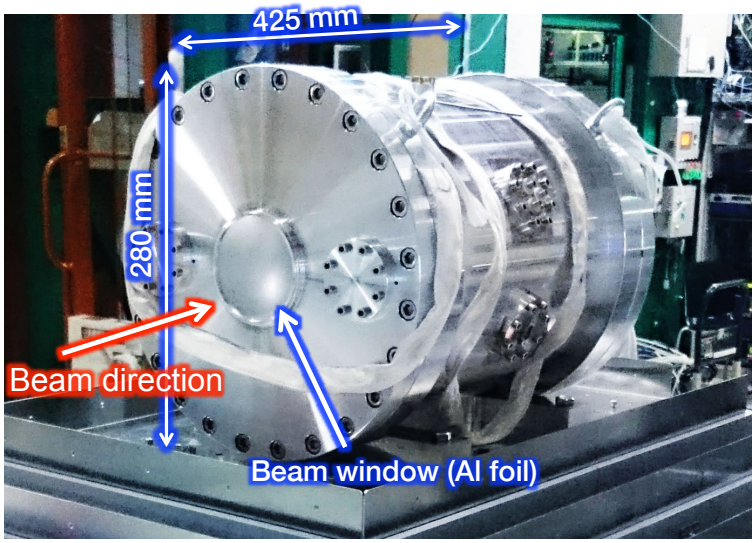


Figure 3.6: Kr gas chamber. There was a aluminum foil as a beam window at the front, and a chamber flange with a thickness of 55 mm as an absorber at the back.

cut off low energy positrons and duct streaming radiations.

### 3.4.1 Gas Selection

When positive muons stop in a gas target, muoniums are formed through the following electron capture reaction,

$$\mu^+ + \mathrm{Kr} \rightarrow \mathrm{Mu} + \mathrm{Kr}^+. \tag{3.1}$$

Muonium is formed in any one of the bound state. The ionization energy of muonium $E_I\,(\mathrm{Mu})$ is 13.54 eV and that of Krypton $E_I\,(\mathrm{Kr})$ is 14.000 eV [36]. In order for a muon to capture an electron from a Krypton atom to form muonium in the ground state, the kinetic energy of the muon-krypton system in the center of mass (CM) coordinate system must be greater than the threshold value

$$E_t\,(\mathrm{CM}) = E_I\,(\mathrm{Kr}) - E_I\,(\mathrm{Mu}) = 0.46\ \mathrm{eV}. \tag{3.2}$$

The ionization energies and the threshold energies for muonium formation for several atoms are listed in Table 3.1. $E_t$ is negative in the case of xenon, and muonium formation is always possible energetically. For the experiment, krypton gas is suitable

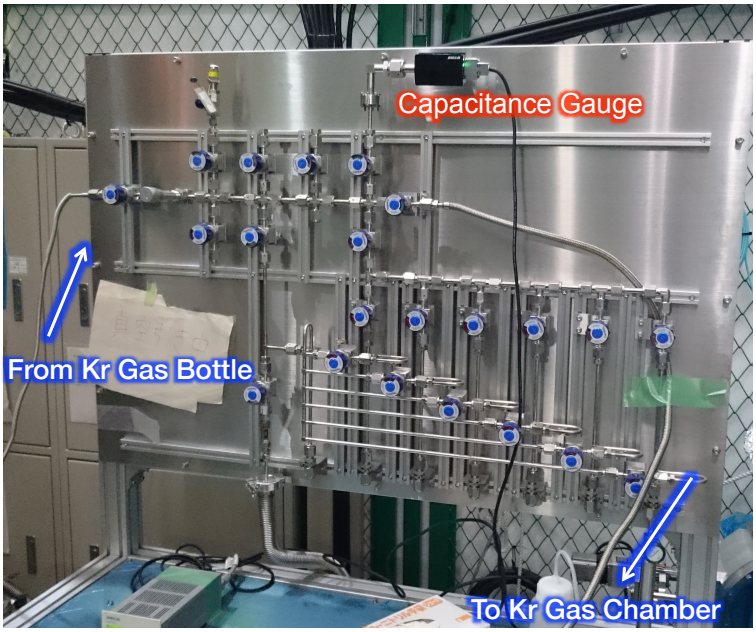


Figure 3.7: Kr gas control panel. A capacitance gauge was attached. The gas pressure was controlled and monitored by this panel.

because the muonium production is highly efficient due to the low energy threshold and the muonium momentum is low.

Table 3.1: Ionization energies, threshold energies, and fractions for muonium formation in rare gases [37, 38].

| Atom | $E_I$ | $E_t$ | Muonium formation fractions |
|---|---|---|---|
| He | 24.587 | 11.04 | 0 |
| Ne | 21.565 | 8.02 | $0.06 \pm 0.05$ |
| Ar | 15.760 | 2.22 | $0.74 \pm 0.04$ |
| Kr | 14.000 | 0.46 | $1.00 \pm 0.05$ |
| Xe | 12.130 | −1.41 | $1.00 \pm 0.04$ |

### 3.4.2 Gas Impurity

Muonium is a highly reactive paramagnetic atom. In order to avoid depolarization through collisions and chemical reactions, a pure inert gas, krypton, is used. Its purity is better than 99.999%. The cross section of the electron-spin exchange collision between muonium and molecular oxygen is very large ($\sim 10^{-16}$ cm$^2$) [39, 40]. Therefore, the molecular oxygen impurity must be kept very low.

The gas impurity was evaluated by using a quadrupole mass spectrometer.

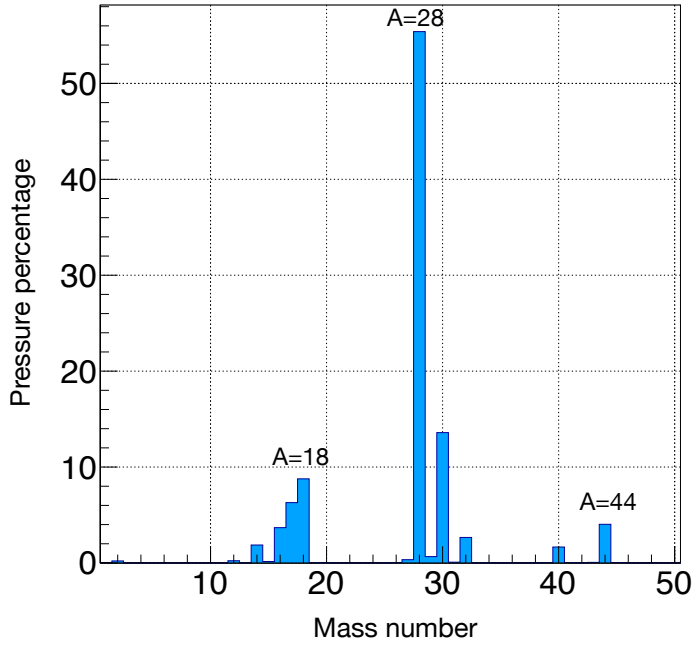


Figure 3.8: Gas impurity measurement in the gas chamber by Q-mass spectrometer before filling Kr gas. The mass numbers 18, 28, and 44 represent water ($H_2O$), nitrogen molecule ($N_2$), and carbon dioxide ($CO_2$), respectively. The mass numbers 16 and 17 correspond to the fragments of $H_2O$. The gas with mass number 30 came from a cold cathode gauge, which was detached from the chamber during the HFS measurement.

Figure 3.8 shows relative pressures for each mass number before filling Kr gas in June 2017. The result was consistent with a previous measurement in 2016. The systematic effect due to the gas impurity is discussed in Ch. 6

### 3.4.3 Extrapolation to Zero Gas Density

The quantity of gas density shift was reported by Thompson *et al*. as follows [41],

$$\Delta\nu_{\mathrm{Mu}}(D) = \Delta\nu_{\mathrm{Mu}}(0)\left(1 + aD + bD^2\right), \tag{3.3}$$

where $D$ is the gas density at 0 °C, $a$ is the coefficient of the linear density shift, and $b$ is the coefficient of the quadratic density shift. $a$ and $b$ are experimentally determined. Their values are $a = -10.66\,(10) \times 10^{-9}/\mathrm{torr}$ and $b = 9.7\,(2.0) \times 10^{-15}/\mathrm{torr}^2$.

Figure 3.9 shows a plot of the monitored gas pressure as the vertical axis and the time as the horizontal axis, and the histogram of the gas pressure is shown in Fig. 3.10. As a result, the fluctuation of the gas pressure is about 20 Pa.

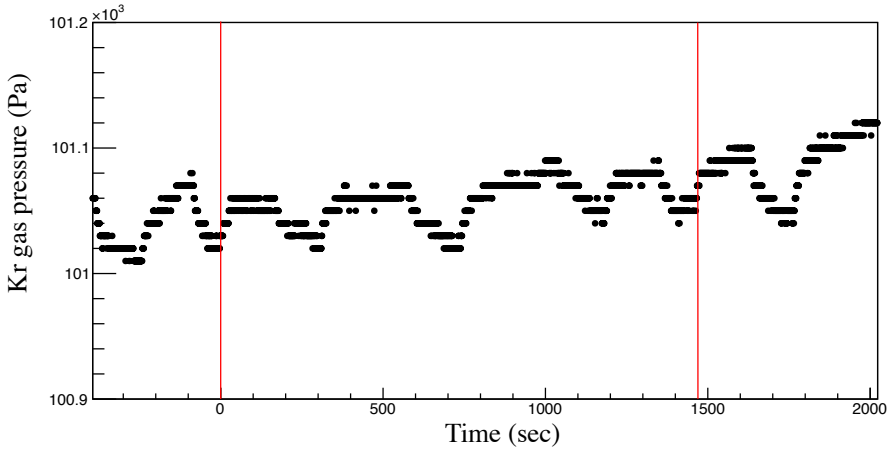


Figure 3.9: Time variation of monitored Kr gas pressure. The red line indicates the time when the microwave frequency was changed.

The gas temperature was controlled by a chiller with a temperature feedback system, and was also measured to calculate the gas density at $0°\mathrm{C}$ as shown in Fig. 3.11. Fluctuation of the gas temperature was about $0.17°\mathrm{C}$.

## 3.5 Microwave System

The probability of muon spin flip depends on the injected microwave frequency and power. Therefore a stable microwave injection system is necessary. A signal generator was used to control the power and frequency of the injected microwave. The resonance frequency of the microwave cavity was tuned by a 20 mm×100 mm×5 mm$^t$ aluminum plate and a piezo actuator. Figure 3.12 shows the circuit diagram of the microwave system. The microwave from a signal generator (R&S SMBV-B106) was amplified and injected to the cavity. A part of the microwave was picked up by an antenna inside the cavity and monitored by a power meter (R&S NRP2).

### 3.5.1 Microwave Cavity

Two microwave cavities were produced. One is for the resonance mode TM110, and its length and diameter are 230 mm and 81 mm, respectively, and the other one is for the TM220 mode, and its length and diameter are 330 mm and 180 mm, respectively. A TM110 cavity is easy to design because other resonance modes

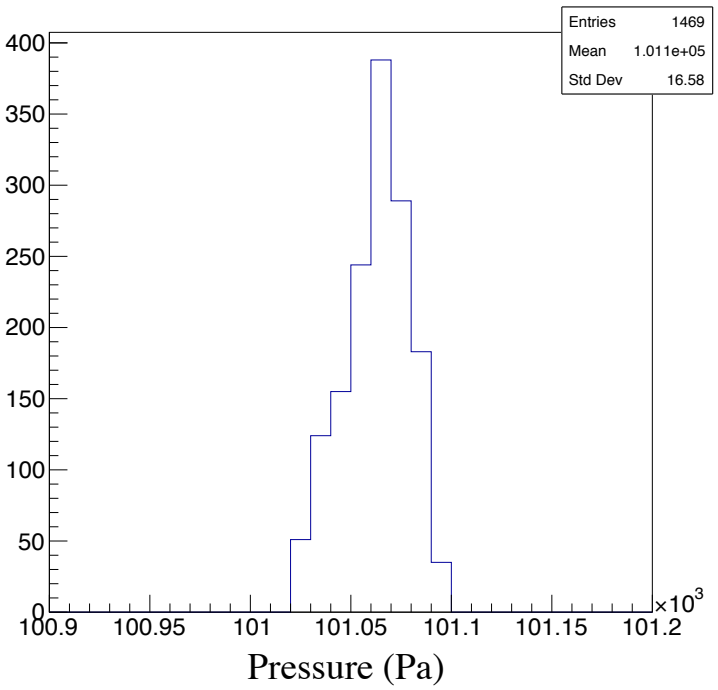


Figure 3.10: Representative histogram of the Kr gas pressure during the measurement.

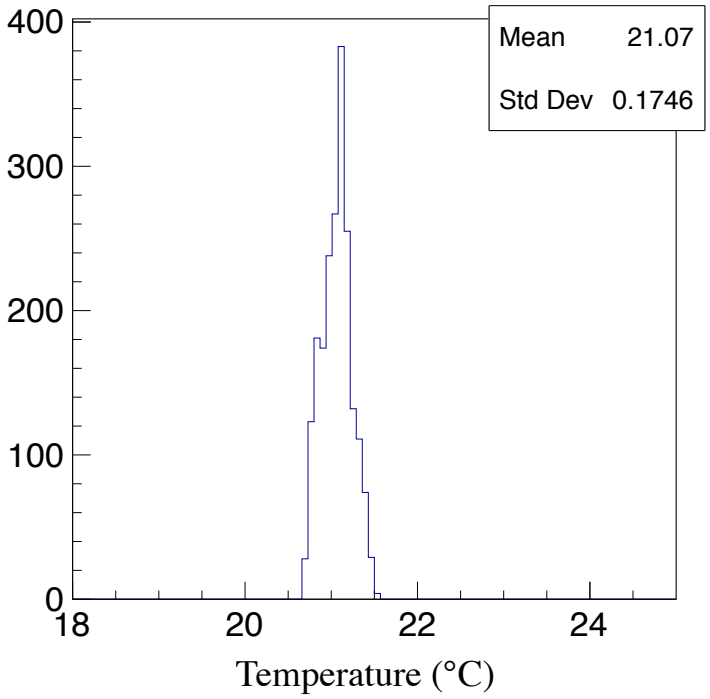


Figure 3.11: Representative histogram of the gas temperature.

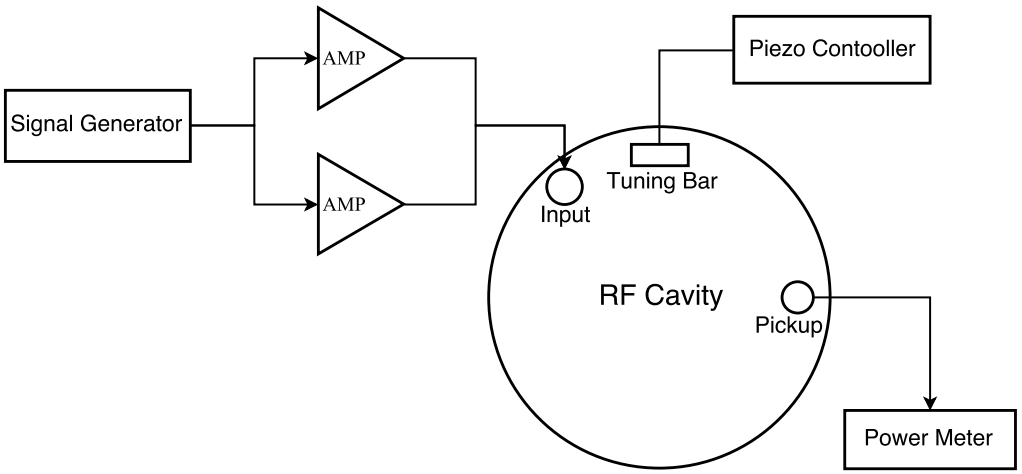


Figure 3.12: Schematic circuit diagram of the microwave system. The stability of the input power was monitored by a power meter. The resonance frequency of the cavity was tuned by an aluminum tuning bar.

are limited. However, the diameter of the cavity is smaller than the muon stopping distribution. Therefore, many muons would stop on the wall of the cavity where microwave is not induced and become background. On the contrary, the design of a TM220 cavity is a little more difficult due to other resonance modes, however almost all muonium can contribute by feeling the magnetic field of the microwave. Therefore the signal to noise ratio is much improved.

The number of stopping muons in the cavity was estimated by a Geant4 simulation. As a result, the ratio of the number of stopping muons to the number of injected muons was $38.1\%$ and $93.8\%$ for the TM110 cavity and TM220 cavity, respectively. The number of muoniums which feel the microwave magnetic field is increased by $2.5$ times by using the TM220 cavity instead of the TM110 cavity. Namely, the statistics is improved by $2.5$ times.

In the previous experiment at J-PARC in June 2016, the TM110 cavity was used, while the TM220 cavity was used in this experiment in June 2017. Pictures of the TM220 cavity is shown in Fig. 3.13.

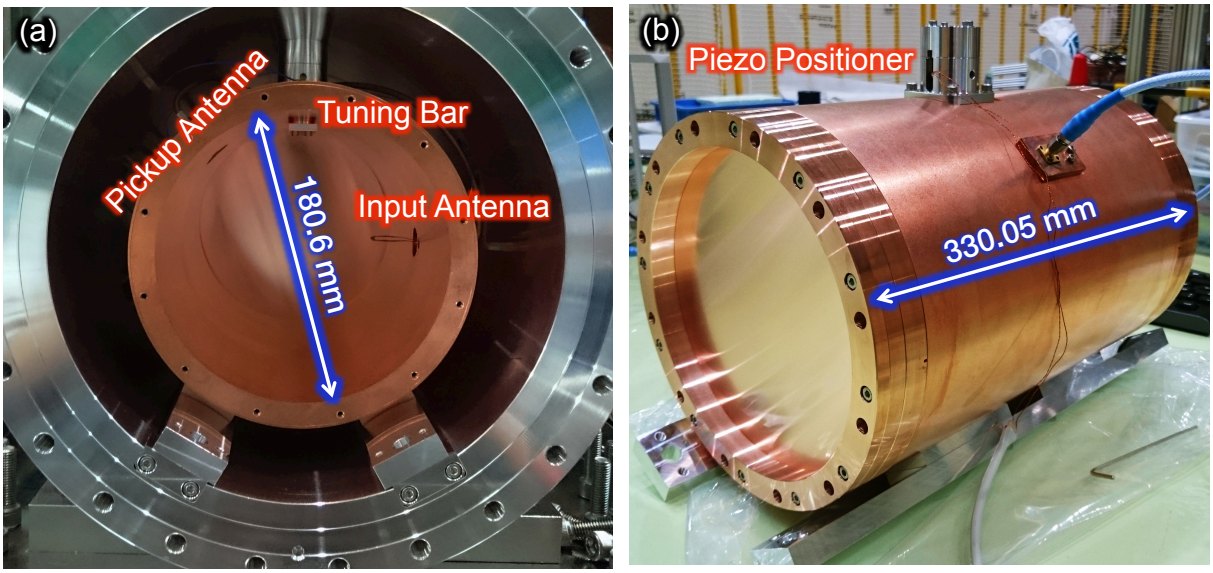


Figure 3.13: The TM220 cavity. (a) shows an inside view of the cavity. There were two antennas for injecting microwave and picking up a part of the stored microwave in the cavity to monitor stored energy. The resonance frequency was controlled by an aluminum tuning bar. (b) shows the whole cavity. There was a piezo positioner at the top of the cavity used to move the tuning bar.

### 3.5.2 Distribution of the Microwave Intensity in the Cavity

It is important to understand the intensity of the microwave field distribution on the resonance because the shape of the muon spin-flip resonance-signal depends on the muon stopping distribution and the magnetic field distribution in the microwave cavity.

For the $\mathrm{TM}_{mn0}$ mode of a cylindrical cavity [42, 43], the magnetic field in cylindrical coordinates is described as

$$\begin{aligned} H_r &= -A\frac{j\omega\epsilon}{k_c^2}\frac{m}{r}J_m\left(\frac{j_{mn}}{R}r\right)\sin(m\theta), \\ H_\theta &= -A\frac{j\omega\epsilon}{k_c^2}\frac{j_{mn}}{R}J'_m\left(\frac{j_{mn}}{R}r\right)\cos(m\theta), \\ H_z &= 0, \\ \omega^2\epsilon\mu &= k_c^2 = \left(\frac{j_{mn}}{R}\right)^2. \end{aligned} \tag{3.4}$$

Below is a variation of the expression in Eq. 3.4.

$$\begin{aligned} H_r &= -A\frac{j\omega\epsilon}{2k_c}\left(J_{m-1}\left(\frac{j_{mn}}{R}r\right)+J_{m+1}\left(\frac{j_{mn}}{R}r\right)\right)\sin(m\theta), \\ H_\theta &= -A\frac{j\omega\epsilon}{2k_c}\left(J_{m-1}\left(\frac{j_{mn}}{R}r\right)-J_{m+1}\left(\frac{j_{mn}}{R}r\right)\right)\cos(m\theta). \end{aligned} \tag{3.5}$$

The square of the microwave magnetic field intensity is

$$\begin{aligned} |H|^2 &= |H_r|^2+|H_\theta|^2 \\ &= A^2\frac{\omega^2\epsilon^2}{4k_c^2}\left(J_{m+1}^2\left(\frac{j_{mn}}{R}r\right)+J_{m-1}^2\left(\frac{j_{mn}}{R}r\right)-2J_{m+1}\left(\frac{j_{mn}}{R}r\right)J_{m-1}\left(\frac{j_{mn}}{R}r\right)\cos(2m\theta)\right). \end{aligned} \tag{3.6}$$

The quality factor, $Q$, is given by

$$Q=\omega\frac{W}{P}, \tag{3.7}$$

where $W$ is total energy of the microwave in the cavity, and $P$ is the input power. Since the power of the magnetic field $W_M$ is equal to one of the electric field $W_E$, $W$ can be described as

$$\begin{aligned} W &= W_E+W_M=2W_M \\ &= \mu\int_V |H|^2\,dV \\ &= A^2\frac{\omega^2\epsilon^2\mu}{4k_c^2}\int_0^R\int_0^{2\pi}\int_0^h\left(J_{m+1}^2\left(\frac{j_{mn}}{R}r\right)+J_{m-1}^2\left(\frac{j_{mn}}{R}r\right)\right. \\ &\quad \left.-2J_{m+1}\left(\frac{j_{mn}}{R}r\right)J_{m-1}\left(\frac{j_{mn}}{R}r\right)\cos(2m\theta)\right)r\;dr d\theta dz \\ &= 2\pi A^2h\frac{\epsilon}{4}\int_0^R r\left(J_{m+1}^2\left(\frac{j_{mn}}{R}r\right)+J_{m-1}^2\left(\frac{j_{mn}}{R}r\right)\right)dr \\ &= \frac{1}{2}\epsilon A^2VJ_{m+1}^2(j_{mn}), \end{aligned} \tag{3.8}$$

in which $V(=\pi R^2h)$ is the volume of the cavity. Using Eqs. 3.6, 3.7, and 3.8, we

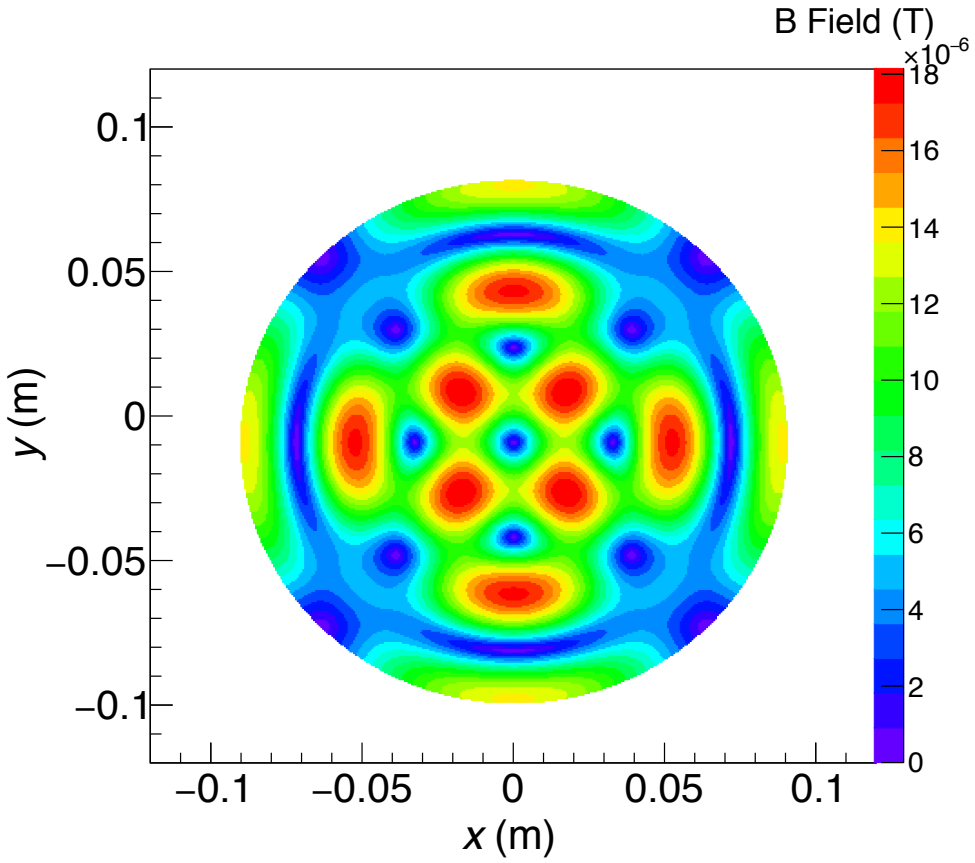


Figure 3.14: Magnetic field intensity of the TM220 microwave cavity. In the calculation, $Q = 20000$, and an input power $P = 0.8$ W were used.

obtain

$$|H|^2 = \frac{PQ}{2\omega\mu} \frac{1}{V J_{m+1}^2(j_{mn})} \left( J_{m+1}^2\left(\frac{j_{mn}}{R}r\right) + J_{m-1}^2\left(\frac{j_{mn}}{R}r\right) - 2J_{m+1}\left(\frac{j_{mn}}{R}r\right) J_{m-1}\left(\frac{j_{mn}}{R}r\right) \cos(2m\theta) \right). \tag{3.9}$$

The calculation result of the magnetic field intensity for a TM220 cavity with a diameter of 180 mm is shown in Fig. 3.14

The distribution of the magnetic field of the TM220 cavity was also evaluated by using a simulation software (AER, INC. CST microwave studio). Figure 3.15 shows the results of the simulation. The result are almost consistent with the analytic calculation, but the field of the microwave was rotated due to the tuning bar. The

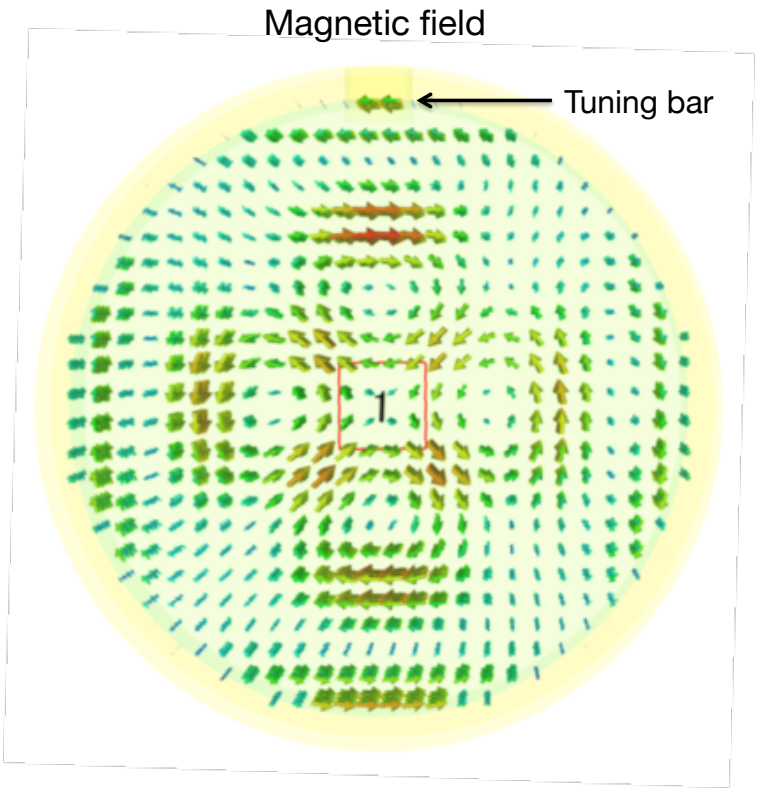


Figure 3.15: Simulation result of the magnetic field of the microwave by CST microwave studio. The arrows indicate the direction of the magnetic fields and their sizes represent the intensity of the magnetic fields. In the calculation, the aluminum tuning bar was considered.

uncertainty of the microwave field rotation will be discussed in Sec. 6.1.

### 3.5.3 Measurement of the Quality Factor of the Cavity

It is important to measure the quality factor of the cavity because the stored energy of the microwave in the cavity depends on it. The quality factor of the TM220 cavity was calculated from the ratio of the reflected power to the injected power, which is called S11 parameter, by using a vector network analyzer (VNA).

Figure 3.16 shows a block diagram of the quality factor measurement system. The VNA was connected to the two antennas of the cavity. First, the tuning bar was moved to the position where the S11 parameter was minimum at the target frequency. Then, the quality factor was obtained by fitting the frequency dependence of the S11 parameter as a function composed of a gaussian plus a linear constant as shown in Fig. 3.17. The result of the quality factor measurement appears in Fig. 3.18.

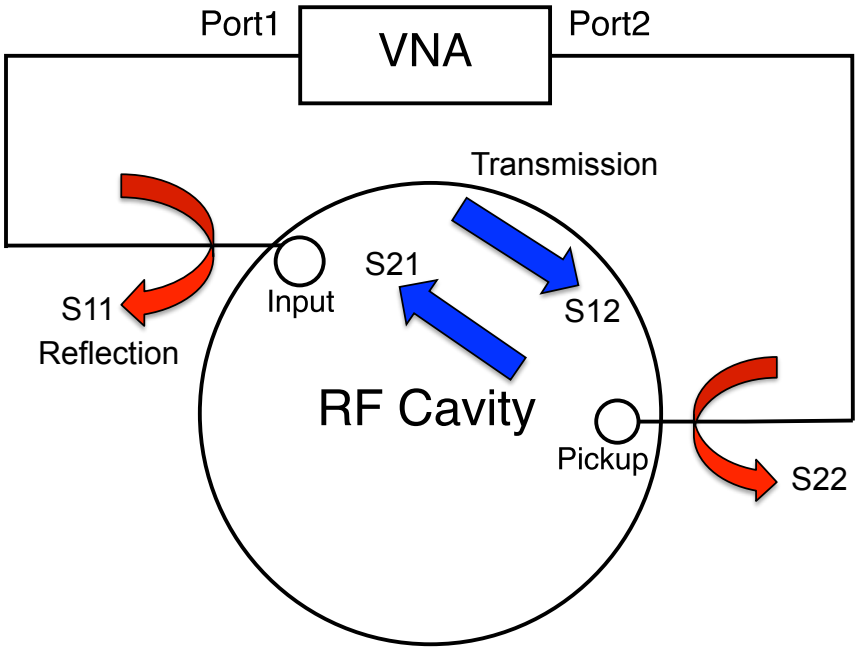


Figure 3.16: Diagram of the quality factor measurement

This result indicates that the quality factor depends on the resonance frequency of the cavity. Therefore, the time integral method with a simple Lorentzian fitting is inapplicable.

### 3.5.4 Microwave Power Monitoring

A part of the microwave was picked up by one of the antenna and monitored. This monitor recorded the picked up microwave power with a time interval of 5 seconds. Figure 3.19 shows the time variation of the monitored microwave power. A microwave power drop was observed in several measurements. This power drop was caused by the thermal expansion of the cavity. The heat source was the injected microwave power. This problem could be improved by using a water cooling system. The systematic uncertainty of the power drop will be discussed in Ch. 6.

## 3.6 Positron Detector

Changes in the number of decay positrons by the muon spin flip were detected by two types of detectors. One is composed of segmented scintillation counters with

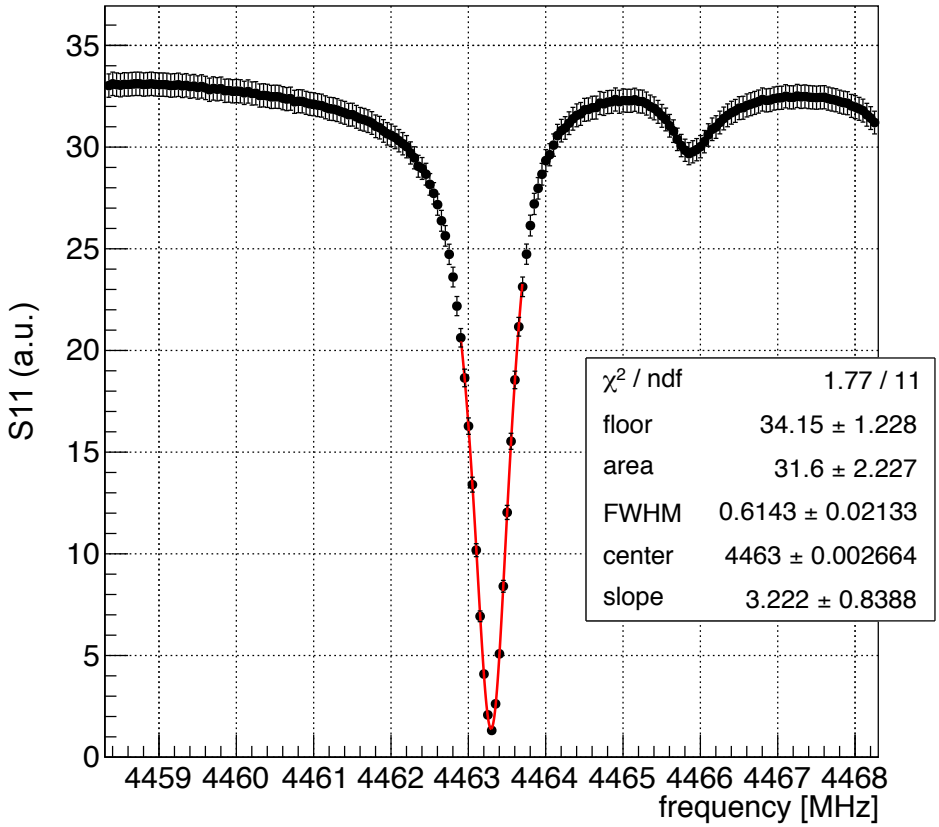


Figure 3.17: Representative result of the frequency characteristics measurement. The microwave frequency of the signal generator was tuned to the peak which was obtained by fitting. The quality factor was calculated from the peak height and width.

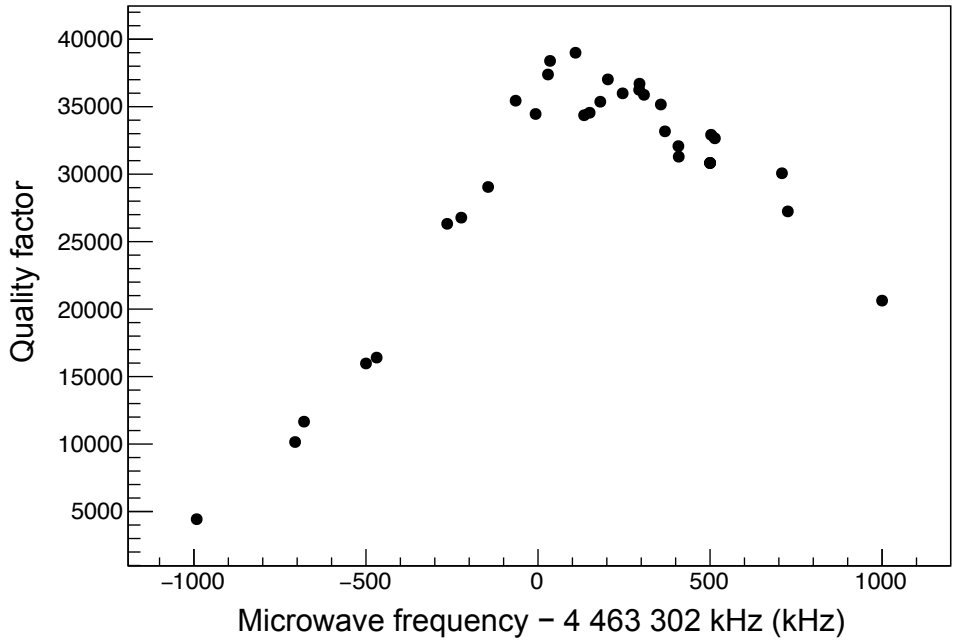


Figure 3.18: Results of the quality factor measurement. The horizontal axis and the vertical axis correspond to the results of the peak center and the quality factor obtained in Fig. 3.17, respectively.

MPPCs. The other is a single-sided silicon strip detector. These detectors must be stable in a high-rate counting environment caused by high-intensity muon beam. To achieve this requirement, these detectors were highly segmented.

### 3.6.1 Segmented Scintillation Detector

This detector consists of 576 $(24\times24)$ plastic scintillators. The size of each pixel was 10 mm square and 3 mm thick. A multi-pixel photo counter (MPPC, Hamamatsu Photonics K.K. S12825-050P-01) was connected to each pixel. In the experiment in June 2017, these detectors were not stable due to a miss-operation of the high voltage control, and after pulses were observed. This problem can be improved by providing appropriate voltage to the MPPCs.

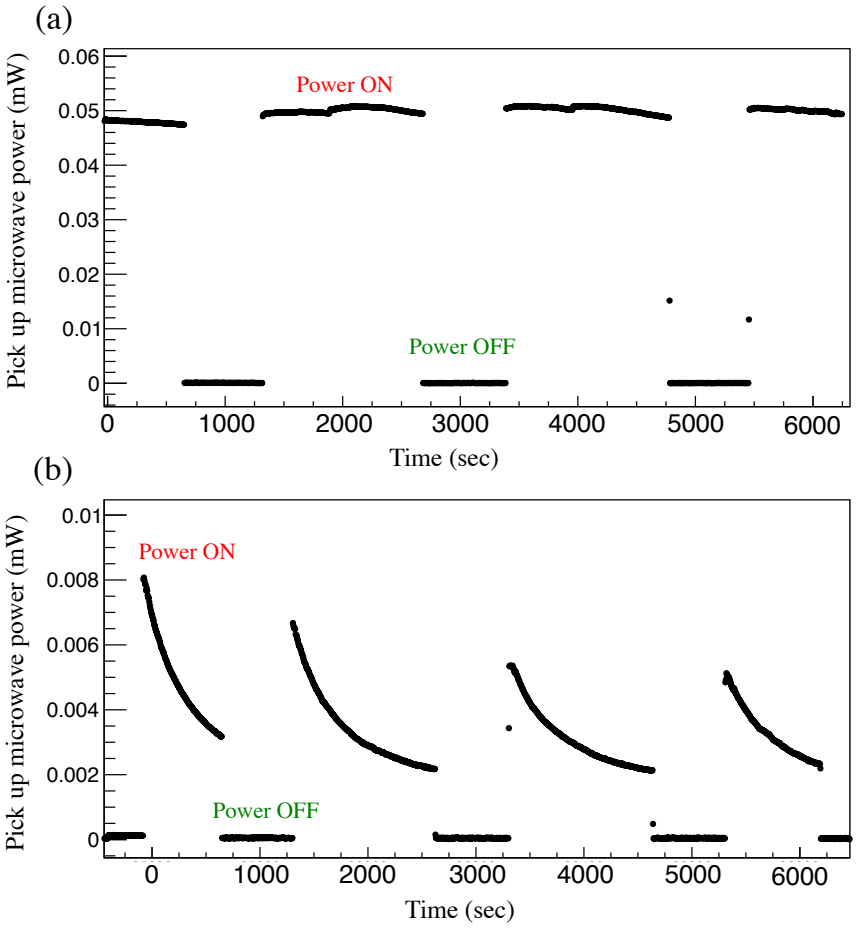


Figure 3.19: Time variation of the picked up microwave power. (a) shows a representative run in which the microwave power fluctuation was relatively small. (b) represents a run where the microwave power was decreasing.

### 3.6.2 Single-sided Silicon Strip Detector

A silicon strip detector is very useful for experiments in which high-intensity pulsed beam is used. The sensor is highly segmented with pitch in the order of 100 $\mu$m. Therefore, the pileup rate is low. A silicon detector also has a good time resolution.

For precise time measurements, a silicon strip detector, which consists of an original silicon strip sensor and an original readout circuit optimized for our experiment, was developed.

The original silicon strip detector was mainly developed for the precise measurement of the muon $g-2$/EDM at J-PARC. For this measurement, the detector must measure the decay positron momentum, time, and the number of positrons. The measurement environment is in a high magnetic field of 3 T, with high-rate fluctuation during the measurement time from 1.4 MHz to 140 kHz, and in vacuum. The requirements and conditions are similar in our measurement. Therefore, this sensor is also suitable for our muonium HFS measurement.

#### Silicon Strip Sensor

Figure 3.20 shows pictures of the silicon strip sensor for the muon $g-2$/EDM experiment at J-PARC. The specification of this sensor is summarized in Table 3.2.

Table 3.2: Specification table of the silicon strip sensor.

| Item | Specification |
|---|---|
| Sensor type | p on n, AC |
| Sensor size | 98.77 mm × 98.77 mm |
| Sensor thickness | 320 $\mu$m |
| Number of Strips | 512 strips× 2 blocks |
| Strip pitch | 190 $\mu$m |
| Strip length | 48.575 mm |
| Backside metal | Aluminum |

The characteristics of this sensor are that it is divided into two blocks to improve the strip occupancy, and that it is possible to connect the chips from either the vertical or horizontal direction by its double metal structure. The detector electrical characteristics was studied for quality assurance by a probing test as detailed in Appendix B. The strip area is smaller than the pixel area of the segmented scintillator.

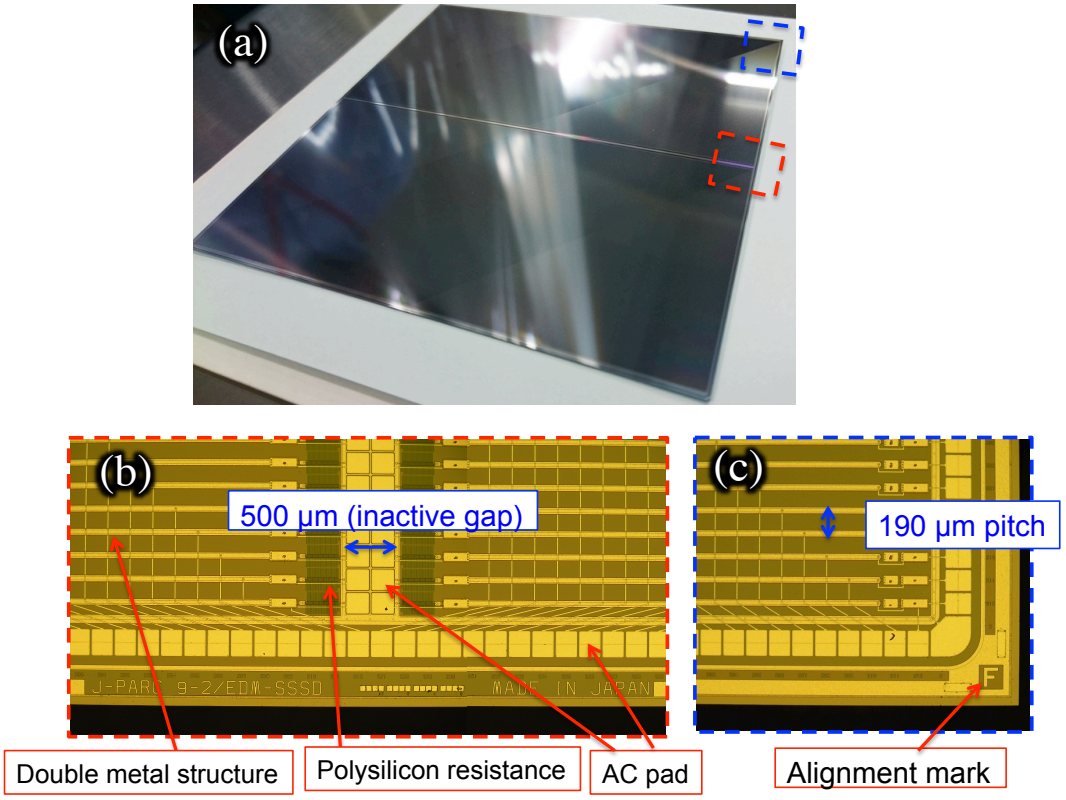


Figure 3.20: The silicon strip sensor developed for the muon $g-2$/EDM experiment at J-PARC. (a) shows a picture of the whole silicon strip sensor, and (b) and (c) are microscope views at the center and the corner of the sensor, respectively.

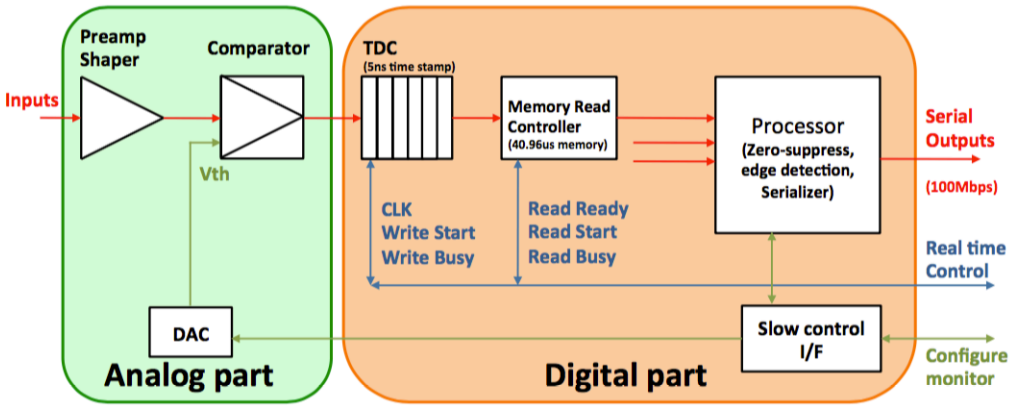


Figure 3.21: Block diagram of SliT128A. The SliT128A is an analog/digital combined type integrated circuit.

### Readout Circuit

An original Application-Specific-Integrated-Circuit (ASIC) named "Slit" was developed. The latest version of the Slit, which is named SliT128A, was produced. The process of the SliT128A is Silterra CMOS 0.18 $\mu$m. The SliT128A is an analog/digital combined type integrated circuit. The signal from the silicon strip sensor is amplified, shaped, discriminated, and digitized, then the hit timing is recorded with a 5-ns time stamp over a time range of 40.96 $\mu$s. Figure 3.21 shows a block diagram of the SliT128A [44].

Four SliT128As were mounted on the circuit board, named multi-SliT128A board, and were controlled and readout by a Field-Programmable Gate Array (FPGA, XILINX ARTIX-7) directly mounted on the board. The chips were glued by a conductive sliver paste (DOTITE D-500) to provide bias voltage, and connected to the board with 25-$\mu$m aluminum wires. The FPGA communicated with a PC via an optical fiber. Figure 3.22 shows a photograph of the multi-SliT128A board.

A performance test of the SliT128A was conducted by using test pulses. The pulses simulated minimum ionization particle (MIP) positron signal. The results are summarized in Table 3.3.

For the time differential method, the time calibration is important. The clock for the multi-SliT128A boards was provided from a function generator (Tektronix AFG3252C), which has on accuracy of 1 ppm. The effect of the uncertainty of the

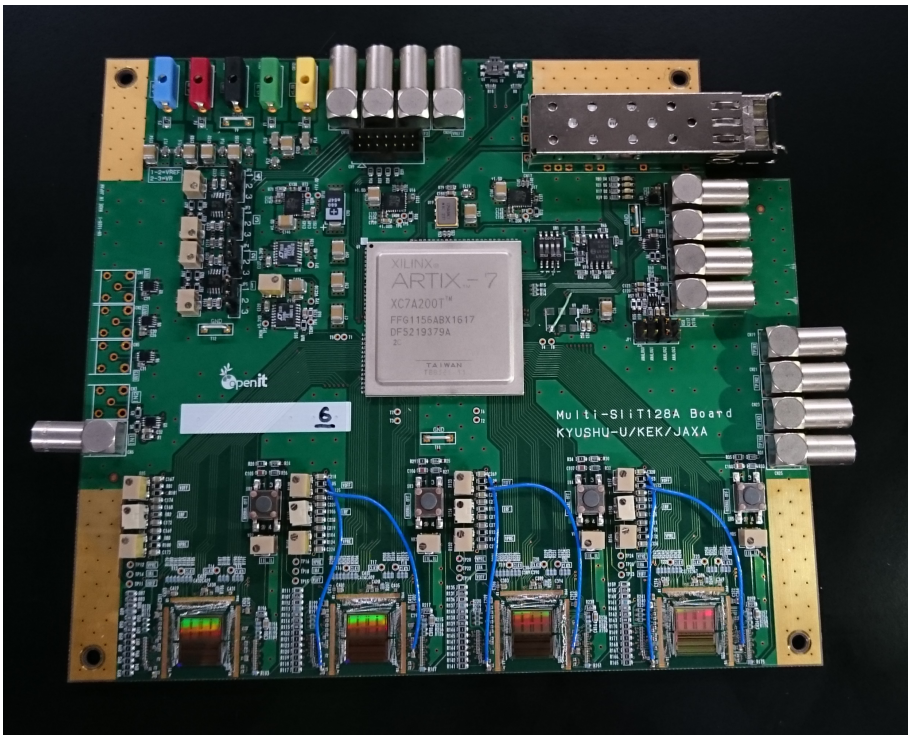


Figure 3.22: Multi-SliT128A board. Four chips were controlled by the FPGA.

Table 3.3: The results of the performance tests of SliT128A.

| Parameter | Performance |
|---|---|
| Dynamic range | 4 MIP |
| Equivalent Noise Charge (ENC) | 430 $e^-$ |
| Pulse width | 155 ns |
| Time walk (0.5 - 3 MIP threshold) | 11.5 ns |

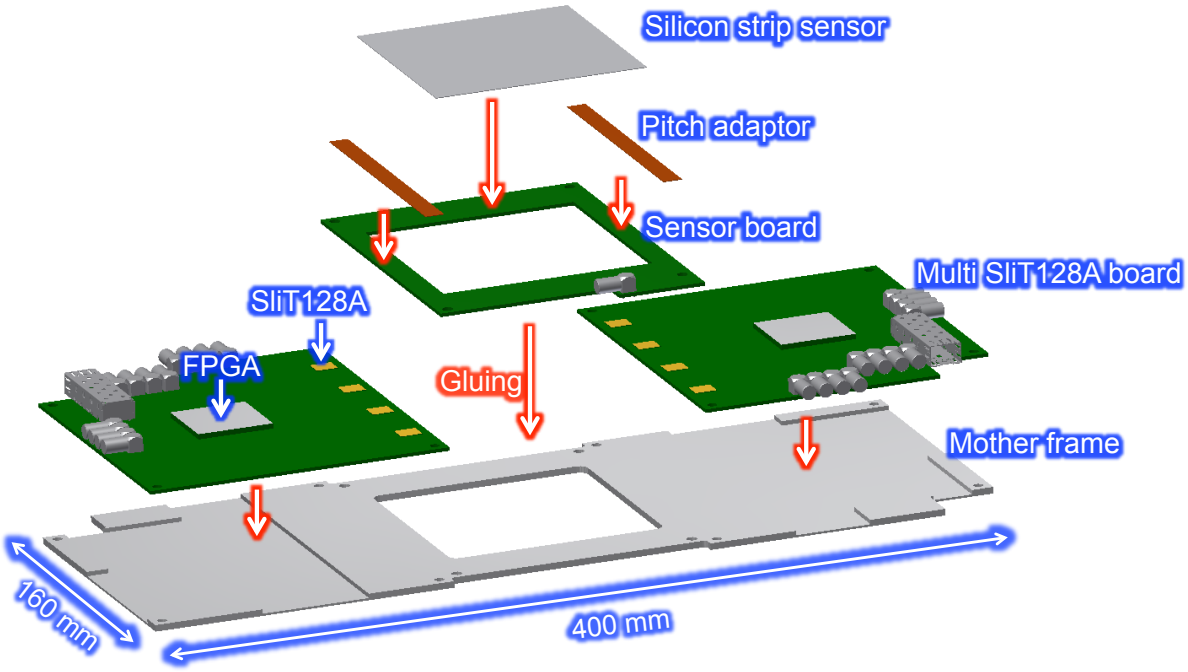


Figure 3.23: Schematic view of the silicon strip detector. The silicon strip sensor and two pitch adaptors were glued on the sensor board, and the sensor board and two multi-SliT128A boards were glued on the mother frame made of aluminum. The sensor, pitch adaptors and SliT128As were connected by wire bonding.

time calibration will be discussed in Ch. 6.

### Silicon Strip Detector Construction

Figure 3.23 shows a schematic view of the design of the silicon strip detector for this experiment. The sensor was glued on the sensor board, which also provides bias voltage to the sensor. Eight SliT128A were mounted on two circuit boards to readout the whole sensor. Both the sensor board and the two circuit boards were glued on an aluminum mother frame as shown in Fig. 3.24. The silicon strip sensor was connected to the chips via two pitch adaptors. The pitch adaptors have 512 lines to read out a half side of the strip sensor and their minimum line/space is 20/22.5 $\mu$m, respectively. Figure 3.25 shows pictures of the pitch adaptor, and a picture of the constructed silicon strip detector is displayed in Fig. 3.26. For gluing of all the boards, pitch adaptors, and sensor, an insulated epoxy adhesive (Araldite Araldite2011) was used. This adhesive is a two-component liquid type, and it takes about a day for solidification at room temperature after mixing.

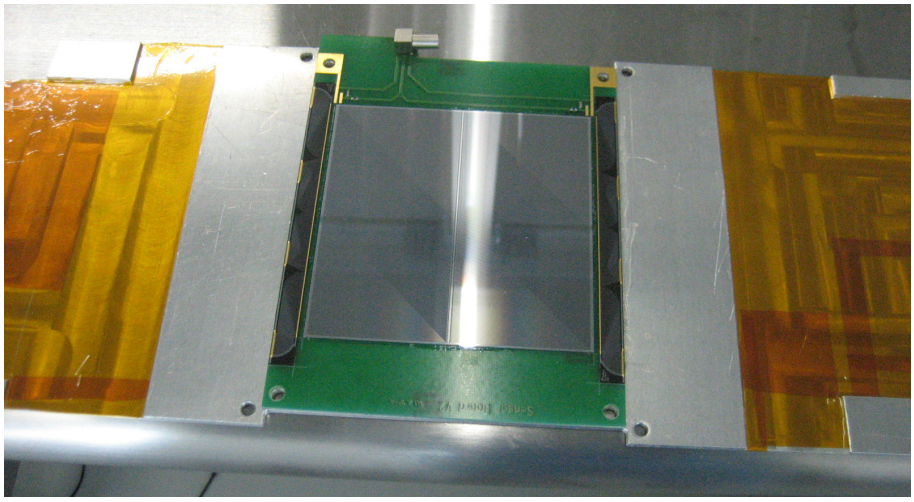

Figure 3.24: After gluing the sensor board on the aluminum mother frame. The mother frame had notches and was shielded by a Kapton tape to avoid electrical contact with the circuit boards.

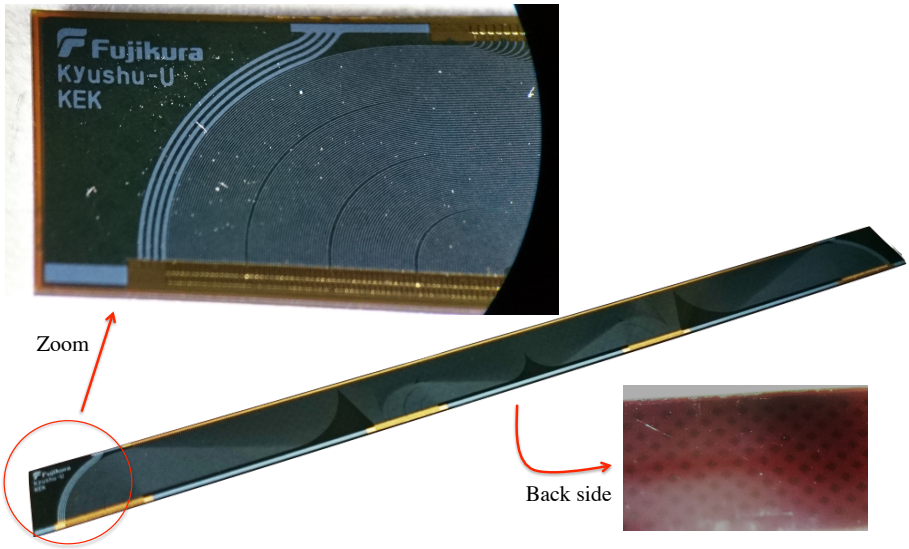


Figure 3.25: Pitch adaptor made by Fujikura K.K. The back side of the pitch adaptor was made of a copper mesh structure to control the curvature.

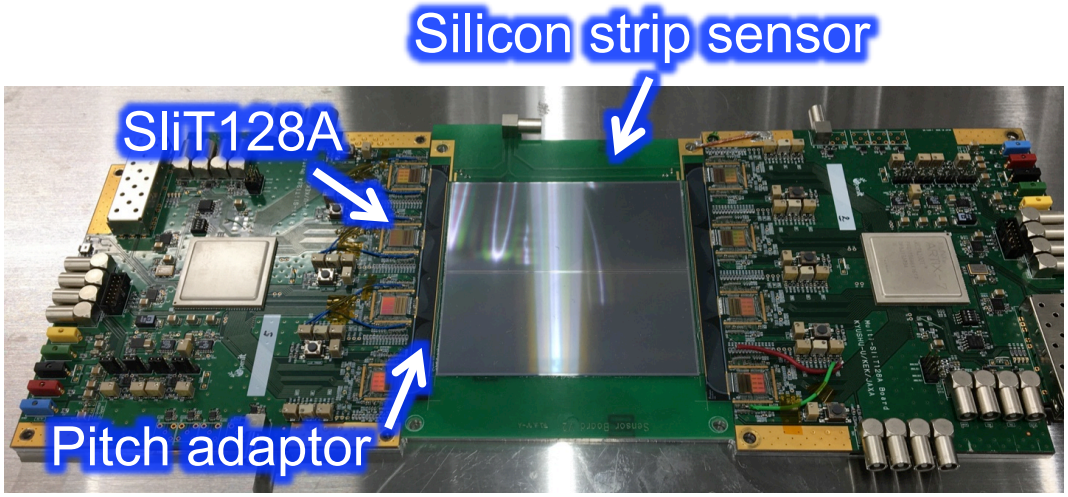


Figure 3.26: Completed silicon strip detector.

Before gluing the silicon strip sensor, the sensor quality was confirmed by the measurement of the sensor electrical characteristics as presented in Appendix B.

#### Silicon Strip Detector Performance Test

The silicon strip detector performance was estimated by using a test pulse simulating a minimum ionising particle (MIP) signal. Figure 3.27 shows results of the performance tests for several SliT128A. We confirmed that the average equivalent noise charge (ENC) was 1400 $e^-$. A signal to noise ratio of 21 was obtained. An uniform gain and an offset at 0.3 MIP threshold were also obtained. There were some channel dependence on an unit of 32 channels. This was because by the power supply to the chip that was not adequate to fully control the chips. This problem can be improved by a circuit upgrade.

## 3.7 Data Acquisition System

Figure 3.28 represents a block diagram of the data acquisition (DAQ) system. The DAQ system for the silicon strip detector was separated from that of the segmented scintillators. The DAQ trigger was distributed from the 25 Hz beam pulse, and was provided even when the muon beam was off, thus background level could be monitored.

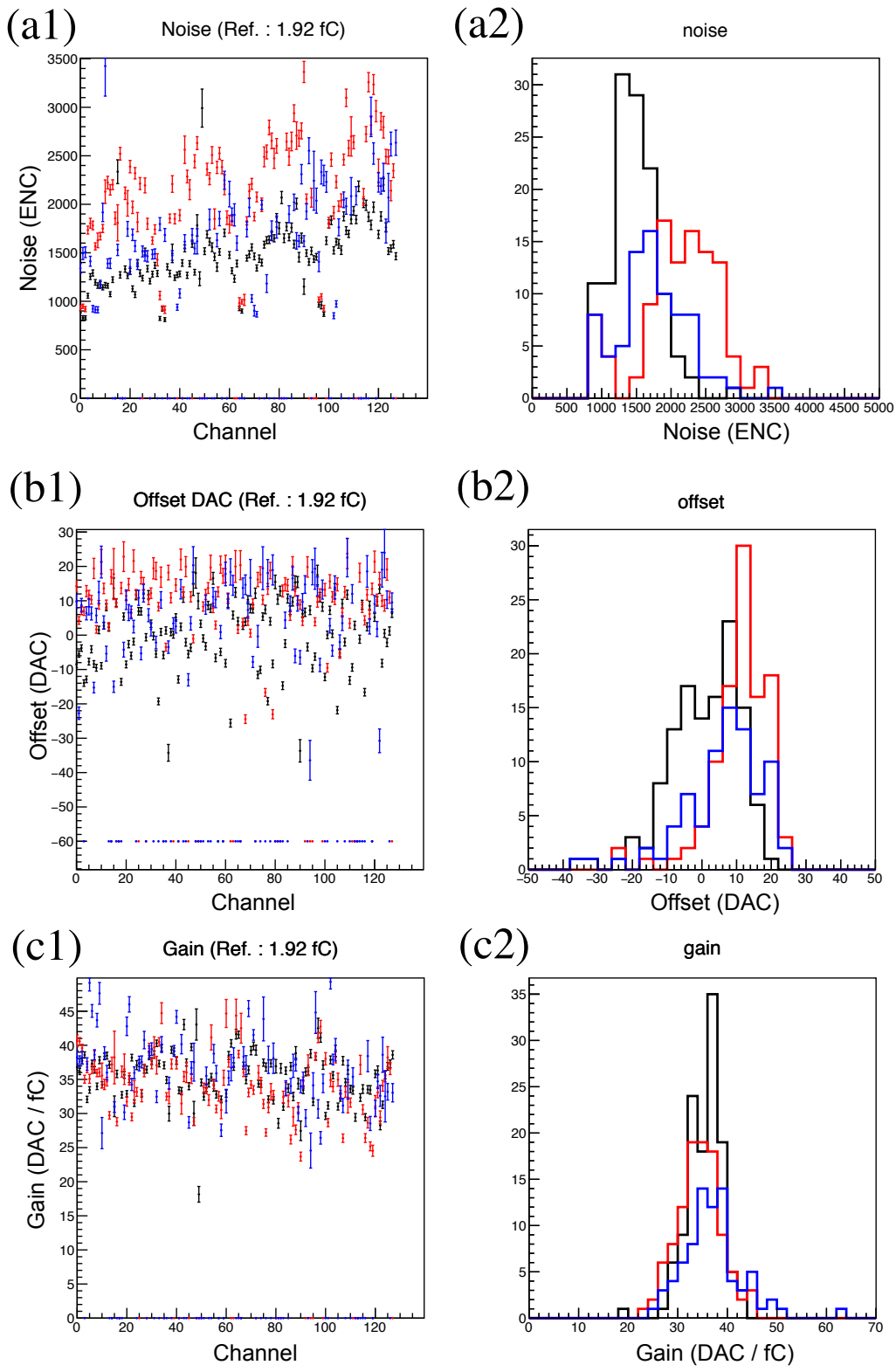


Figure 3.27: Summary plots of the performance tests of the silicon strip detector: (a) ENC distributions, (b) offset DAC distributions, and (c) gain distributions. For each 32 channels, there were some channel dependence due to a poor power supply, but this could be improved by a circuit upgrade.

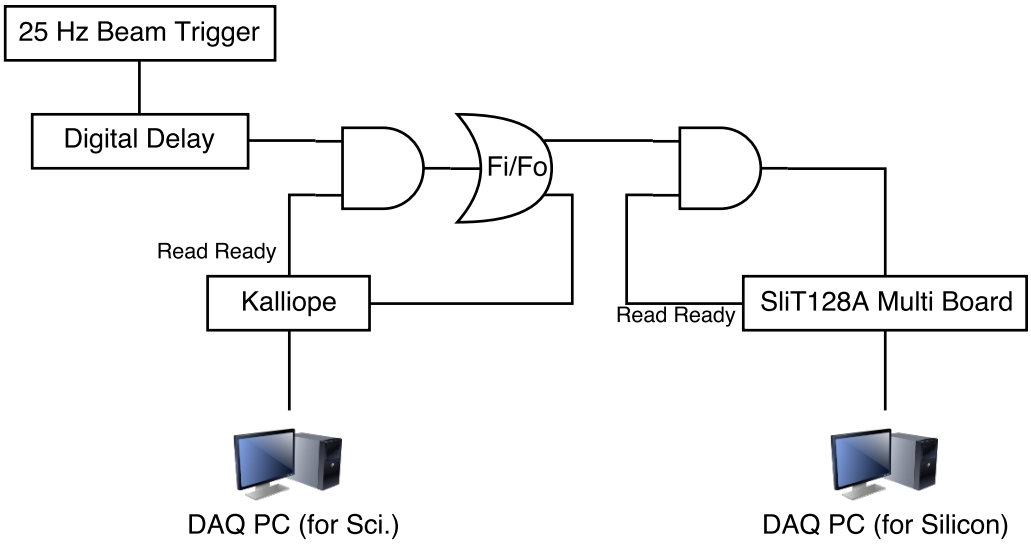


Figure 3.28: Block diagram of the trigger logic circuit. Two computers were used for the data acquisition. They also monitored the performance of the detectors.

# Chapter 4

# Simulation Study

This chapter describes the simulation study for the zero field experiment at J-PARC. First, the estimation of the positron hit rate of the silicon detector is described. Then, the estimation of the signal shapes obtained by the time differential method and the time integral method is discussed.

## 4.1 Simulation Setup

For the estimation of the muon stopping distribution and counting rate of decay positrons, a Geant4 simulation was used. For the signal form simulation of the time integral method and the differential method, the total number of detected positrons subjected to the microwave spin flip was calculated by using the muon stopping distribution from a Geant4 simulation, and then, the signal form was calculated by using Eqs. 2.53 and 2.60. The total number of simulated muons was $7.8 \times 10^{11}$.

The event display of the simulation is shown in Fig. 4.1. In the simulation, muons were injected from the beam pipe. The beam width was assumed to be 21.7 mm in the $x$ direction and 19.6 mm in the $y$ direction, and the value of the beam momentum was assumed to be $28.0$ MeV/$c$.

## 4.2 Estimation of the Counting Rate

The hit rate of the silicon detector for the experiment in June 2017 was estimated. The number of muons in a bunch is expected as $1.8 \times 10^5$ at the experimental area

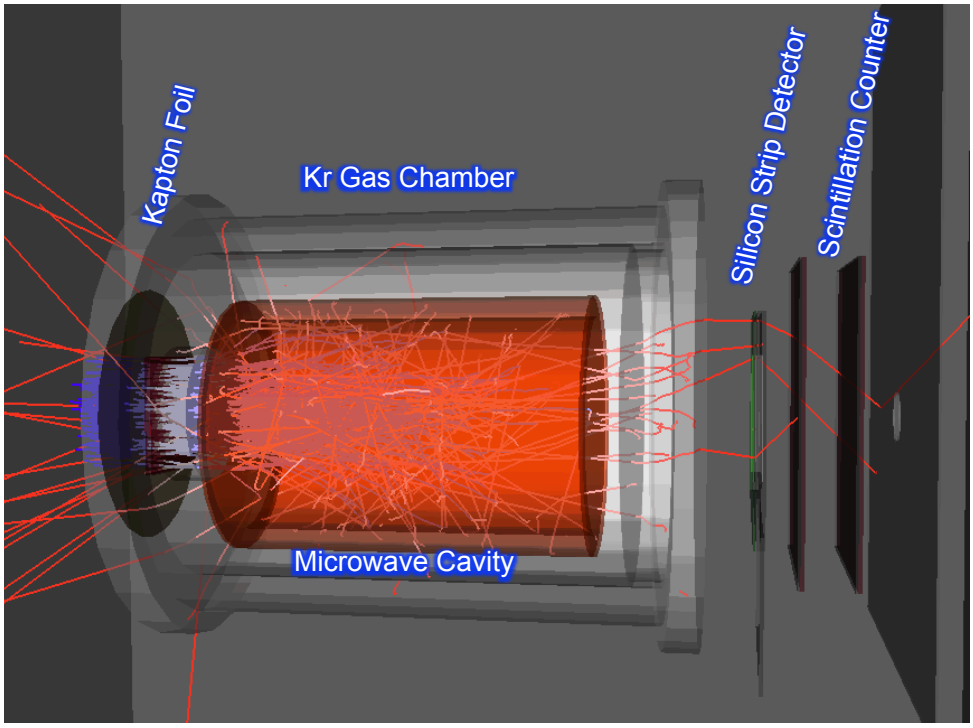


Figure 4.1: Geant4 simulation event display. Blue lines and red lines indicate muon and positron tracks, respectively.

when the proton beam power is 150 kW. Simulation results about the hit rate of the silicon detector are shown in Fig. 4.2. This figure indicates that the strip position dependence is negligibly small.

Average hit rate per strip per pulse was estimated to be 0.43 count. Therefore, the number of detected positron by the whole silicon detector was assumed as 440 hit per pulse.

## 4.3 Estimation of the Signal Shapes

The signal shapes in the time integral method and time differential method were estimated by a simulation. The muon stopping distribution was estimated by using Geant4 as shown in Fig. 4.3, and then, the number of positrons, which was counted by a detector, was calculated by using Eq. 2.53. The solid angle covering the detector and the microwave field distribution of the TM220 cavity discussed in section 3.5 were considered. The decay positron energy threshold, which is related to the signal amplitude, was estimated to be 30 MeV from the range of positron in aluminum for

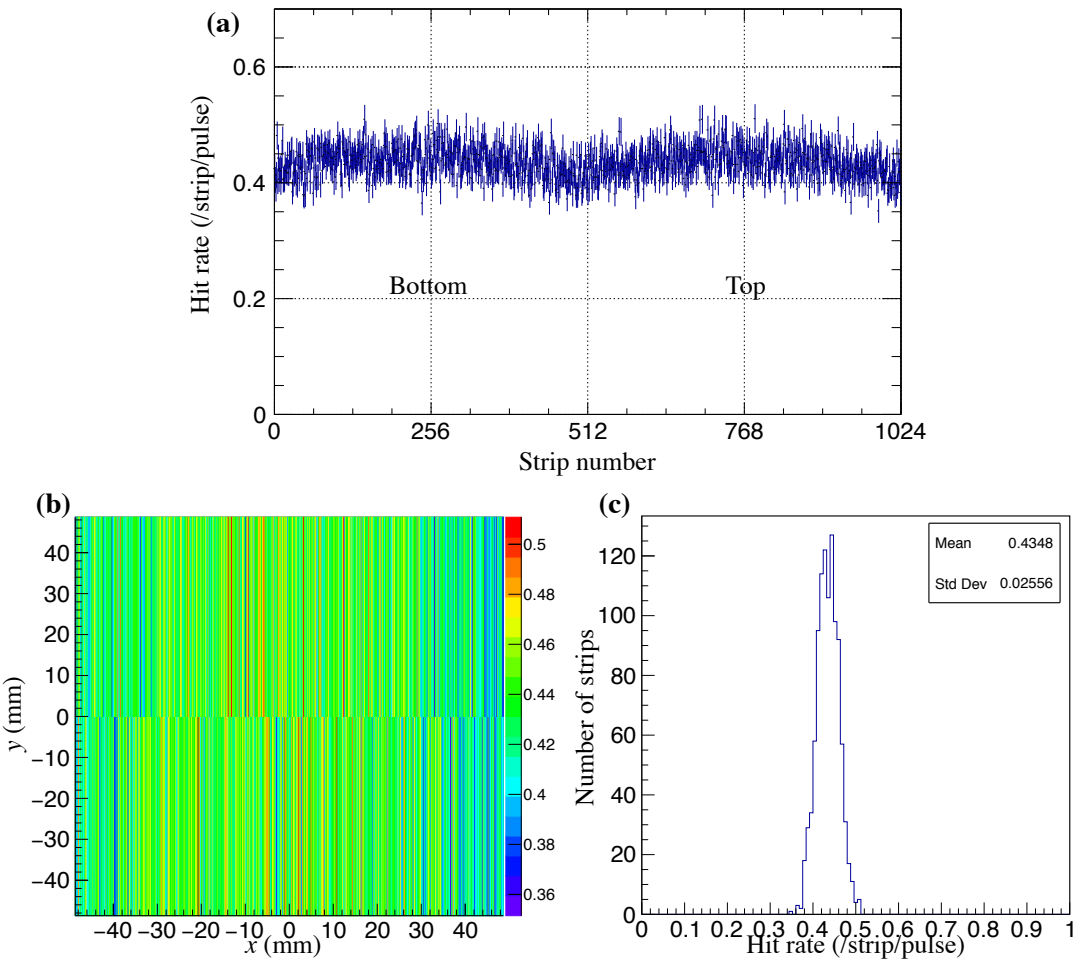


Figure 4.2: Hit rate of the silicon detector estimated by a Geant4 simulation. (a, b) show strip dependence of simulated hit rate. (c) shows the distribution of hit rate per strip.

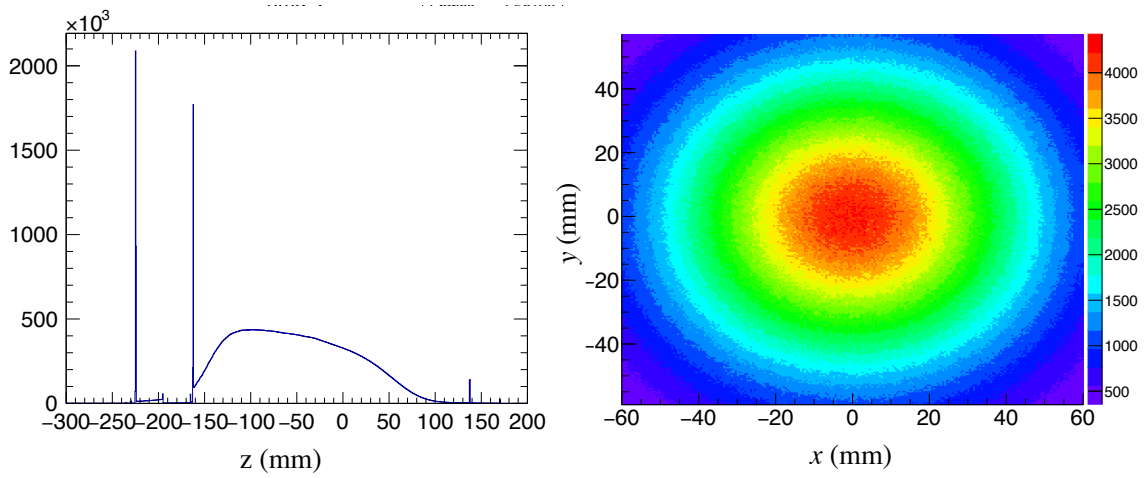


Figure 4.3: Simulation results for the muon stopping distribution. The left shows a projection on the beam axis and the right a distribution in the cavity projected on the plane perpendicular to the beam axis.

a flange with a thickness of 55 mm. The quality factor and stored microwave power were assumed to be 20000 and 0.8 W as ideal values, respectively.

### 4.3.1 Time Integral Method

In the simulation, the number of detected positron was calculated from the microwave field intensity and the number of stopping muon was simulated by Geant4. Then, the total number of detected positrons was integrated over the space and fluctuated by a Poisson distribution. Finally, the signal was calculated as $(N_{\mathrm{ON}} - N_{\mathrm{OFF}})/N_{\mathrm{OFF}}$ and was plotted with the signal as the vertical axis and the microwave frequency, $\nu_0$, as the horizontal axis. For each frequency, $7.8{\times}10^{10}$ muons were simulated.

The fitting function is expressed as

$$f_{\mathrm{int}}(\nu_0,\ p_1,\ p_2,\ \Delta,\ \lambda) = p_1 \sum \frac{\frac{aP}{2}\cos\theta}{1+\frac{\lambda}{\gamma}+\frac{aP}{2}\cos\theta} \frac{-2\left|p_2 b\right|^2\left(\gamma'^2+2\left|p_2 b\right|^2\right)}{\left(\gamma'^2+2\left|p_2 b\right|^2\right)^2+\gamma'^2(2\pi\Delta)^2}, \quad (4.1)$$

where $p_1$ is the signal amplitude scaling factor, $p_2$ is the power scaling factor, $\Delta = \Delta\nu - \nu_0$ is the difference between the microwave frequency and the muonium HFS frequency, and $1/\lambda$ is the spin relaxation time. The values of $p_1$, $p_2$, $\Delta\nu$, and $\lambda$ are free fitting parameters. The other two parameters, which were the muon decay rate $\gamma$ and the spin relaxation rate $\lambda$, were fixed as the inverse of Eq. 2.2 and

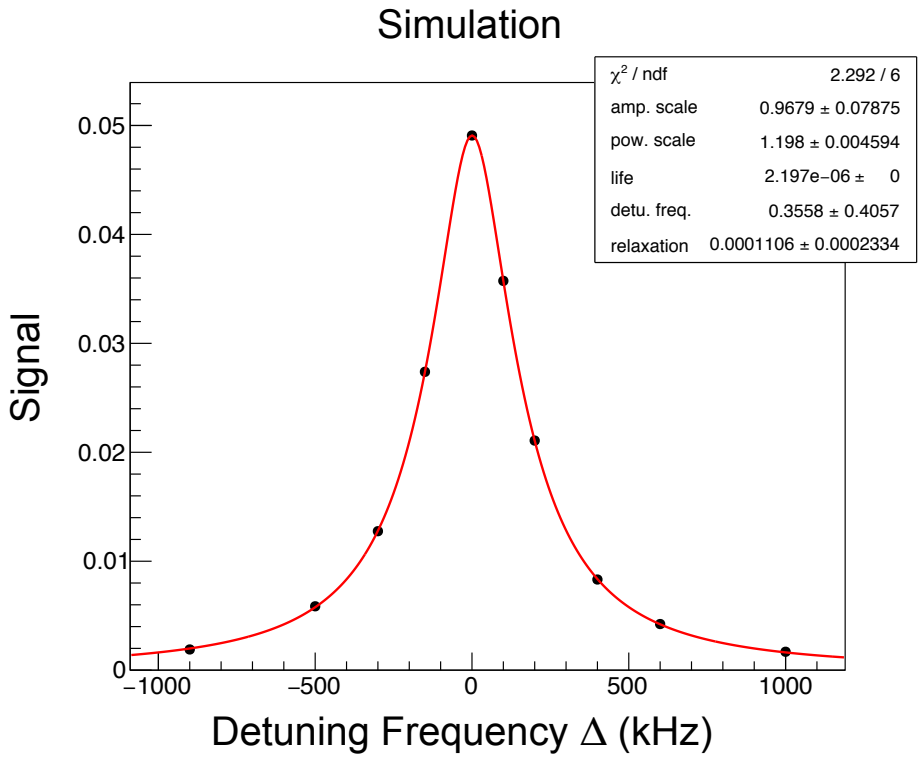


Figure 4.4: The simulation result of the time integral method. Amp. scale, pow. scale, life, detu. freq., and relaxation refer to the parameters $p_1$, $p_2$, $1/\gamma$, $\Delta$, and $1/\lambda$ in Eq. 4.1, respectively.

$1/200$ $\mu$s$^{-1}$, respectively.

The fitting function was not a single Lorentzian, but a summation of multiple Lorentzians that varied with the microwave power that the muonium feels at different location. It appears as the summation in Eq. 4.1.

Figure 4.4 shows the simulation results obtained by the time integral method. The precision of the muonium HFS frequency obtained by the time integral method was estimated to be 0.41 kHz. Note that this method is only applicable when the quality factor and injected microwave power are constant during the whole measurement.

### 4.3.2 Time Differential Method

The time differential signal shape was estimated in the same way as the time integral method. Simulation results of the time differential signals are plotted in Fig. 4.5 with the signal as the vertical axis and the time as the horizontal axis. The statistics for each frequency was the same as in the simulation of the time integral signal.

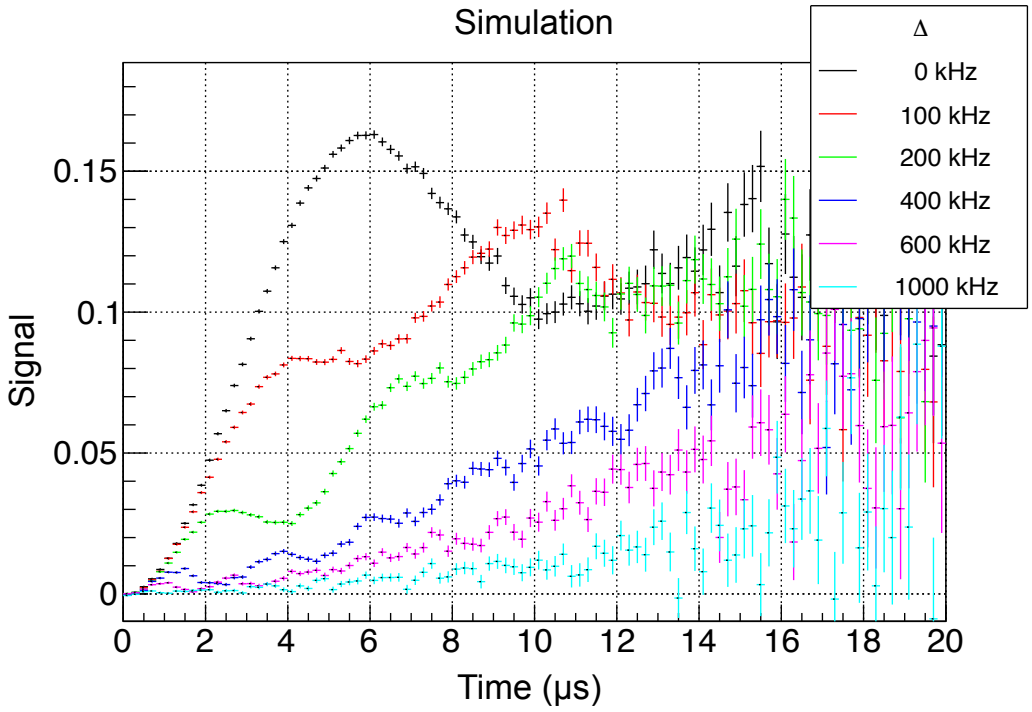


Figure 4.5: The simulation results of the time differential signal.

The fitting function is expressed as

$$f_{\mathrm{diff}}(t,\ p_1,\ p_2,\ \Delta,\ \lambda,\ t_0) = p_1 \frac{\frac{aP}{2}\sum_i N_i \left(\frac{G_+}{\Gamma}\cos G_-(t-t_0) + \frac{G_-}{\Gamma}\cos G_+(t-t_0) - 1\right) S_i}{\sum_i N_i \left(1 + \frac{aP}{2} S_i\right)}, \tag{4.2}$$

where $p_1$ is the signal amplitude scaling factor, $p_2$ is the power scaling factor, $\Delta$ is the difference between the microwave frequency and the muonium HFS frequency, $\lambda$ is the spin relaxation rate, and $t_0$ is the time when muonium is formed. These five values are free fitting parameters. $N_i$ and $S_i$ are the number of stopping muons and the solid angle of the silicon strip detector, respectively. $G_\pm$ is expressed as

$$G_\pm = \frac{\Gamma \pm 2\pi\Delta}{2}, \tag{4.3}$$

$$\Gamma = \sqrt{(2\pi\Delta)^2 + 8\,|p_2 b|^2}. \tag{4.4}$$

We developed a new method to obtain the muonium HFS frequency from multiple

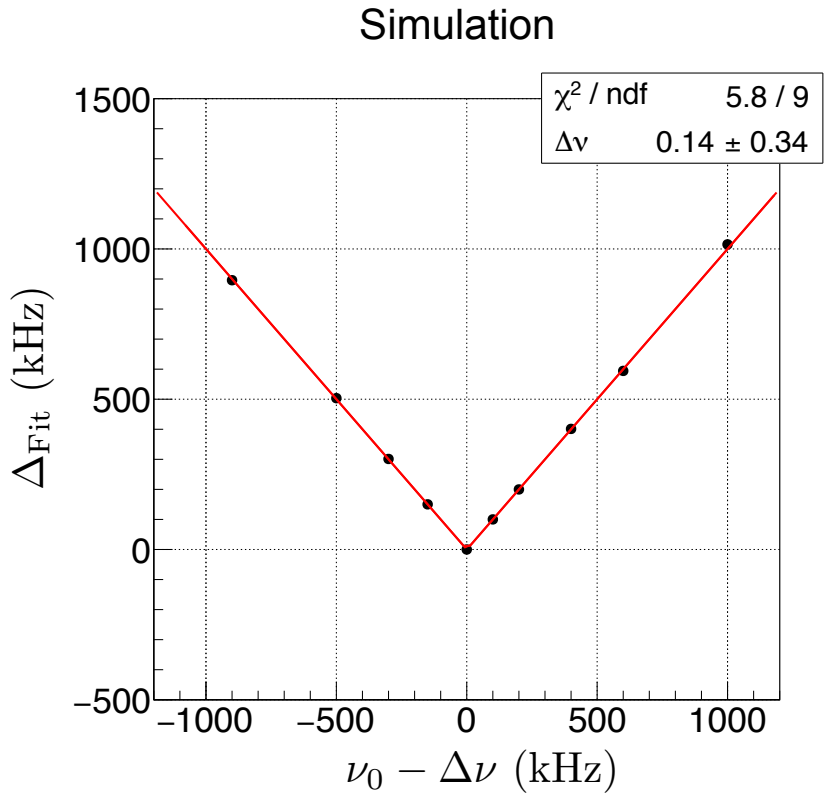


Figure 4.6: The simulation result of the multiple time differential method.

results of the time differential method. The muonium HFS frequency $\Delta\nu$ is described with the following equation,

$$\Delta\nu = \nu_0 - \Delta, \tag{4.5}$$

where $\nu_0$ is the microwave frequency, and $\Delta$ is the detuning frequency obtained by fitting. However, only absolute value of the detuning frequency from the muonium HFS frequency, $|\Delta|$, can be obtained in the time differential method. Thus, the muonium HFS frequency is

$$|\Delta| = |\nu_0 - \Delta\nu| \tag{4.6}$$

Figure 4.6 shows the simulation results of the multiple time differential method. Eq. 4.6 was used as fitting function. Precision of the muonium HFS frequency by the time differential method was estimated to be 0.34 kHz.

This result is just a particular case when the same data as the time integral method

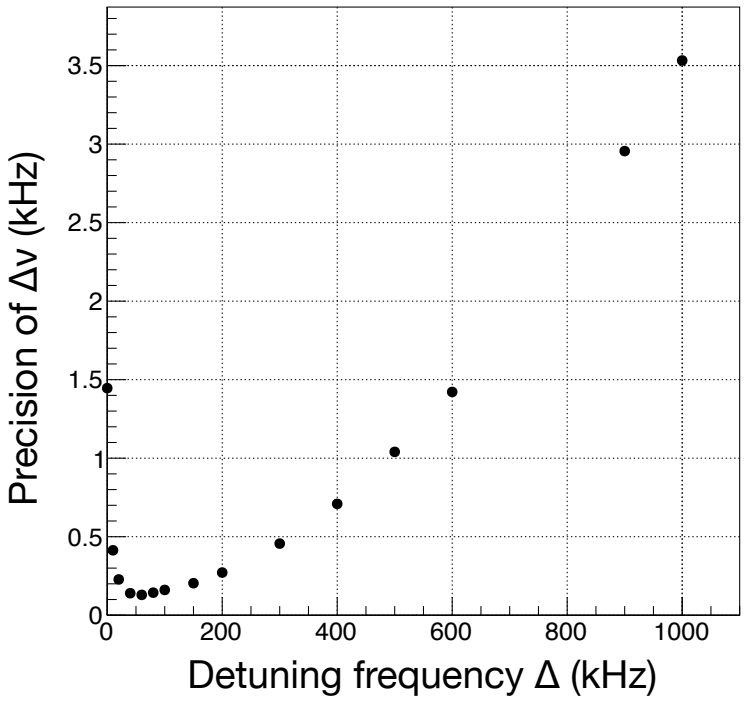


Figure 4.7: Relation between the detuning frequency and the precision of the obtained muonium HFS frequency when a quality factor of 20000 and an injected microwave power of 0.8 W are considered. The most precise point is when the detuning frequency is set to 60 kHz.

are used. One of the most charming point of the time differential method is that the muonium HFS frequency can be determined by only one frequency data. Figure 4.7 shows the relation between the detuning frequency and the precision of obtained muonium HFS frequency by a simulation whose statistics for each point is the same as the total statistics of the above simulations. This plot indicates that the most precise data can be obtained when the detuning frequency is set to 60 kHz. Figure 4.8 shows the time differential signal obtained by a simulation when the detuning frequency is set to 60 kHz, and the precision of the obtained muonium HFS frequency was estimated to be 0.13 kHz. This precision is 3.2 times better than that obtained by the time integral method.

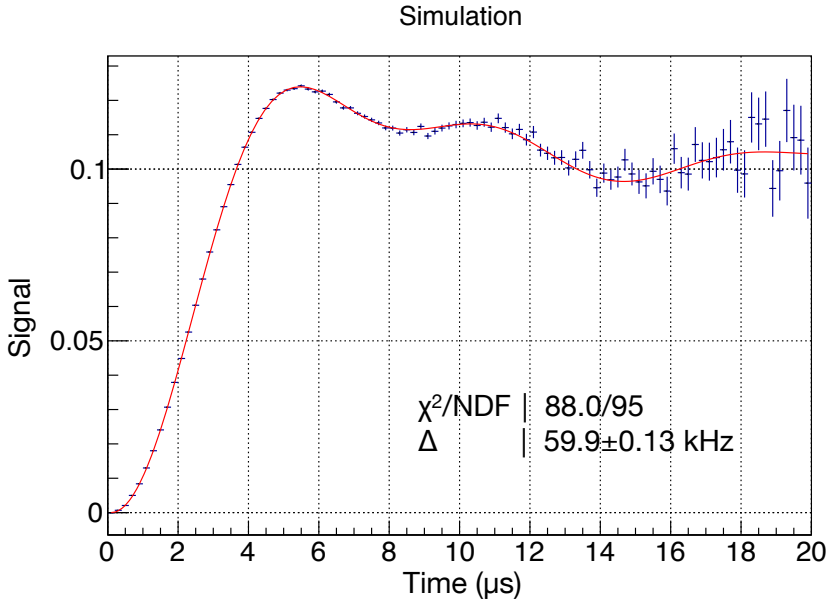


Figure 4.8: The simulation result of the time differential signal when the detuning frequency is set to 60 kHz. The red line indicates the fitting result.

## 4.4 Comparison of the Time Integral Method and the Time Differential Method

By comparing with the precision of the time integral method, the precision of the time differential method is 15% better when the same data set is used. Moreover, the time differential method can determine the muonium HFS with only one detuning frequency data. Accordingly, the time differential method can be used efficiently by concentrating all data at the most sensitive detuning frequency, and the statistical uncertainty would be drastically improved by 3.2 times compared to the time integral method.

In addition, the microwave power can be obtained by the fitting of the time differential signal. Therefore, it is possible that the systematic effect of the variation of the microwave power can be eliminated by using the time differential method. Consequently, the time differential method can improve both the systematic uncertainty and the statistical error.

# Chapter 5

# Experimental Data Analysis

The experiment of the muonium HFS measurement was conducted from June 13 to June 19, 2017. This chapter presents the experimental data analysis of the silicon strip detector and the resonance spectroscopy. First, the validation of the silicon strip detector is described. Next, the stability check of the detector and the stored energy in the cavity are described. Then, the analysis of the time differential method is discussed.

## 5.1 Experimental Setup

The experiment was conducted at area D2 of J-PARC MLF MUSE. The measurement period of the beam time was 30 hours for beam tuning and 100 hours for the muonium HFS measurement. The experimental apparatus is described in Ch. 3.

## 5.2 Validation of the Silicon Strip Detector

Event loss or multi-count deforms the signal shape. This deformation may contribute to the systematic uncertainty. Thus, validation of the detector is necessary. First, strips of the silicon detector were qualified by the time over threshold (ToT) distribution to mask noisy strips. Next, events with the same timing between adjacent strips were merged to prevent multi-count. Then, the event loss was estimated by the time distribution of clusters.

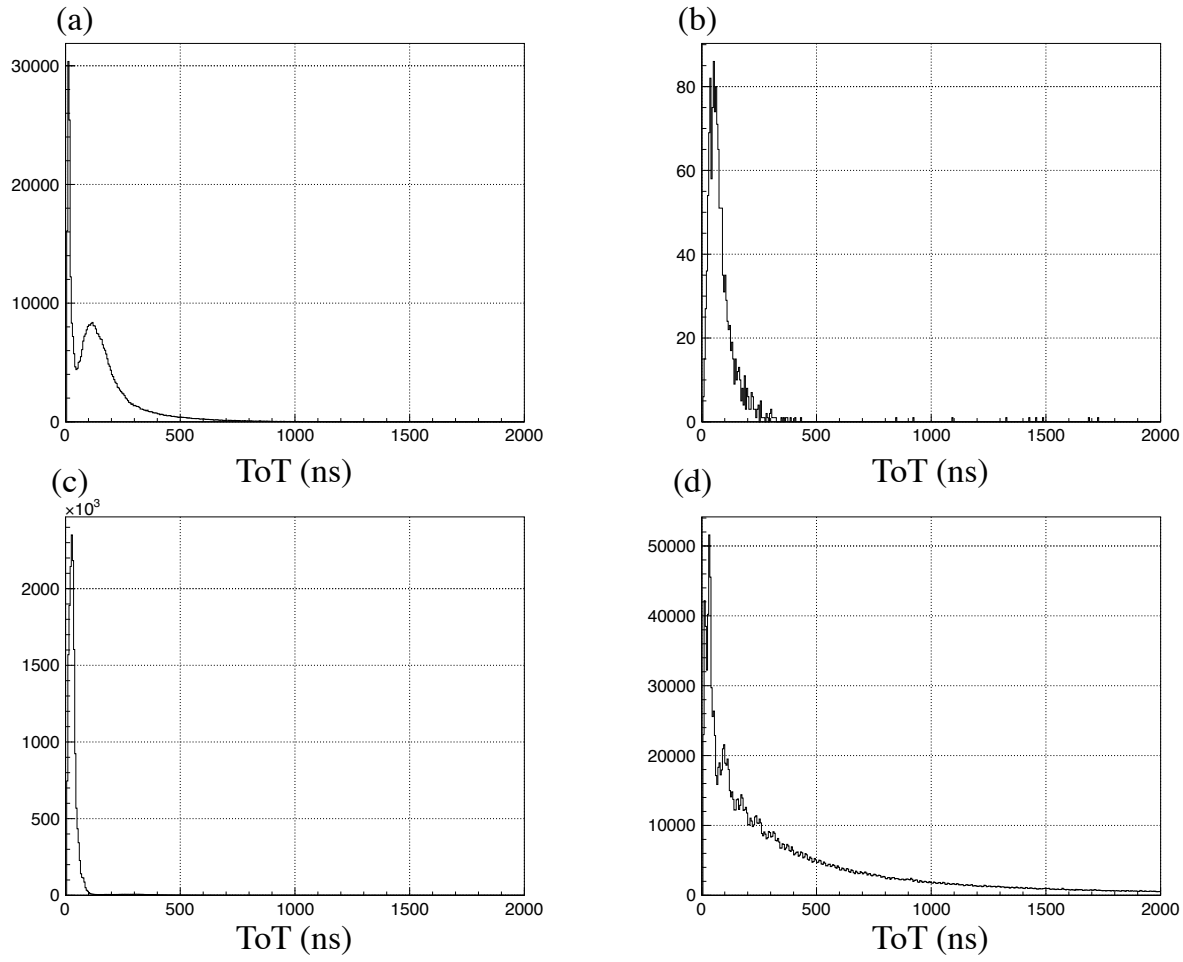


Figure 5.1: Representative plots of ToT distribution. (a) Threshold was reasonable. Noise and MIP signals were clearly separated. (b) Threshold was high, and the total number of counts was small. (c) Threshold was low, and ToT cut was necessary to obtain the number of signals. (d) Noise level was too high to distinguish signals from the noise. These strips were masked in the following analysis.

### 5.2.1 Qualification of Strips

The SliT128A measured both the leading edge and trailing edge of signal pulses. The ToT was calculated from the time difference between these edges. The ToT gave us information on the charge distribution that depends on the noise level, signal height, and pulse width. Therefore, we could evaluate the strips. Strips were classified into four types by ToT spectra. Several typical ToT distributions are shown in Fig. 5.1, and the number of strips and strip types are summarized in Table 5.1. In total, 89% strips survived.

Table 5.1: Strip types and the number of strips.

| Threshold level | Number of strips |
|---|---|
| High threshold level | 20 |
| Reasonable | 714 |
| Low threshold level | 174 |
| Too noisy | 10 |
| Dead | 106 |
| Total (alive / masked) | 908 / 116 |

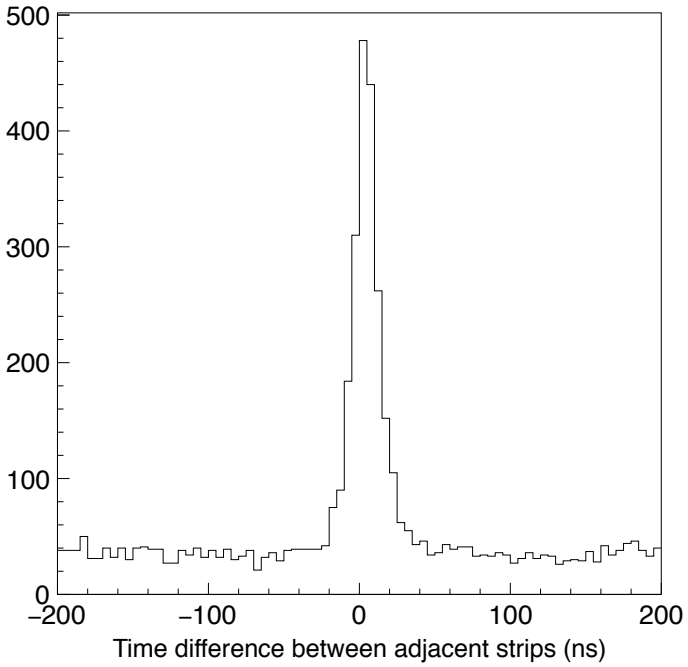


Figure 5.2: Time difference between adjacent strips. A peak due to multi-hits appears on the accidental coincidence floor.

### 5.2.2 Clustering

When a positron hits multi-strips, it is necessary to merge several hits to avoid double counting. Figure 5.2 represents the distribution of the time difference between adjacent strips for all events. As the plot indicates, there is a multi-hit peak with a time width of ±20 ns on the floor due to accidental coincidence. Thus, multi-events within ±20 ns on adjacent strips were merged.

### 5.2.3 Time Distribution

Figure 5.3 shows the time distribution of the clustered events normalized by the number of pulses. The first peak corresponds to the prompt electron beam generated at the muon production target. The muon beam arrives at the Kr gas target 250 ns after the prompt electron beam.

As a fitting result, we obtain a muon life time of 2198±1.6 ns. It is consistent with previous measurements. The number of positrons hitting the whole sensor is estimated to be 430 counts/pulse, which is consistent with the simulation result. Namely, the maximum hit rate of decay positron is estimated to be about 0.2 MHz per strip. Assuming a muon pulse width of 100 ns, the maximum event loss ratio due to pile-up is estimated to be 0.02%. However, this result indicates that 14% of decay positrons are lost at the beginning. This is caused by strips having a wide pulse width. Typical distorted and non-distorted time distributions are shown in Fig. 5.4.

The effect of event loss for systematic uncertainty will be discussed in Ch. 6. This problem could be solved by improving the board power supply to control better the chips.

## 5.3 Stability of the Counting Rate and the Microwave Power

Fluctuation of the beam power or the ground level of the detector could change the counting rate and the signal shape. Fluctuation of the microwave power could also distort the signal shape. For these reasons, it is important to validate the stability of the counting rate and the microwave power.

For the validation, it is useful to compare two data with the same microwave condition. If there is no fluctuation, the signal should be zero constant as shown in Fig. 5.5.

Figure 5.6 shows the chi-square distribution when we assume the signal to be zero constant. The data with a chi-square of more than 149, corresponding to 0.1 percent probability equivalent, are discarded in the following analysis.

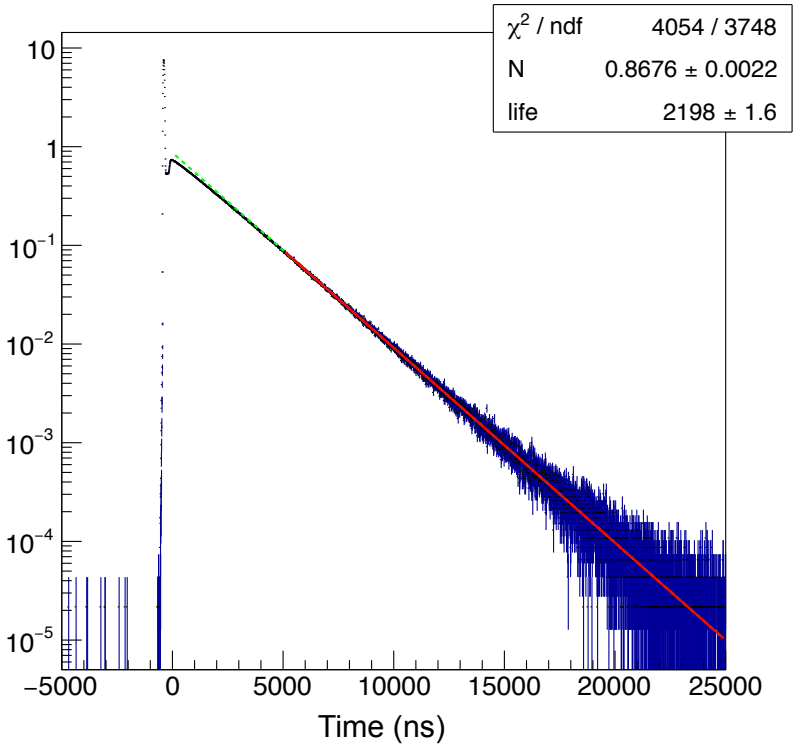


Figure 5.3: Time spectrum of the silicon strip detector scaled by the number of pulses with the microwave power off. The time zero was adjusted to the time when the muon beam is injected to the Kr gas target. The red line shows the fitting result with an exponential function from 5 $\mu$s. Extrapolation of the fitting result to the time zero is represented with a green broken line.

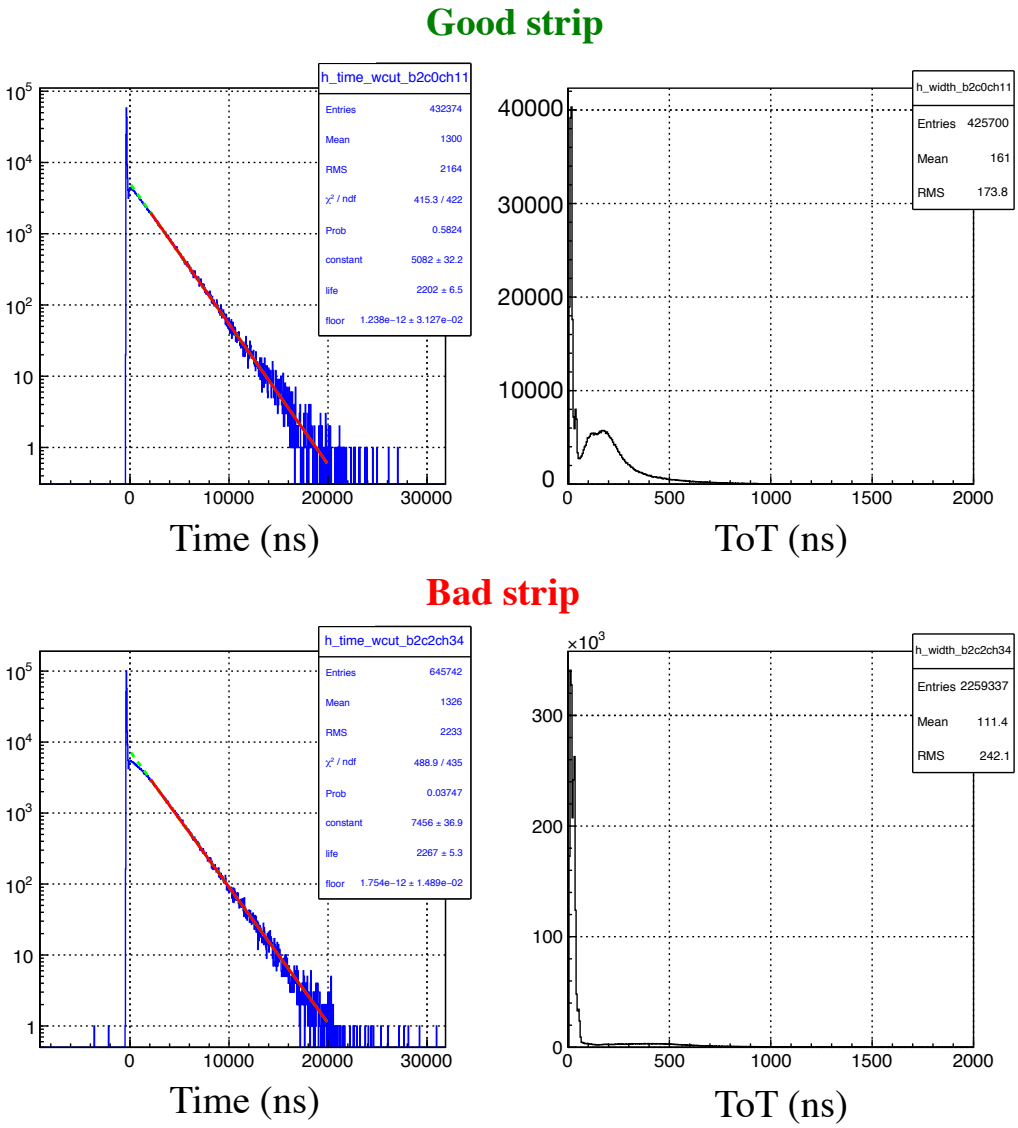


Figure 5.4: Typical time spectra (left) and ToT distributions (right) before clustering. The top shows the data of a well controlled strip and event loss cannot observed. However, there is more than 20% of event loss in the bottom plots. The pulse width estimated from the ToT distribution is much wider than expected.

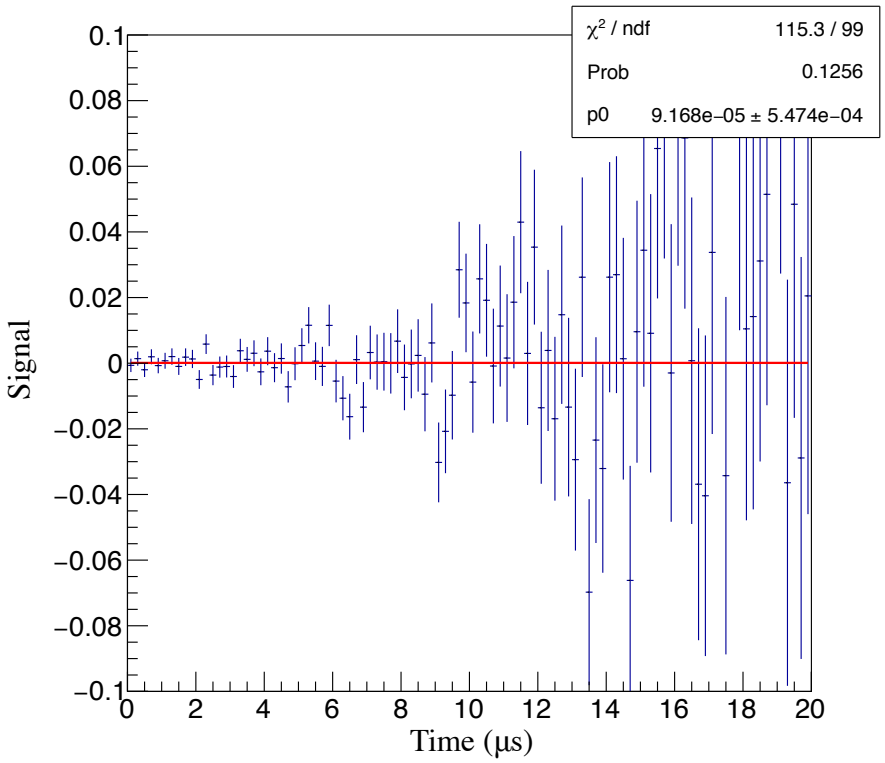


Figure 5.5: The ratio of two data with the microwave power off. The red line indicates the fitting result with a constant function. This result shows that there was no fluctuation of the counting rate between the two data.

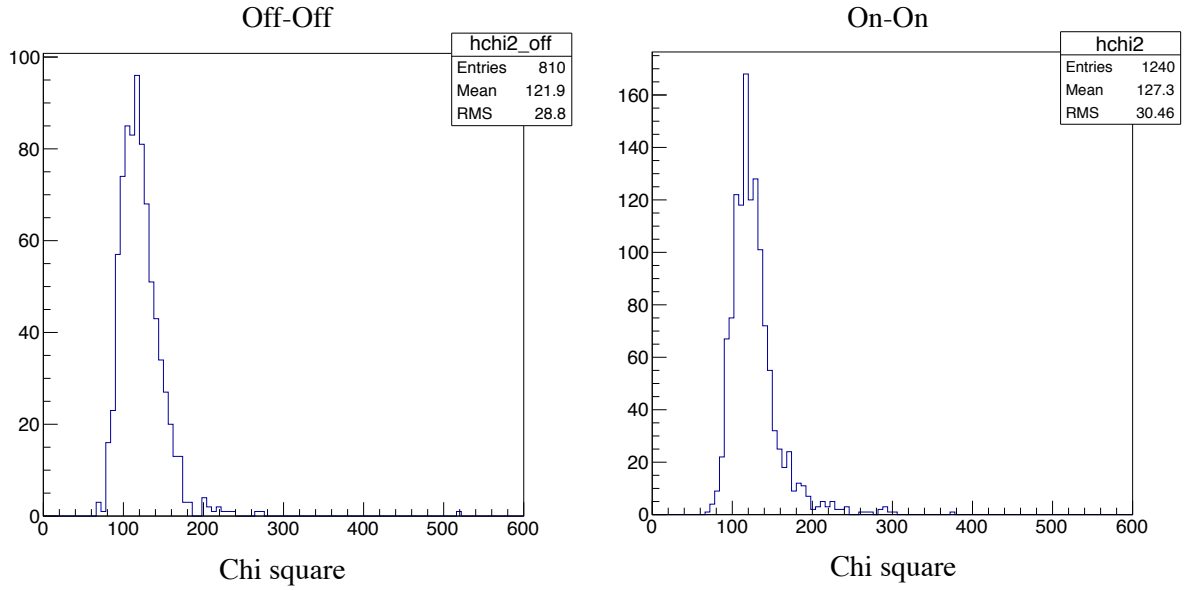


Figure 5.6: Chi-square distribution when assuming fitting results of zero constant signals. The left side shows data with microwave power off, and the right side data with microwave power on.

## 5.4 Analysis of Time Differential Signal

Figure 5.7 shows typical time differential signals. The time bin width is 100 ns before 10 $\mu$s, and rebined to 500 ns after 10 $\mu$s to reduce statistical uncertainty. For the fitting, Eq. 2.61 and the minimum chi-square method was applied. The minimization was carried out with the MIGRAD algorithm from MINUIT fitting software, and then the MINOS algorithm was used to evaluate uncertainties of the parameter values [45]. The microwave power distribution and the muon stopping distribution were assumed to be the same as in the simulation results discussed in Sec. 4.3. There are two types of parameters. One is common parameters to all measurements. The signal amplitude factor, the time offset, and the spin relaxation coefficient are of this type. The other is individual parameters to each measurement. The scale factor of the microwave power amplitude and the detuning frequency from the muonium HFS frequency are of this type. In total, we measured muonium HFS frequency at 44 detuning frequency points.

## 5.5 Analysis of Multiple Time Differential Method

The experimental data analysis is different from the simulation since we must consider the gas density shift.

From Eq. 4.5 and Eq. 4.6, we obtain

$$\Delta\nu_{\mathrm{HFS}}\left(0\right)\left(1+aD+bD^{2}\right)=\nu_{0}-\Delta, \tag{5.1}$$

or

$$\left|\Delta'\right| \;=\; \left|\nu_{0}'-\Delta\nu_{\mathrm{HFS}}\left(0\right)\right|, \tag{5.2}$$

where

$$\Delta'=\frac{1}{1+aD+bD^{2}}\Delta, \tag{5.3}$$

$$\nu_{0}'=\frac{1}{1+aD+bD^{2}}\nu_{0}, \tag{5.4}$$

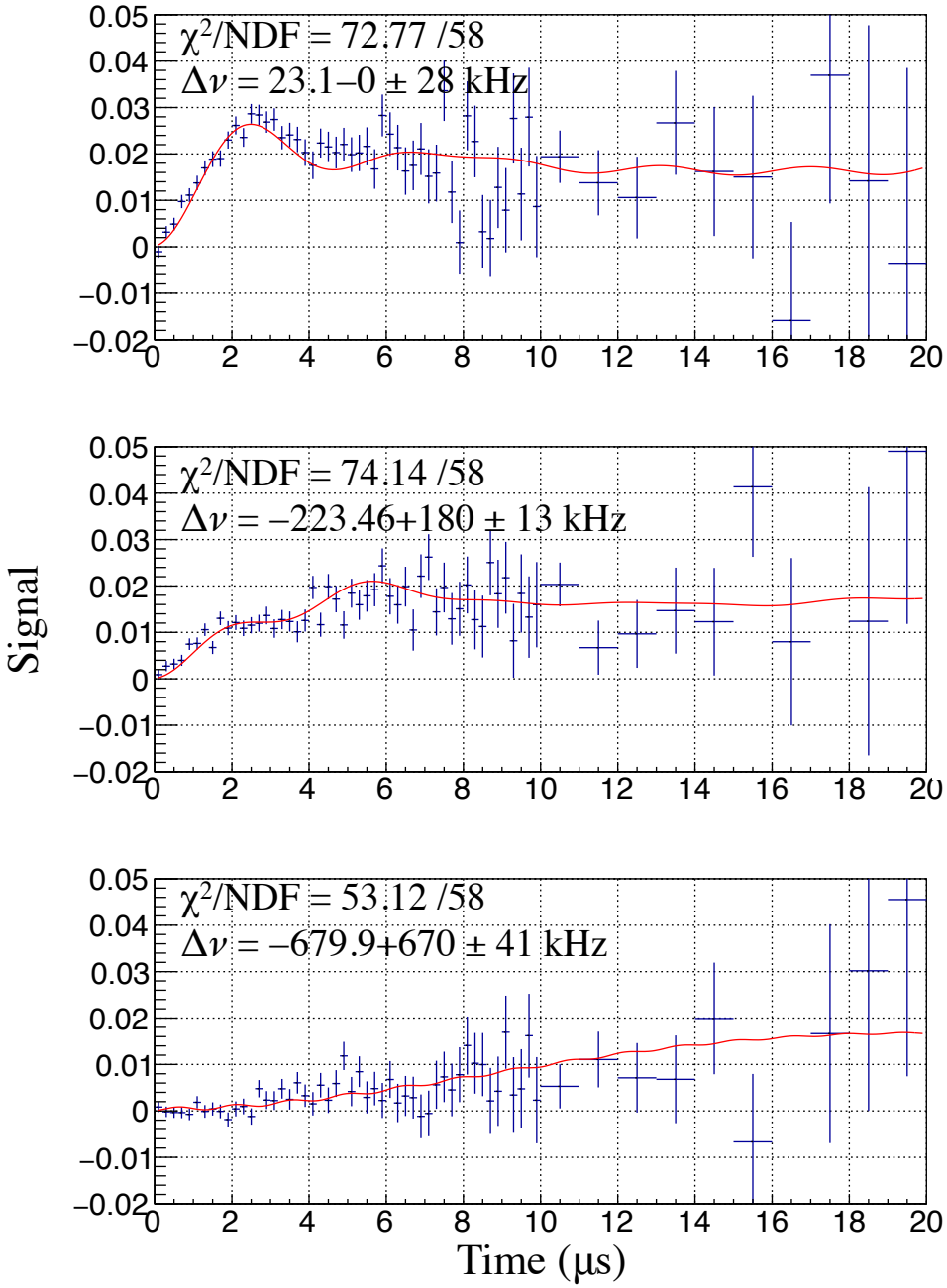


Figure 5.7: Typical time differential signals. The frequency of the signal generator was from the top, +23.10 kHz, −223.46 kHz, and −679.90 kHz from 4 463 302 kHz, respectively. The red line represents the fitting results. Equation 4.2 was used as the fitting function. The numbers, which are components of the muonium HFS, $\Delta\nu$, represent from left to right the microwave frequencies, the detuning frequencies from the fitting $\Delta'$, and uncertainties obtained by fitting for each plot.

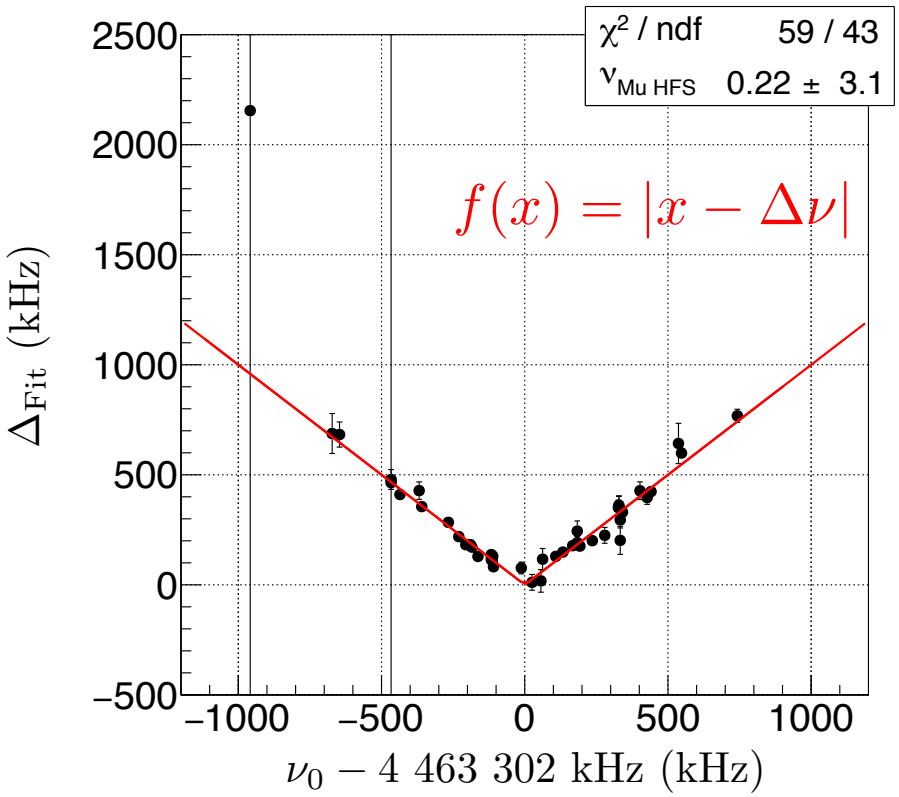


Figure 5.8: Results of the multiple time differential method. The red line shows the fitting result.

and $\Delta\nu_{\mathrm{HFS}}\,(0)$ is the muonium HFS frequency in vacuum.

Figure 5.8 shows a plot with the obtained detuning frequency from the muonium HFS frequency by fitting as the vertical axis and the microwave frequency as the horizontal axis. The pull distribution is shown in Fig. 5.9, and it indicates that the fitting is good.

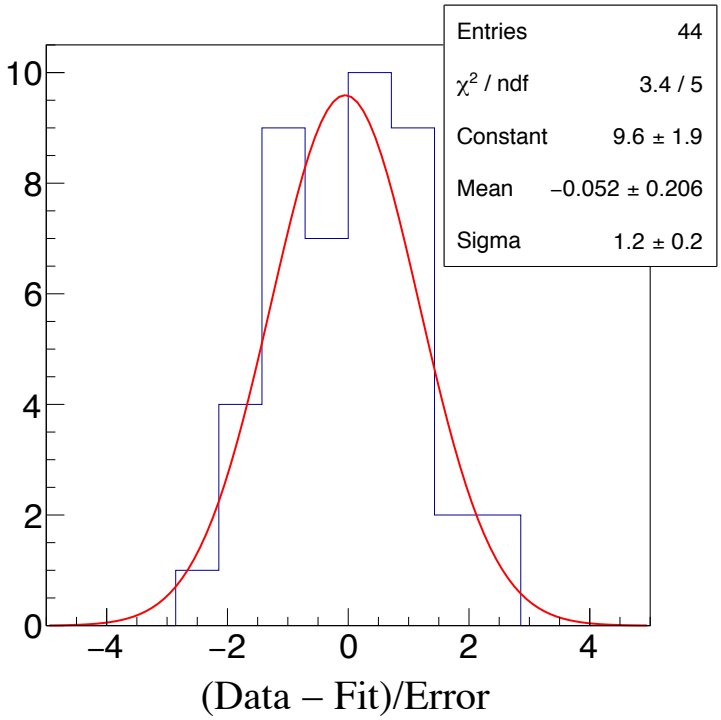


Figure 5.9: Pull distribution of the time differential method analysis. The red line represents the fitting result with a Gaussian function.

# Chapter 6

# Results and Discussion

In this chapter, we discuss about systematic uncertainties, and the result of the muonium HFS measurement in June 2017. Finally, we present some perspectives for our experiment.

## 6.1 Systematic Uncertainties of the Previous Measurement at J-PARC in 2016

Systematic uncertainty in the previous measurement at J-PARC in June 2016, were estimated and reported by Kanda [46] as shown in Table 6.1. The muonium HFS was extracted by the time integral method at that time.

Table 6.1: Systematic uncertainties of the muonium HFS measurement at J-PARC in 2016, in which the time integral method was used.

| Item | Contribution |
|---|---|
| Gas pressure extrapolation | 66 Hz |
| Gas pressure fluctuation | 6 Hz |
| Gas impurity | 12 Hz |
| Static magnetic field | 0 Hz |
| Muon beam profile | 9.8 Hz |
| Detector pileup | 2 Hz |
| Microwave power drift | 26 Hz |

## 6.2 Systematic Uncertainties in 2017

The differences between the experiments in 2016 and 2017 are the analysis method, detectors, and the microwave cavity. Therefore, it is necessary to estimate other uncertainties arising from these differences.

For the time differential method, the signal shape is directly fitted, so unexpected distortion of the signal becomes the main source of systematic. To put it the other way around, understanding the signal deformation can reduce systematic uncertainties by adding the effect to the fitting function.

Candidates of signal distortion not considered in the fitting were the event loss due to pileup, the wrong assumption of the muon beam profile, the microwave power distribution, and the uncertainty of the time calibration of the detector. Uncertainties due to these effects are discussed later. In addition to these effects, the uncertainty in June 2017 due to gas pressure fluctuation was also estimated.

### 6.2.1 Gas Density

As discussed in Sec. 3.4, the resonance frequency is shifted due to collisions between the Kr gas and the muonium atom. The quantity of the frequency shift is experimentally described in Eq. 3.3. There was a pressure fluctuation of about 20 Pa as shown in Fig. 3.10 and its contribution to the uncertainty was estimated to be 7 Hz. This value was larger than in the previous experiment in 2016 because the set temperature of the chiller was colder and a time variation of the gas pressure was observed.

Furthermore, according to the data sheet, the accuracy of the capacitance gauge, which becomes uncertainty due to extrapolation to zero gas density, was 0.2%. The systematic uncertainty due to the accuracy of the capacitance gauge was estimated to be 66 Hz. It was the same value as in the previous experiment.

### 6.2.2 Muonium Spin Depolarization

As discussed in Ch.3, gas impurity is the cause of depolarizing collisions and chemical reactions and makes spin relaxation rate higher. The spin relaxation due to

gas impurity was included in the fitting function and no effect was observed.

The initial depolarization of the muon, the wrong evaluation of the momentum distribution of detected positron, and detecting decay positrons of muons which decay in the wall of the cavity only lead to changes in the signal amplitude and was considered in the fitting function. Therefore, systematic uncertainties due to the muon spin depolarization were estimated to be nearly zero.

### 6.2.3 Wrong Assumption of the Microwave Power Distribution

The wrong assumption of the distribution of the microwave power felt by muonium leads to signal shape distortion and becomes a source of systematic uncertainty. The cause of a misassumption is mainly the microwave power drift and the application of the wrong muon stopping distribution. As shown in Fig. 3.19, the microwave power decreased by up to 50% during the measurements.

The difference of the microwave power distribution felt by muonium due to a wrong assumption is shown in Fig. 6.1 for several situations. This figure indicates that a microwave power drop was dominant to change the distribution. Therefore, it is sufficient to evaluate the uncertainty due to a microwave power drop as the uncertainty of the wrong assumption of the microwave power distribution.

The equation of the time differential signal of muonium which feels the microwave with power $|b|$ can be modified from Eq. 2.61 as,

$$\begin{aligned} dS_{\mathrm{diff}} &= K\left(\frac{1+\frac{\Delta\omega}{\sqrt{\Delta\omega^2+8|b|^2}}}{2}\cos\left(\frac{\sqrt{\Delta\omega^2+8|b|^2}-\Delta\omega}{2}t\right)\right. \\ &\quad \left.+\frac{1-\frac{\Delta\omega}{\sqrt{\Delta\omega^2+8|b|^2}}}{2}\cos\left(\frac{\sqrt{\Delta\omega^2+8|b|^2}+\Delta\omega}{2}t\right)-1\right) \\ &= K\left(\frac{1}{\sqrt{1+\frac{8|b|^2}{\Delta\omega^2}}}\left(\frac{\sqrt{1+\frac{8|b|^2}{\Delta\omega^2}}+1}{2}\cos\left(\frac{\sqrt{1+\frac{8|b|^2}{\Delta\omega^2}}-1}{2}\Delta\omega t\right)\right.\right. \\ &\quad \left.\left.+\frac{\sqrt{1+\frac{8|b|^2}{\Delta\omega^2}}-1}{2}\cos\left(\frac{\sqrt{1+\frac{8|b|^2}{\Delta\omega^2}}+1}{2}\Delta\omega t\right)\right)-1\right), \end{aligned} \tag{6.1}$$

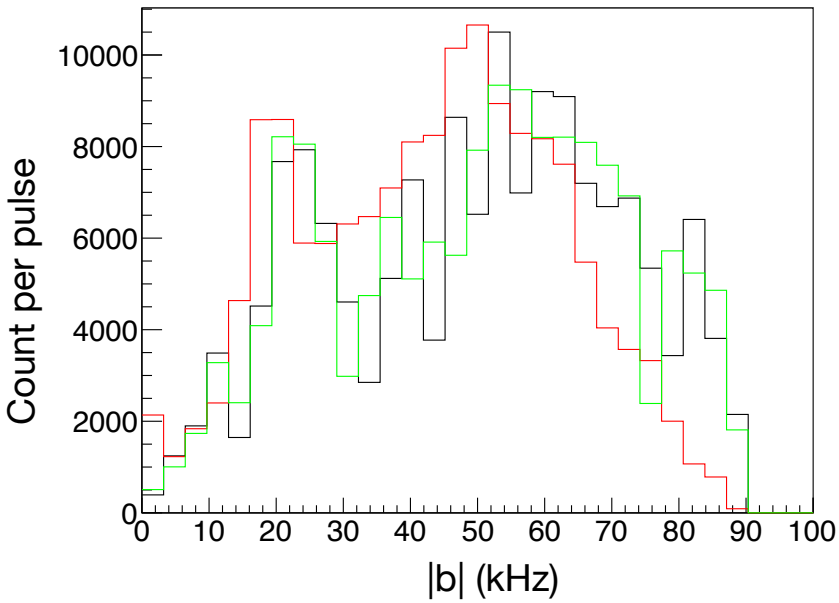


Figure 6.1: Microwave power distributions felt by muonium estimated by a simulation. The black line shows the ideal distribution of the microwave power. The green line indicates the microwave power distribution when the beam center was assumed to be shifted by 10 mm. The red line shows the distribution when the microwave power was assumed to constantly drop to 50% during the measurement. These distributions were normalized by the number of muons in a pulse at 150-kW proton beam power. In this experiment, the largest misassumption of the microwave power distribution was due to the microwave power drop.

where $K$ is a time independent signal amplitude when the spin relaxation rate is negligibly small and expressed as

$$K = \frac{\frac{aP}{2}\cos\theta}{1 + \frac{aP}{2}\cos\theta}. \tag{6.2}$$

The equation 6.1 indicates that the angular detuning frequency, $\Delta\omega$, is dominant in frequency of the cosine function when the microwave power, $|b|$, is larger than $\Delta\omega$. To put it the other way round, a lower detuning frequency is more strongly related to the microwave power. Figure 6.2 shows a plot obtained by a simulation with the ratio of the microwave power drop as the horizontal axis and the precision of muonium HFS for each detuning frequency as the vertical axis. This plot indicates that the obtained muonium HFS frequency is shifted by more than 5 kHz due to a microwave power drop of 50% when the detuning frequency is set to 10 kHz. However, no significant shift of more than 200 Hz is observed when the microwave power decreases by 10% under a detuning frequency of 100 kHz, or even if the microwave power drops by 50% over a detuning frequency of 100 kHz. In this experiment, the microwave power decreased up to 10% during the measurement with a detuning frequency was set to under 100 kHz. Hence, the uncertainty due to a microwave power drop was estimated to be up to 200 Hz.

### 6.2.4 Pileup Event Loss

In the experiment in 2017, the event loss of the silicon strip detector due to pileup was estimated to be 14% at maximum from the time spectrum. By the way, when we will use the MLF H-Line instead of the D-Line and the proton beam power increases to 1 MW, the counting rate of the silicon strip detector will be 29 count/strip and the event loss will be expected to be 36% at maximum. Hence, the systematic uncertainty arising from event loss in this experiment was smaller than that of in the future. The uncertainty due to the pileup event loss in future measurements was estimated.

Figure 6.3 shows a plot with the detuning frequency as the horizontal axis and the precision of the obtained muonium HFS frequency as the vertical axis. For each detuning frequency, the statistics is the same, so the detuning frequency dependence

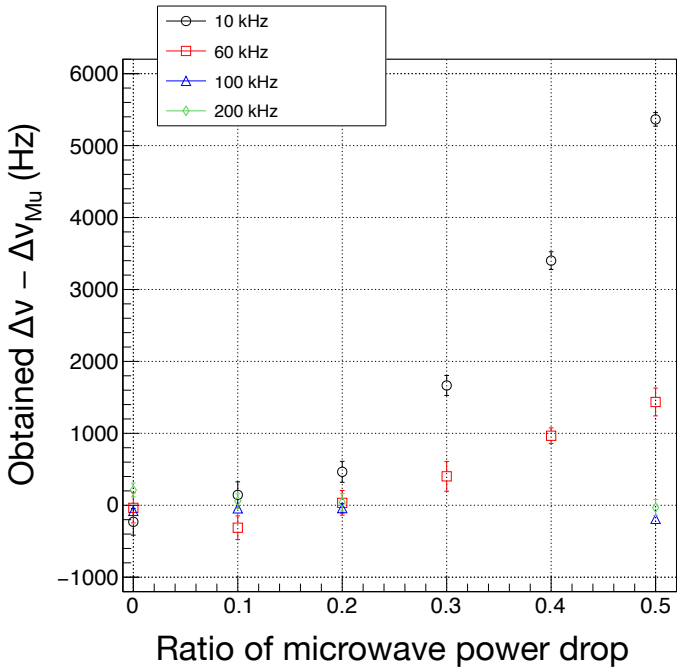


Figure 6.2: Relation between the ratio of the microwave power drop and the precision of muonium HFS frequency for several frequencies obtained by a simulation.

appears to the error bar in this plot as discussed in Ch. 4.3.

As a result, no significant shift of the muonium HFS frequency was observed and the systematic uncertainty due to pileup event loss was estimated to be 10 Hz in this experiment. If the measurement is concentrated to the detuning frequency of 60 kHz in the future, the systematic uncertainty would be 1 Hz.

### 6.2.5 Uncertainty due to the Time Calibration

Equation 6.1 can be re-written as follows,

$$dS_{\mathrm{diff}} = K\left(\frac{1}{\sqrt{1+\frac{8|b|^2}{\Delta\omega^2}}}\left(A_+\cos\left(A_-\Delta\omega t\right)+A_-\cos\left(A_+\Delta\omega t\right)\right)-1\right), \tag{6.3}$$

where $A_\pm = \frac{\sqrt{1+8|b|^2/\Delta\omega^2}\pm 1}{2}$, respectively. If $\Delta\omega$ is changed, $A_\pm$ could stay constant by optimizing $|b|$ and $K$. Thus, this equation implies that the time spectrum of the signal can be scaled in the time direction by shifting $\Delta\omega$, $|b|$, and $K$, which are free parameters in the fitting function. Therefore, the uncertainty of the time

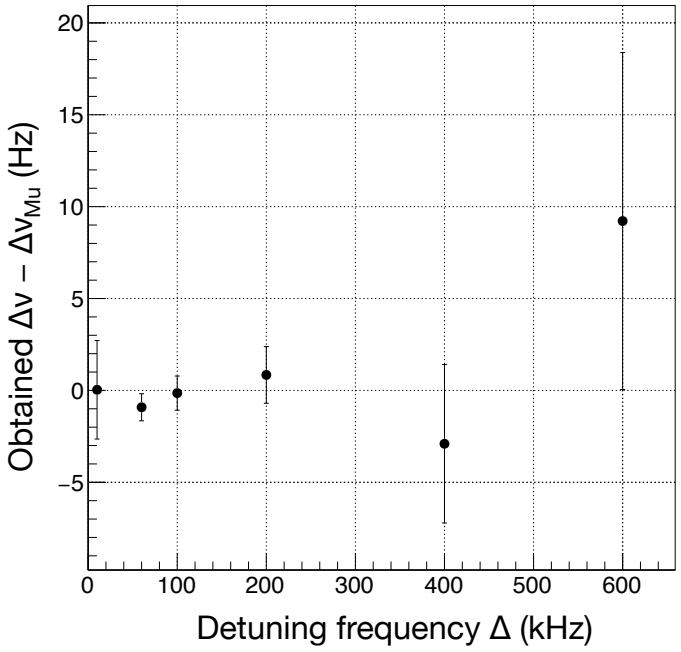


Figure 6.3: Result of the event loss simulation plotted with the detuning frequency as the horizontal axis and the muonium HFS frequency as the vertical axis. There is no significant shift for any detuning frequencies.

calibration would directly be the systematic uncertainty, and its quantity depends on the detuning frequency. For example, when the accuracy of the time calibration is 1% at 100 kHz detuning frequency, the systematic uncertainty of the muonium HFS frequency would be 1 kHz. In this experiment, the detuning frequency was set to less than 1 MHz and the accuracy of the time calibration, which was determined by the accuracy of the frequency of pulse generator, was 1 ppm. Hence, the systematic uncertainty due to the time calibration was estimated to be 1 Hz.

## 6.3 Results and Perspectives

### 6.3.1 Results of the Experiment at J-PARC in June 2017

As given in the above discussion, the total systematic uncertainty was evaluated to be 200 Hz in this experiment. The result of our muonium HFS measurement in June

2017 was

$$\Delta\nu_{\mathrm{Mu}} = 4\,463\,302.2 \pm 3.1 \pm 0.2\ \mathrm{kHz}. \tag{6.4}$$

where the first error is the statistical uncertainty and the second one is systematic. The total uncertainty was 690 ppb. This value is consistent with the previous result at LAMPF, and it corresponds to an improvement by a factor of seven from the previous measurement at J-PARC. This improvement is caused by a time differential method, using the TM220 cavity, and removal of a beam collimator. The precision in this experiment would be improved twice compared to the previous experiment at zero field if the measurement would run for the same period of time, and by using the time differential method.

### 6.3.2 Future Perspectives

The summary tables of the statistical uncertainty and the different systematic uncertainties are indicated in Table 6.2 and Table 6.3, respectively.

In the future, the power drop could be suppressed down to 0.02% by installing a water cooling system to the microwave cavity, and also a microwave power feedback system [47]. The simulation result plotted with the detuning frequency as the horizontal axis and the precision of the muonium HFS frequency as the vertical axis is shown in Fig. 6.4. It indicates that there is no significant shift when the detuning frequency is set to more than 10 kHz. When the measurement is concentrated to a detuning frequency set to 60 kHz, the systematic uncertainty due to a power drop of 0.02% was estimated to be 1 Hz.

Finally, we could achieve 24 Hz (5 ppb) for the statistical uncertainty by using a higher proton beam power, spreading the active area of the silicon strip detector, extending the measuring time, and using the H-Line that will provide a muon beam intensity 10 times higher than that of the D-Line. The total systematic uncertainty will also be improved to 10 Hz (3 ppb). Therefore, the muonium HFS frequency at zero field could be measured with a precision of 26 Hz (6 ppb), which would be even more precise than that of the high field measurement at LAMPF.

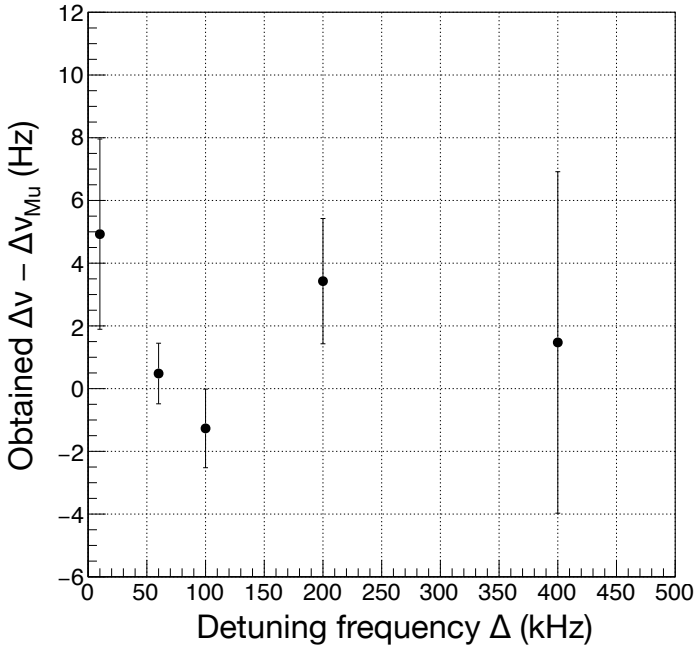


Figure 6.4: Result of a simulation to estimate the systematic uncertainty due to a power drop of 0.02%.

Table 6.2: Results in 2016, 2017, and prospects of muonium HFS frequency of the zero field experiment at J-PARC.

| | June 2016 | June 2017 | Prospects |
|---|---|---|---|
| Analysis Method | Time integral | Time differential | Time differential |
| Beam line | D Line | D Line | H Line |
| Beam power | 200 kW | 150 kW | 1 MW |
| Measurement time | 8 hours | 31 hours | 80 days (1920 hours) |
| Microwave cavity | TM110 | TM220 | TM220 |
| Detector area | 240× 240 $\mathrm{mm}^2$ | 98.77× 98.77 $\mathrm{mm}^2$ | 98.77× 98.77 $\mathrm{mm}^2$ ×4 |
| Statistical uncertainty | 22 000 Hz | 3 100 Hz | 24 Hz |

Table 6.3: Systematic uncertainty table in this experiment.

| | June 2017 | Prospects |
|---|---|---|
| Gas pressure fluctuation | 7 Hz | 7 Hz |
| Gas pressure extrapolation | 66 Hz | 7 Hz |
| Gas impurity | 0 Hz | 0 Hz |
| Static magnetic field | 0 Hz | 0 Hz |
| Microwave power drift (including muon beam profile) | 200 Hz | 1 Hz |
| Detector pileup | 10 Hz | 1 Hz |
| Time calibration | 1 Hz | 1 Hz |
| Total systematic error | 200 Hz | 10 Hz |

### 6.3.3 Idea to Extract More Information from the Time Differential Signal

The time differential signal contains information of the microwave power, so it is possible to extract the microwave power distribution felt by muonium and make the analysis more rigid. The idea of extracting the microwave power information from the time differential signal is discussed here.

Equation 2.61 can be re-written as follows,

$$\begin{aligned} S_{\text{diff}}(\nu,\ |b|,\ t) &= \frac{\frac{aP'}{2}\int N_0(r,\theta,z)\left(\int \cos\theta d\Omega\right)(C(t)-1)\,dV}{\int\int N_0(r,\theta,z)\left(1+\frac{aP'}{2}\cos\theta\right)d\Omega dV} \\ &= \int \alpha(r,\theta,z)\,C(t)\,dV + C, \end{aligned} \tag{6.5}$$

where

$$\alpha(r,\theta,z) = \frac{aP'}{2}\frac{N_0(r,\theta,z)\int \cos\theta d\Omega}{\int\int N_0(r,\theta,z)\left(1+\frac{aP'}{2}\cos\theta\right)d\Omega dV}, \tag{6.6}$$

$$C = -\frac{aP'}{2}\frac{\int N_0(r,\theta,z)\left(\int \cos\theta d\Omega\right)dV}{\int\int N_0(r,\theta,z)\left(1+\frac{aP'}{2}\cos\theta\right)d\Omega dV}. \tag{6.7}$$

Therefore, the integral of the time differential signal over the cavity becomes

$$S_{\text{diff}}(\nu,\ |b|,\ t) = \int a(\phi)\cos\phi t\ d\phi + C, \tag{6.8}$$

in which $a(\phi)$ is an appropriate factor.

Equation 6.8 indicates that a time differential analysis can be converted into the frequency spectrum by a Fourier transform.

Especially, when the microwave frequency is set precisely to the muonium HFS frequency, the equation of the time differential signal can be described as follows,

$$S_{\text{diff}}(|b|,\ t) = \int \alpha(r,\theta,z)\left(\cos\left(\sqrt{2}\,|b|\,t\right)\ -1\right)d\phi. \tag{6.9}$$

Equation 6.9 means that the time differential signal is a summation of cosines. Its frequency and amplitude depend on the microwave power and the number of

positron hits, respectively. Hence, the Fourier transform of the time differential signal may become a strong tool to validate the dependence between the muon stopping distribution and the microwave power distribution.

# Chapter 7

# Conclusion

The muonium HFS is one of the key to search for new physics beyond the SM, and more precise measurement is desired. For that purpose, the time differential spin flip resonance method was developed. This method contains much more information than the conventional method, named the time integral method, so the precision could be improved dramatically. However, this method needs high statistics, detectors with high-rate capability and good time resolution. Therefore, a silicon strip detector optimized for high-intensity pulse beam was developed. This detector was used in the experiment in June 2017.

First, the time differential method was developed by using a MC simulation. The most charming point of the time differential method is that the muonium HFS frequency can be determined by only one detuning frequency while the time integral method needs multiple detuning frequency data. Taking advantage of this property of time differential method, it is found that the time differential method can dramatically improve the statistical uncertainty by 3.2 times compared to the time integral method. Furthermore, the systematic uncertainty due to the microwave power variation with frequency can be eliminated. Thus, the time differential method can drastically improve the uncertainty compared to the time integral method.

Next, we applied the time differential method to the experimental data in June 2017. The result of the muonium HFS frequency measurement was

$$\Delta\nu_{\mathrm{Mu}} = 4\,463\,302.2 \pm 3.1 \pm 0.2\ \mathrm{kHz}. \tag{7.1}$$

where the first error is the statistical uncertainty and the second one is the systematic uncertainty. The precision of the result value was 690 ppb. This result is consistent with the previous experiment at LAMPF, and would be twice better than the previous experiment at zero field if the data were taken for the same period of time. Moreover, by upgrading the experimental apparatus, the precision in the future was estimated to reach 26 Hz (6 ppb) at zero field. This precision would be better than the precision of the previous measurement of 12 ppb at high field. Only after the time differential method is used, this can be achieved.

# Appendix A

# Formula of Bessel Function

Bessel functions are solutions to the differential equation,

$$\frac{1}{x}\frac{d}{dx}\left(x\frac{df}{dx}\right)+\left(k^2-\frac{n^2}{x^2}\right)f=0, \tag{A.1}$$

where k is a real number and n is an integer. One of the independent solution to the equation, $J_n$, is called a Bessel function of the first kind, and the following equations are useful.

$$J_{n+1}(x) = \frac{2n}{x}J_n(x)-J_{n-1}(x), \tag{A.2}$$

$$J_n'(x) = \frac{1}{2}\left(J_{n-1}-J_{n+1}\right), \tag{A.3}$$

$$\int_0^x J_n^2\left(kt\right)t\,dt = \frac{x^2}{2}\left\{J_n'^2\left(kx\right)+\left(1-\frac{n^2}{k^2x^2}\right)J_n^2\left(kx\right)\right\}. \tag{A.4}$$

Equation A.4 is called a Integral of Lommel.

# Appendix B

# Silicon Strip Sensor Qualification

The electrical characteristics of the sensor was measured by using a micro probe at Kyushu University. This measurement is important to check the sensor quality. Table B.1 shows the results of the measurement. The sensor for the experiment was chosen according to this qualification.

Table B.1: Electrical characteristics table of the silicon strip sensor.

| Item | Estimation | Measurement |
|---|---|---|
| IV measurement | N/A | plateau observed |
| Bulk capacitance | 3100 pF | 3050 pF |
| Full depletion voltage | ~80 V | ~80 V |
| Interstrip capacitance | 3.0 pF +$\alpha$ | 7.1 pF |
| Coupling capacitance | 164 pF | 167 pF |
| Polysilicon resistance | 5~15 MΩ | ~12 MΩ |

# Appendix C

# Wire Bonding of the Silicon Detector

Figure C.1 represents a picture of the automatic small wire bonder (Orthodyne Electronics 3700 plus) at Kyushu University. Figure C.2 shows a microscope view during wire bonding. The silicon strip sensor and the readout ASIC are highly integrated. Hence, fine pitch wire bonding is necessary to assemble the detector. There are two types of wire bonding processes. One is a ball bonding process in which heat is applied to melt the wire. The other is a wedge bonding process in which only ultrasonic force is used. The former can damage the sensor because of heat. Therefore, the wedge bonding process with thin aluminum wires was used for wire bonding.

There were 3660 wires for the silicon strip detector. After the wire bonding, the status of each wire was validated by visual check with a microscope as shown in Fig. C.3.

## C.1 Pull Test

There are several tests to optimize the bond parameters, which are the bond force, ultrasonic power, bond time, loop height, and so on. For the tests, first, we check wires with a microscope whether there is a crack at the bond heels and distortion of the wire, then, we perform a pull test, which is one of the break tests.

A picture of the pull tester is shown in Fig. C.4. This pull tester can be controlled precisely by an electrical moving stage. It is useful to disconnect wires touching each other. Figure C.5 shows a schematic view of the pull test. The tension applied to the


Figure C.1: Automatic wire bonder at Kyushu University.

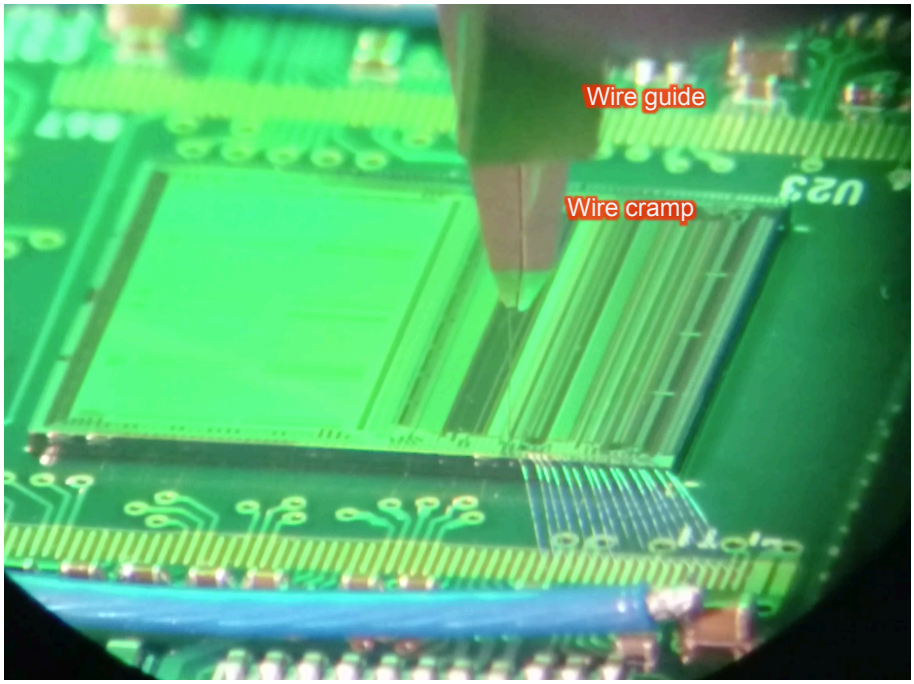


Figure C.2: Microscope view during wire bonding.

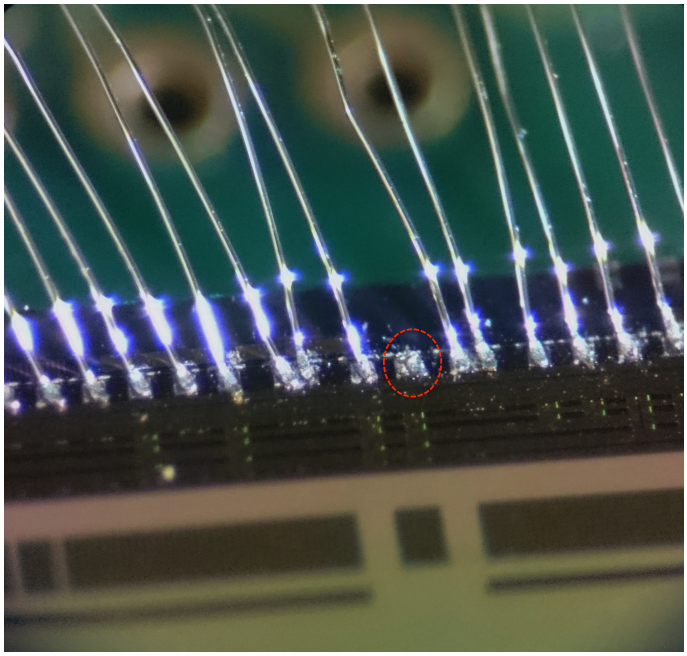

Figure C.3: Visual check of the wire bonding with a microscope. The area of bonding pads on the chip is 60 $\mu$m square. The red circle indicates a disconnected wire.

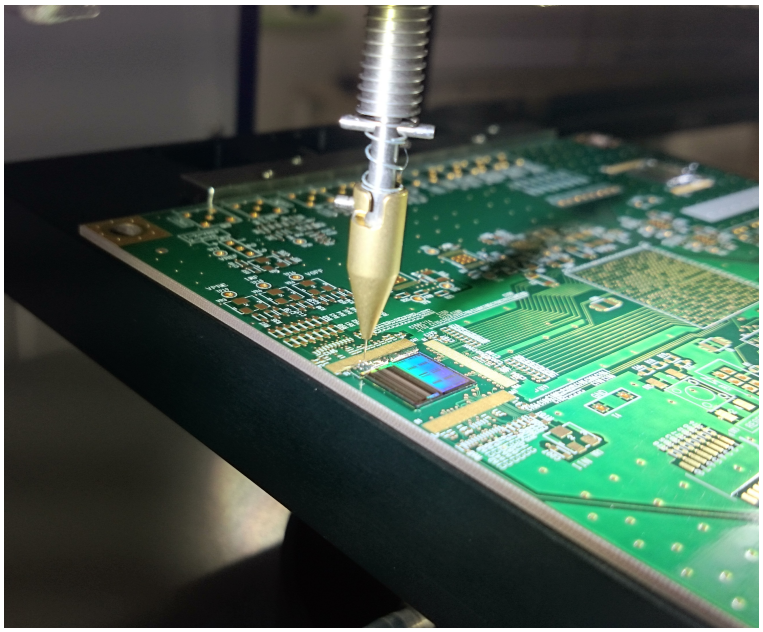

Figure C.4: Hook of the pull tester at Kyushu University. The circuit board with a chip is on the moving stage and remotely controlled.

bond heel is calculated as follows,

$$f_{\mathrm{wt}} = F\frac{\left(h^2+\epsilon^2 d^2\right)^{1/2}\left((1-\epsilon)\cos\phi+\frac{h+H}{d}\sin\phi\right)}{h+\epsilon H}, \tag{C.1}$$

$$f_{\mathrm{wd}} = F\frac{\left(1+\frac{(1-\epsilon)^2 d^2}{(h+H)^2}\right)^{1/2}(h+H)\left(\epsilon\cos\phi+\frac{h}{d}\sin\phi\right)}{h+\epsilon H}. \tag{C.2}$$

Figure C.6 shows a plot with the tension to the bonding heel as the vertical axis and the hook position as the horizontal axis for several loop heights when the wire is pulled straight up. The height difference between bonded planes, and the distance between bonds are 300 $\mu$m. This figure indicates that higher loop height gives a better result because the tension to the bond heels is smaller. In addition, this figure also shows that the pull test result depends on the pull position. Therefore, the pull position was fixed in the middle of a wire. As a result of the pull test, we obtained a pull force of more than 9 gf for a wire loop height of 400 $\mu$m.

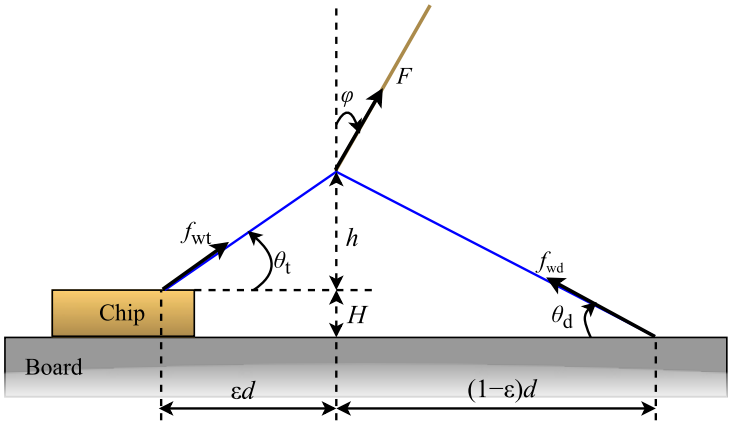


Figure C.5: Schematic view of the wire pull test.

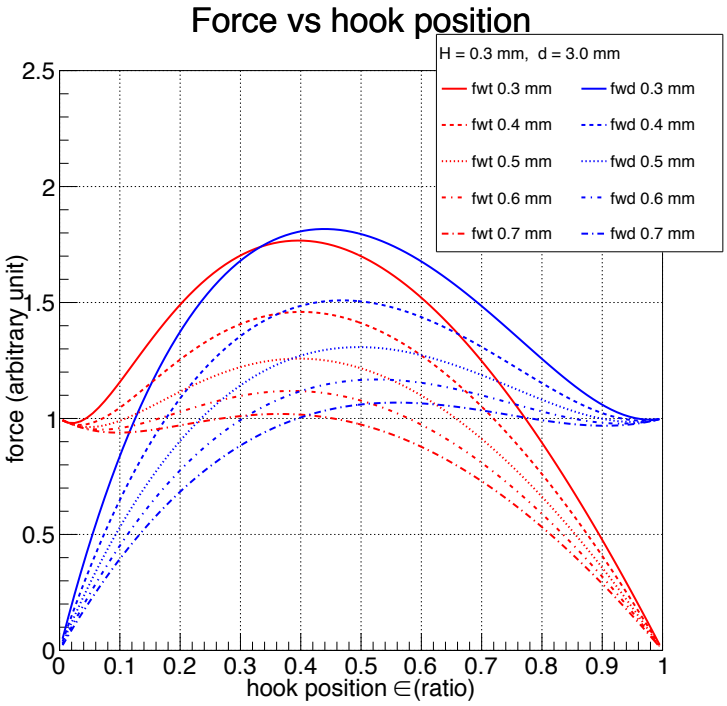


Figure C.6: Correlation plot between the pull position and the tension applied to the bond heels.

# Appendix D

# Solid Angle Calculation for an Off-axis Rectangular Detector

For a rectangular detector, which is set as shown in Fig. D.1, the solid angle is calculated as follows.

$$\Omega = \int_{\beta_1}^{\beta_2} \int_{\alpha_1}^{\alpha_2} \frac{\cos\theta \cos\phi}{\left(1 - \sin^2\theta \sin^2\phi\right)^{3/2}} d\theta d\phi \tag{D.1}$$

$$= \mathrm{Sin}^{-1}\left(\sin\alpha_1 \sin\beta_1\right) + \mathrm{Sin}^{-1}\left(\sin\alpha_2 \sin\beta_2\right) - \mathrm{Sin}^{-1}\left(\sin\alpha_1 \sin\beta_2\right) - \mathrm{Sin}^{-1}\left(\sin\alpha_2 \sin\beta_1\right). \tag{D.2}$$

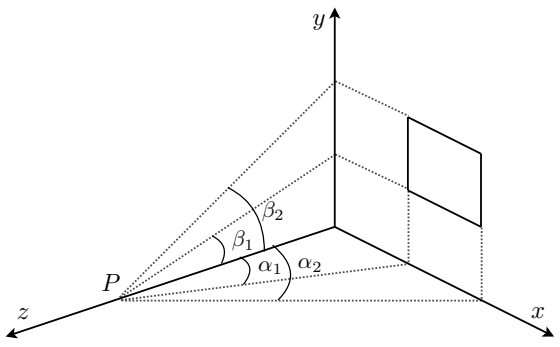


Figure D.1: Schematic view of an off-axis rectangular detector.

# References


[1] L. Essen *et al.*, Hydrogen Maser Work at the National Physical Laboratory, Metrologia **9** (1973) 128.
URL http://stacks.iop.org/0026-1394/9/i=3/a=004

[2] N. F. Ramsey, Experiments with trapped hydrogen atoms and neutrons, Hyperfine Interactions **81** (1993) 97–103.
URL https://doi.org/10.1007/BF00567253

[3] M. Diermaier *et al.*, In-beam measurement of the hydrogen hyperfine splitting and prospects for antihydrogen spectroscopy, Nature Communications **8** (2017) 15749, article.
URL http://dx.doi.org/10.1038/ncomms15749

[4] M. Eides, H. Grotch, V. Shelyuto., Theory of Light Hydrogenic Bound States, Springer Berlin Heidelberg, 2007.
URL https://doi.org/10.1007/3-540-45270-2

[5] M. W. Ritter *et al.*, Precision determination of the hyperfine-structure interval in the ground state of positronium. V, Phys. Rev. A **30** (1984) 1331–1338.
URL https://link.aps.org/doi/10.1103/PhysRevA.30.1331

[6] A. P. Mills, Line-shape effects in the measurement of the positronium hyperfine interval, Phys. Rev. A **27** (1983) 262–267.
URL https://link.aps.org/doi/10.1103/PhysRevA.27.262

[7] A. Ishida *et al.*, New precision measurement of hyperfine splitting of positronium, Physics Letters B **734** (2014) 338 – 344.

URL http://www.sciencedirect.com/science/article/pii/S0370269314003931

[8] M. Baker *et al.*, Hyperfine Splitting in Positronium to $O(\alpha^7 m_e)$: One Photon Annihilation Contribution, Phys. Rev. Lett. **112** (2014) 120407.
URL https://link.aps.org/doi/10.1103/PhysRevLett.112.120407

[9] D. Casperson *et al.*, A new high precision measurement of the muonium hyperfine structure interval $\delta\nu$, Physics Letters B **59** (1975) 397 – 400.
URL http://www.sciencedirect.com/science/article/pii/0370269375900994

[10] W. Liu *et al.*, High Precision Measurements of the Ground State Hyperfine Structure Interval of Muonium and of the Muon Magnetic Moment, Phys. Rev. Lett. **82** (1999) 711–714.
URL https://link.aps.org/doi/10.1103/PhysRevLett.82.711

[11] P. J. Mohr, D. B. Newell, B. N. Taylor, CODATA recommended values of the fundamental physical constants: 2014, Rev. Mod. Phys. **88** (2016) 035009.
URL https://link.aps.org/doi/10.1103/RevModPhys.88.035009

[12] S. G. Karshenboim, V. G. Ivanov, The $g$ factor in a light two-body atomic system: a determination of fundamental constants to test QED, Can. J. Phys. **80** (2002) 1305–1312.

[13] V. W. Hughes, G. zu Putlitz, MUONIUM, WORLD SCIENTIFIC, 2013.
URL https://www.worldscientific.com/doi/abs/10.1142/9789814503273_0016

[14] S. G. Karshenboim, Precision physics of simple atoms: QED tests, nuclear structure and fundamental constants, Physics Reports **422** (2005) 1 – 63.
URL http://www.sciencedirect.com/science/article/pii/S0370157305003637

[15] T. Kinoshita, M. Nio, Radiative corrections to the muonium hyperfine structure: The $\alpha^2(z\alpha)$ correction, Phys. Rev. D **53** (1996) 4909–4929.
URL https://link.aps.org/doi/10.1103/PhysRevD.53.4909

[16] T. Kinoshita, M. Nio, Improved theory of the muonium hyperfine structure, Phys. Rev. Lett. **72** (1994) 3803–3806.
URL https://link.aps.org/doi/10.1103/PhysRevLett.72.3803

[17] M. Nio, T. Kinoshita, Radiative corrections to the muonium hyperfine structure. II. the $\alpha(z\alpha)^2$ correction, Phys. Rev. D **55** (1997) 7267–7290.
URL https://link.aps.org/doi/10.1103/PhysRevD.55.7267

[18] S. G. Karshenboim, Leading logarithmic corrections and uncertainty of muonium hyperfine splitting calculations, Zeitschrift für Physik D Atoms, Molecules and Clusters **36** (1996) 11–15.
URL https://doi.org/10.1007/BF01437414

[19] T. Kinoshita, NRQED Approach to the Hyperfine Structure of the Muonium Ground State (1998).

[20] A. Karimkhodzhaev, R. N. Faustov, Contribution of hadronic vacuum polarization to hyperfine splitting in muonium, Sov. J. Nucl. Phys. **53** (1991) 626–627, yad. Fiz.

[21] D. Nomura, T. Teubner, Hadronic contributions to the anomalous magnetic moment of the electron and the hyperfine splitting of muonium, Nuclear Physics B **867** (2013) 236 – 243.
URL http://www.sciencedirect.com/science/article/pii/S0550321312005482

[22] A. Czarnecki, S. I. Eidelman, S. G. Karshenboim, Muonium hyperfine structure and hadronic effects, Phys. Rev. D **65** (2002) 053004.
URL https://link.aps.org/doi/10.1103/PhysRevD.65.053004

[23] S. I. Eidelman, S. G. Karshenboim, V. A. Shelyuto, Hadronic effects in leptonic systems: muonium hyperfine structure and anomalous magnetic moment of muon, Canadian Journal of Physics **80** (2002) 1297–1303.
URL https://doi.org/10.1139/p02-103

[24] S. G. Karshenboim, V. A. Shelyuto, A. I. Vainshtein, Hadronic light-by-light scattering in muonium hyperfine splitting, Phys. Rev. D **78** (2008) 065036.
URL https://link.aps.org/doi/10.1103/PhysRevD.78.065036

[25] M. I. Eides, H. Grotch, V. A. Shelyuto, Theory of light hydrogenlike atoms, Physics Reports **342** (2001) 63 – 261.
URL http://www.sciencedirect.com/science/article/pii/S0370157300000776

[26] M. I. Eides, Weak-interaction contributions to hyperfine splitting and Lamb shift, Phys. Rev. A **53** (1996) 2953–2957.
URL https://link.aps.org/doi/10.1103/PhysRevA.53.2953

[27] G. W. Bennett *et al.*, Final report of the E821 muon anomalous magnetic moment measurement at BNL, Phys. Rev. D **73** (2006) 072003.
URL http://link.aps.org/doi/10.1103/PhysRevD.73.072003

[28] M. Davier *et al.*, Reevaluation of the hadronic vacuum polarisation contributions to the standard model predictions of the muon using newest hadronic cross-section data, The European Physical Journal C **77** (2017) 827.
URL https://doi.org/10.1140/epjc/s10052-017-5161-6

[29] C. Patrignani *et al.*, Review of Particle Physics, Chin. Phys. C **40** (2016) and 2017 update 100001.

[30] A. Czarnecki, W. J. Marciano, Muon anomalous magnetic moment: A harbinger for "new physics", Phys. Rev. D **64** (2001) 013014.
URL https://link.aps.org/doi/10.1103/PhysRevD.64.013014

[31] B. L. Roberts *et al.*, Muon $g-2$ technical design report (2015).

[32] T. Mibe *et al.*, Technical design report for the measurement of the muon anomalous magnetic moment $g-2$ and electric dipole moment at J-PARC (to be published).

[33] T. Crane *et al.*, Observation of a Quadratic Term in the hfs Pressure Shift for Muonium and a New Precise Value for Muonium $\Delta\nu$, Phys. Rev. Lett. **27** (1971)

474–476.
URL https://link.aps.org/doi/10.1103/PhysRevLett.27.474

[34] V. Tishchenko *et al.*, Detailed report of the MuLan measurement of the positive muon lifetime and determination of the Fermi constant, Phys. Rev. D **87** (2013) 052003.
URL https://link.aps.org/doi/10.1103/PhysRevD.87.052003

[35] W. Higemoto *et al.*, Materials and Life Science Experimental Facility at the Japan Proton Accelerator Research Complex IV: The Muon Facility, Quantum Beam Science **1**.
URL http://www.mdpi.com/2412-382X/1/1/11

[36] E. B. Saloman, Energy levels and observed spectral lines of krypton, Kr I through Kr XXXVI, Journal of Physical and Chemical Reference Data **36** (2007) 215–386.
URL https://doi.org/10.1063/1.2227036

[37] D. G. Fleming, R. J. Mikula, D. M. Garner, $\mu^+$ charge exchange and muonium formation in low-pressure gases, Phys. Rev. A **26** (1982) 2527–2544.
URL https://link.aps.org/doi/10.1103/PhysRevA.26.2527

[38] A. Kramida *et al.*, NIST Atomic Spectra Database (ver. 5.5.6), [Online]. Available: https://physics.nist.gov/asd [2018, May 2]. National Institute of Standards and Technology, Gaithersburg, MD. (2018).

[39] R. M. Mobley *et al.*, Muonium chemistry, The Journal of Chemical Physics **44** (1966) 4354–4355.
URL https://doi.org/10.1063/1.1726633

[40] R. M. Mobley *et al.*, Muonium chemistry II, The Journal of Chemical Physics **47** (1967) 3074–3075.
URL https://doi.org/10.1063/1.1712335

[41] P. A. Thompson *et al.*, Muonium. IV. Precision Measurement of the Muonium Hyperfine-Structure Interval at Weak and Very Weak Magnetic Fields, Phys.

Rev. A **8** (1973) 86–112.
URL https://link.aps.org/doi/10.1103/PhysRevA.8.86

[42] H. Yoshida, Oho seminar.
URL http://accwww2.kek.jp/oho/OHO%20text%20archives%202005-2011/OHO08%20web%20final/02%20yoshida_08all.pdf

[43] D. M. Pozar, Microwave Engineering, 4th Edition, Wiley, 2011.
URL https://books.google.co.jp/books?id=JegbAAAAQBAJ

[44] K. Ueno and M. Tanaka and T. Uchida and M. Ikeno, iEEE Nucl. Sci. Symp. Conf. Rec. 2013.

[45] F. James, M. Roos, Minuit - a system for function minimization and analysis of the parameter errors and correlations, Computer Physics Communications **10** (1975) 343 – 367.
URL http://www.sciencedirect.com/science/article/pii/0010465575900399

[46] S. Kanda, Ph.D. Thesis (2017).

[47] K. S. Tanaka, Ph.D. Thesis (2015).

# Acknowledgements

It was a great experience to work on MuSEUM and the detector development for the $g-2$/EDM experiment at J-PARC. I am indebted to MuSEUM collaborators, Prof. Koichiro Shimomura, Prof. Yasuyuki Matsuda, Prof. Hiroyuki A. Torii, Prof. Patrick Strasser, Prof. Akihisa Toyoda, Prof. Yoshinori Fukao, Prof. David Kawall, Prof. Kazuo S. Tanaka, Dr. Sohtaro Kanda, Mr. Yasuhiro Ueno, Mr. Toya Tanaka, Mr. Shun Seo, and Mr. Daisuke Yagi. They gave me useful and constructive comments and suggestions.

I would like to express my gratitude to Prof. Savely G. Karshenboim and Dr. Daisuke Nomura for many constructive theoretical discussions.

I am deeply grateful to my advisors, Prof. Naohito Saito and Prof. Tsutomu Mibe for their guidance. Their insightful comments were a great help.

I would like to thank the silicon detector group at KEK, Dr. Yutaro Sato, Prof. Tatsuya Kume, Prof. Osamu Sasaki, Mr. Takashi Kohriki, Prof. Kazuki Ueno, for their useful technical advice about the silicon detector and its mechanical structure.

Advice and support given by the Electronic System Group, Prof. Manobu Tanaka, Prof. Tomohisa Uchida, Mr. Masayoshi Shoji, Mr. Masahiro Ikeno, Mr. Hiroshi Sendai, were a great help to operate the electrical circuits of the silicon detector.

I am indebted to the silicon detector group at Kyushu University, Prof. Junji Tojo, Prof. Tamaki Yoshioka, Prof. Kiyotomo Kawagoe, Prof. Taikan Suehara, Dr. Takashi Yamanaka, Mr. Shohei Shirabe, Mr. Shinji Koura, Mr. Tsubasa Nagasawa, Mr. Masato Matama, Mr. Takumi Ito, and Mr. Yuki Tsutsumi. Their support and comments during the detector construction were invaluable.

I would like to thank J-PARC MLF MUSE personnel, Prof. Yasuhiro Miyake, Prof. Kenji M. Kojima, Prof. Naritoshi Kawamura, Dr. Noriyuki Kurosawa, Dr.

Yutaka Ikedo, Dr. Taihei Adachi, and Mr. Koji Hamada, for engineering and technical support.

I would like to thank my colleagues in Saito's laboratory, Dr. Masashi Otani, Mr. Ryo Kitamura, Mr. Kohei Hanzawa, Mr. Hiromasa Yasuda, and Mr. Li Sirui for making a working environment comfortable and enjoyable.

Finally, I would like to thank Ms. Hisako Ohata, Ms. Tomoko Iida, and Ms. Saori Shigematsu for office work support.